PLANKTONIC PROPULSION:
THE HYDRODYNAMICS, KINEMATICS, AND DESIGN OF METACHRONY

A Thesis
Presented To
The Academic Faculty

By

David W. Murphy

In Partial Fulfillment
Of the Requirements for the Degree
Doctor of Philosophy in Civil and Environmental Engineering

Georgia Institute of Technology

August, 2012

PLANKTONIC PROPULSION:
THE HYDRODYNAMICS, KINEMATICS, AND DESIGN OF METACHRONY

Approved by:

Dr. Donald R. Webster, Co-Advisor
School of Civil and Environmental Engineering
Georgia Institute of Technology

Dr. Jeannette Yen, Co-Advisor
School of Biology
Georgia Institute of Technology

Dr. Silas Alben
School of Mathematics
Georgia Institute of Technology

Dr. Meghan Duffy
School of Biology
Georgia Institute of Technology

Dr. David Hu
School of Mechanical Engineering
Georgia Institute of Technology

Dr. Philip J. W. Roberts
School of Civil and Environmental Engineering
Georgia Institute of Technology

Date Approved: June 28, 2012

Dedicated to the Memory of my Grandfather

Ralph Waldo Murphy (1920 – 2010)

Farm Boy, WW II Pilot, NASA Engineer, Magician

And the Most Curious Man I've ever met

ACKNOWLEDGEMENTS

I'm so grateful to the scores of people the world over who have helped me in big and small ways over the past several years, to those who have provided guidance, funding, an occasional kick in the pants, and friendship. In particular, I'd like to thank my advisors, Dr. Donald Webster and Dr. Jeannette Yen, for being an excellent team and for letting me participate in their amazing collaboration. I'd also like to thank Jeannette for taking me on as a grad student (rescuing me, really!) and patiently bearing with me during that transition. Because of you, I'm doing exactly what I hoped I'd be doing ten years ago. Thanks for your guidance and creativity along the way and for gathering animals from all over the globe for us to play with. I'd also like to thank Don for offering excellent advice, for being the most organized man on earth, and for being the best editor I'll ever have.

I'm grateful to my committee, Dr. Silas Alben, Dr. Meghan Duffy, Dr. David Hu, and Dr. Phil Roberts, for taking the time to engage with my work. I'm particularly thankful to Dr. Roberts for agreeing to be a last-minute addition to my committee and to Dr. Duffy for providing *Daphnia*.

Many thanks to my labmates past and present, both in the Webster and Yen labs, for friendship, commiseration, and tea breaks. Thanks to Aaron True, Ann Larson, Joseph Chrzan, Sarah Delavan, Rachel Lasley-Rasher, Larisa Pender-Healy, and Kathy Nagel. Thanks especially to Rachel for help with statistics. Thanks, too, to Daniel Borrero for good advice.

I'm thankful to have been assisted by many amazing undergraduate students over the past several years. I'm grateful to them, especially to Marleen Kanagawa, Nadir Kabir,

Morgan Stephenson, Lin Fan, Eleanor Middlemas, and Thanh Nguyen. Thanks for digitizing loads of data and for bearing with me as I learn how to manage.

Many people have helped by either sending us animals or by hosting us as we travel to find them. I remember with fondness my time Down Under at the Australian Antarctic Division thanks to the hospitality of Rob King, So Kawaguchi, and Steve Nicol. Thanks to Kate Ruck and Debbie Steinberg for sending Antarctic krill to Atlanta! Thanks also to those sending us copepods, pteropod, and ostracods from all over the world.

Thanks to Andy and Mike in the shop and Mike in IT and to the guys at LaVision (Callum Gray, Doug Neal, Steve Anderson, and Dirk Michaelis) for working with us to make the Tomo PIV system a success.

Thanks as well to my friends, especially the guys at the A1 House, for fellowship and encouragement. Thanks to Marc, Terry, Inouye, Matthias, Brian, and Dan. Thanks especially to Marc Sedjro for being a true friend for all these years. We made it, Dr. Sedjro! Thanks to Liz, Steph, Josie, Nit, Devi, Thomas, Conner, Mary Ellen, Tim, Brent, Amanda, and Yingjie too for good dinners and friendship. And thanks to Steph and Devi for krill cupcakes! And thanks to Joi for encouragement and two decades of friendship!

Thanks to my family, Mom, Dad, Michael, Katie and the kids for their encouragement and reminders of life outside the lab.

And thanks to Jesus, who created such an awesome world that I get to explore and who is ever so slowly but surely setting what's wrong with the world right again.

TABLE OF CONTENTS

LIST OF TABLES

LIST OF FIGURES

Page

NOMENCLATURE

BA	Body angle
BL	Body length
FFW	Fast forward swimming
HOV	Hovering
USD	Upside down swimming
Re	Reynolds Number
St	Strouhal number
St_{ws}	Strouhal number calculated from wake speed
St_{ss}	Strouhal number calculated from swimming speed
A	Total pleopod area
B	Length between adjacent appendages
D	Divergence
I	Hydrodynamic impulse
J	Advance ratio
J_m	Normalized advance ratio
L	Appendage length

M	Impulsive stresslet strength
T	Thrust
U^*	Velocity threshold
V	Swimming speed
W_U	Underwater weight
e_{ij}	Strain rate tensor
f	Beat frequency
m	Number of appendage pairs
n	Beat frequency
p	Pressure
t	Time
t^*	Time to reach threshold
v_{ind}	Induced velocity
v_w	Jet wake velocity
α	Pleopod angle between body and protopodite
β	Pleopod angle between protopodite and endopodite
γ	Pleopod angle between endopodite and exopodite

Γ	Circulation
θ	Stroke amplitude
ψ	Viscous energy dissipation rate
ρ	Fluid density
x	Axial distance
r	Radial distance
φ	Azimuthal angle
υ	Kinematic viscosity
μ	Dynamic viscosity
ω	Vorticity

SUMMARY

Locomotion is a key characteristic of almost all forms of life and is often accomplished, whether on land, in water, or in the air, by reciprocal motion of two or more appendages. Among the zooplankton, many species propel themselves by rhythmically beating multiple pairs of closely spaced leg-like appendages in a back-to-front (metachronal) pattern. The focus of this study is to understand the mechanical design, kinematic operation, and hydrodynamic result of metachrony in the zooplankton.

In the first part of this study, Antarctic krill (*Euphausia superba*) are investigated as an ecologically important model species that metachronally beats its swimming legs (pleopods) to perform drag-based propulsion. Based on high speed videos of freely swimming Antarctic krill, hovering, fast forward swimming, and upside down swimming are identified as three distinct swimming modes with significantly different stroke amplitudes and beat frequencies. When transitioning between hovering and fast forward swimming, Antarctic krill first increase beat amplitude and secondarily increase beat frequency. In considering the design components that contribute to metachrony being a successful swimming technique, a comparison among many different species shows that the ratio between the appendage separation distance and appendage length is limited to a narrow range of values (i.e. 0.2 – 0.65).

In the second part of this study, metachrony is examined at smaller length and time scales by examining the impulsive escape jump of a calanoid copepod (*Calanus finmarchicus*). The wake generated by the copepod's metachronally beating swimming legs is experimentally measured using a novel (and newly developed) tomographic particle

image velocimetry (PIV) system capable of making volumetric 3D velocity measurements with high temporal and spatial resolution using IR illumination. The flow generated by the escaping copepod consisted of a stronger posterior vortex ring generated by the metachronally stroking swimming legs and a weaker one generated anteriorly around the body by the impulsive start of the escape, both of which decayed over time. The experiments also revealed azimuthal asymmetry in the vortices caused by body yawing and the action of the swimming legs, flow features not considered in previous axisymmetric computational and theoretical models of copepod jumps. While not accounting for this asymmetry, an impulsive stresslet is nonetheless useful in modeling the flow created by the escaping copepod and represents the flow more accurately than an impulsive Stokeslet.

In the final part of this study, the flow associated with metachronal hovering in Antarctic krill is experimentally and theoretically investigated in regards to the energy requirements of the pelagic lifestyle. Volumetric flow measurements of a hovering Antarctic krill show that each stroking pleopod drags flow behind it such that a downward stream develops medially. The lateral exopodites induce tip vortices which add to the lift force on each appendage. Furthermore, the flow beneath the hovering krill develops into a pulsed jet with a Strouhal number in the 'high-efficiency zone' of $0.2 < St < 0.4$. Actuator disk theory is used to make theoretical estimates of the induced power necessary to hover, the results of which match induced power values calculated from measured flow gradients contributing to viscous energy dissipation.

CHAPTER 1

INTRODUCTION

Locomotion is a key characteristic of almost all forms of life and is often accomplished, whether on land, in water, or in the air, by reciprocal motion of two or more appendages. In the watery world of the zooplankton, a surprisingly large number of species propel themselves by rhythmically beating multiple pairs of closely spaced oar-like appendages in a back-to-front (metachronal) pattern. Most of these species are rather small crustaceans and range in size from approximately 100 microns (e.g. copepods) up to tens of centimeters (e.g. lobsters). Though these animals are small, they are incredibly numerous and are key species in aquatic ecosystems. The global biomass of just one species using metachronal propulsion, the Antarctic krill (*Euphausia superba*), for instance, has been estimated at 379 million metric tons (Atkinson et al. 2009) which is comparable to the global human biomass of approximately 420 million metric tons, assuming 7 billion humans at an average mass of 60 kg.

The metachronal propulsion system has been adapted by various animals and thus shows a large amount of variation. Beat frequencies, for example, may span two orders of magnitude (from 1 to 100 Hz). Some animals, such as calanoid copepods reserve metachronal swimming for when they need to escape (at speeds up to 1 m s^{-1}). Others, such as krill, use a metachronal gait for normal swimming (and escape with a different technique). In another example, lobsters use metachronal beating to produce jet-assisted walking (Lim and Demont 2009). Understanding the design and operation of this type of

propulsion system in all its variations can bring new insight into the behavior and energetic of these ecologically-important animals.

The goal of this study is to understand the mechanical design, kinematic operation, and hydrodynamic result of the metachronal propulsion system that is so widespread in the zooplankton. In order to examine design variation across different species, aspects of metachronal propulsion will be investigated in both Antarctic krill and in calanoid copepods.

Specific Aim 1: Examine the design and kinematic operation of metachrony in a model species exhibiting a variety of swimming behaviors.

The Antarctic krill, *Euphausia superba,*was chosen to study the design of metachrony and various metachronal swimming gaits because it is a highly motile pelagic species with great ecological importance in the Antarctic. Free-swimming Antarctic krill were filmed in the laboratory with a high speed camera, and the kinematics of their swimming appendages were digitized and analyzed. Based on differences in body orientation, stroke amplitude, and stroke frequency, the recorded events are classified into distinct swimming gaits. Finally, the interlocking morphological, hydrodynamic, and kinematic components that make metachrony successful as a locomotion strategy are considered from a design perspective.

Specific Aim 2: Develop a volumetric flow measurement system in order to better characterize the hydrodynamics of metachrony.

A high-speed tomographic particle image velocimetry (PIV) system is developed and applied to another species using metachrony: a calanoid copepod performing an impulsive escape jump. In contrast to the Antarctic krill investigated in Specific Aim 1, this investigation provides another perspective on metachronal locomotion by examining a much smaller species operating on a much shorter time scale. The flow generated by the copepod is extensively analyzed and is compared to mathematical models and to previously published computational fluid dynamics (CFD) results. The effect of the metachronally striking swimming legs on the surrounding flow is especially considered.

Specific Aim 3: Investigate the hydrodynamics and energetic of metachronally produced hovering in Antarctic krill.

High-speed volumetric flow measurements around hovering Antarctic krill are acquired and used to investigate both the local flow generated by single pleopods and wake flows created by the appendages. The energetics of the jet-like flow produced by krill hovering is considered through theoretical considerations of the induced power and through experimental measurements of viscous energy dissipation.

Results of this study will lead to a better comprehension of a widespread locomotion technique. Kinematic and flow measurements associated with metachrony lead to better

estimates of swimming energetics and hydrodynamic signal production. Hydrodynamic signal production and perception are key in understanding predator-prey interactions in the zooplankton. A zooplanktonic species that employs only one pair of appendages for locomotion, the cladoceran *Daphnia magna*, also will be briefly investigated for comparison.

This thesis is organized as follows: Background information concerning the physiology and behavior of common zooplankton species will be presented in Chapter 2. In Chapter 3, an investigation of the kinematics and design of metachrony in the Antarctic krill based on high speed video will be described. In Chapter 4, a newly designed and built tomographic particle image velocimetry (PIV) system is described and is applied to volumetrically measure the flow field of the escape jump of a calanoid copepod (*Calanus finmarchicus*). The hydrodynamic signal extent and energy dissipated as a result of the escape jump also are investigated in order to show the capabilities of the new experimental system. Chapter 5 describes the application of the tomographic PIV system to metachronally produced hovering in Antarctic krill. Chapter 6 will draw out some of the limitations of the current study, draw conclusions based on this work, and present directions for future work. Finally Appendix A will present volumetric flow measurements of a swimming daphniid for comparison with the metachronal swimming of the copepod presented in Chapter 4.

CHAPTER 2

BACKGROUND

This chapter provides a general introduction to zooplankton biology, with emphasis on copepods, daphniids, and krill. The hydrodynamics and kinematics of specific behaviors such as swimming, escaping, feeding, and sensing then will be examined in more detail.

2.1. A Zooplankton Primer

Zooplankton are a diverse assemblage of mostly small organisms defined not by taxonomy but by their free-swimming way of life in the open waters of lakes and oceans. Every major phylum, in fact, includes organisms that are planktonic in at least part of their life cycle (Miller, 2004). Figure 1.1 shows some examples of zooplankton diversity. Although there is a wide variety of planktonic species, they are not equally numerous. Small crustaceans such as copepods and cladocerans are the major component of the zooplankton in most planktonic food webs (Bronmark and Hansson, 2005). Copepods, which are found in both marine and freshwater environments, are argued to be the world's most numerous metazoans (Humes, 1994) and, in marine systems, dominate the mesozooplankton both numerically and in biomass (Miller, 2004). In many lakes and ponds, on the other hand, cladocerans, specifically those of the genus *Daphnia*, are the major herbivore (Bronmark and Hansson, 2005). In ecological terms, both cladocerans and copepods are important food source for larger animals such as fish. These crustaceans, in turn, are important grazers on phytoplankton (Bronmark and Hansson, 2005). This work will focus on copepods, daphniid cladocerans, and Antarctic krill, and all three types will be briefly introduced here.

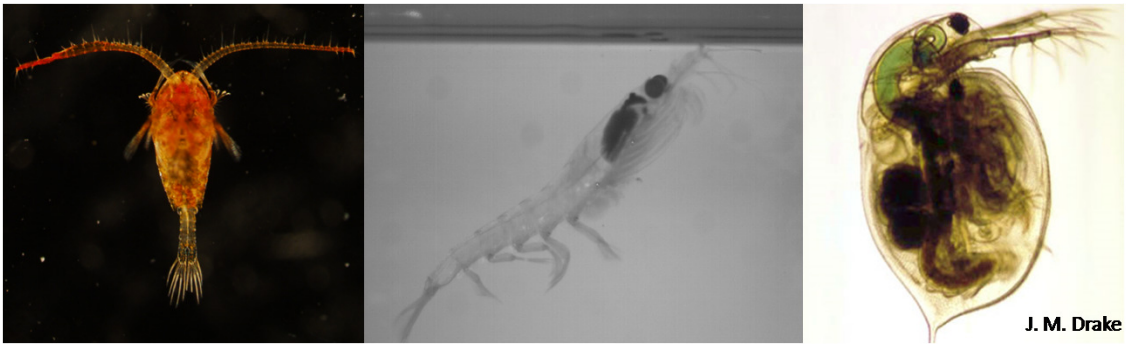

Figure 2.1 Images (from left to right) of a copepod, Antarctic krill, and *Daphnia* (water flea).

2.1.1. Copepods

Planktonic copepods are small, generally in the range of 0.5 to 3 mm in length. The copepod body is divided into two main sections, the pellet-shaped prosome and the much narrower urosome. The prosome, the length of which is used as a direct measure of animal size, contains the antennules, which are used for sensing, the second antennae which are rapidly vibrated for feeding and swimming, the mouthparts, and the swimming appendages. The rudder-like urosome is often flexed in swimming. The appendages, which are paired and morphologically complex, are used in swimming, mating, and finding and eating food (Mauchline, 1998).

The free-swimming copepods are divided into three major groups, the calanoids, cyclopoids, and harpacticoids. The calanoids are characterized by long antennules, an elongated body, and one egg sac, though some also may broadcast their eggs directly into the water. Most of the calanoids are equipped with filtering mouthparts and are

herbivores, feeding on phytoplankton and protists filtered from the water. The cyclopoids have a much more rounded body, shorter antennules, and two egg sacs. Cyclopoid copepods consume both algae and other zooplankton and are raptorial in that they pick out individual food particles. Cyclopoids swim by a characteristic 'hop and sink' swimming mode, and the hopping is used to attack prey (Bronmark and Hansson, 2005). Harpacticoid copepods have a cylindrical body shape (without an apparent articulation between the prosome and urosome), extremely short antennules, and two egg sacs. The urosome of harpacticoids also is characterized by long setae on the caudal rami (Todd et al., 1996). Harpacticoids are primarily benthic or littoral and have mouthparts adapted for scraping particles from surfaces (Bronmark and Hansson, 2005).

2.1.2. Daphniids

Daphniids are generally transparent and 0.2 to 3 mm in length (Pennak, 1978). These organisms are commonly called 'water fleas' because of their shape and the jerky motion with which they swim (Bronmark and Hansson, 2005). A daphniid body is shaped like a laterally compressed disc. The carapace has a bivalve appearance with a ventral opening which is usually lined with setae (Pennak, 1978). The posterior end of the carapace often bears a spine. A daphniid's head is bent downward and contains a large compound eye. The head also may bear an elongated helmet. The first antennae (antennules), which are quite small and used in olfaction, are located ventrally on the head. The large second antennae are laterally attached just below the head and serve as swimming paddles. They

are biramous with a variable number of setae. These antennae beat to produce a sequence of hops that more or less keep the animal in continuous motion (Pennak, 1978).

One unique aspect of some daphniid species is their ability to undergo cyclomorphosis, a seasonal change in morphology. During the fall, winter and early spring, a population of cyclomorphic daphniids has a normal, round-headed appearance. In the late spring, however, the head begins to elongate into a 'helmet.' The helmet persists until early fall and then reverts to the normal appearance. The posterior spine and the eye may change size, and protective neck teeth also may develop (Pennack, 1978; LaForsch and Tollrian, 2004a). The phenomenon varies widely among populations and seems to occur less in ponds and shallow lakes than in larger and deeper lakes. Even within a population exhibiting cyclomorphosis, the degree of this cyclomorphic development varies greatly. Cyclomorphosis appears to have multiples causes. Increased temperature during early stages of development has been shown to increase the helmet formation, as has the level of small-scale turbulence in the water (Pennack, 1978; LaForsch and Tollrian, 2004b). Chemical cues from invertebrate predators such as the cladoceran *Leptodora kindtii* and the phantom midge larvae *Chaoborus* as well as vertebrate predators such as fish also have been shown to induce helmet formation, and these induced defenses have been shown to effectively reduce predation (LaForsch and Tollrian, 2004a; Gelinas et al., 2007). Increased swimming ability and gas exchange ability have also been proposed as functions for the cyclomorphic form (Hebert, 1978).

2.1.3. Antarctic krill

Antarctic krill (*Euphausia superba*) are the most ecologically-important of the euphausiid crustaceans and live in the Southern Ocean surrounding Antarctica. They can grow quite large, up to 65 mm in length, and can live up to six or seven years and are thus perhaps better considered part of the nekton, which have strong swimming abilities (Knox, 1994). Despite their large size, Antarctic krill, like many other zooplanktonic species, feed on phytoplankton. They do this by grabbing parcels of water with their filtering basket and squeezing the water out until an algae bolus remains (Hamner et al., 1983). Because they serve as a vital link in the (very short) food web between the phytoplankton and larger animals (seabirds, whales, fish, penguins, seals), they are considered a keystone species in the Antarctic. Antarctic krill are also subject to a fishery for human use. Antarctic krill usually swim (up to eight body lengths per second) by metachronally beating five pairs of swimming appendages known as pleopods, although they also perform a tail flip escape reaction (up to eleven body lengths per second) (Kils, 1981).

Antarctic krill are unique in that they are considered obligate schoolers (Hamner et al., 1983). They exhibit exceptional aggregative behavior and are known to form schools that may extend for several kilometers in the horizontal direction and for greater than 100m in the vertical direction (Hamner et al. 1983). These schools are generally characterized by synchrony and polarized swimming. Proposed benefits for school membership include increased hydrodynamic efficiency (drafting) and improved awareness of external environmental signals, such as those created by prey, predators, or mates. Hamner et al. (1983) proposed that contact within these schools was maintained by rheotaxis, that is, the hydrodynamic signals generated by the beating pleopods.

2.2. Hydrodynamics of Plankton

At the length and time scales at which most zooplankton behavior occurs, viscosity plays an important role in flow dynamics.Viscosity affects every aspect of zooplankton biology, including swimming, filtering food particles, and sensing the approach of a predator. The Reynolds number *Re*, the ratio between inertial and viscous forces, defines the relative importance of these competing forces and is defined as $Re = \rho Vd/\mu$, where ρ is the fluid density, V is a characteristic velocity, d is a characteristic length, and μ is the dynamic viscosity of the fluid. A typical Reynolds number for a calanoid copepod (body length of 0.5 – 5 mm) swimming at 1 to 20 $mms^{-1}$is in the range of 0.5 to 150 (Mauchline, 1998). The effects of this low Reynolds number environment will be elucidated by examining the kinematics and hydrodynamics of swimming, sensing, and feeding in copepods and daphniids.

2.2.1. Copepods

2.2.1.1. *Swimming*

Swimming behavior in pelagic copepods can generally be divided into two distinct forms, cruise swimming and jumping (Jiang et al., 2002a). In cruise swimming, the animal propels itself forward by the rapid beating of it cephalic (feeding) appendages, often at a high frequency. Cruise swimming is closely associated with the beating of the same appendages to produce a feeding current, a behavior that will be discussed later. In a study of *Temora longicornis*, van Duren and Videler (2003) used a high-speed camera to film the feeding appendages and found that the mouthparts beat at a frequency of

approximately 40 Hz and propelled the animal forward at an average speed of 3.4 mm s^{-1}. Similarly, Catton et al. (2007) found that *Euchaeta antarctica* copepodids beat their appendages at approximately 50 Hz in order to swim at aspeed of 8.2 mm s^{-1}.The Reynolds number associated with cruising has been estimated at less than 10 (Yen, 2000) and between 2 and 6 (van Duren and Videler, 2003). Swimming direction and body orientation during cruise swimming can vary greatly between species. Both horizontal and vertical body orientations are observed, and animals may swim forwards, backwards, or even in loops (Jiang et al., 2002a; Mazzocchi and Paffenhöfer, 1999).

The flow associated with cruise swimming has been studied experimentally (Strickler, 1975; Bundy and Paffenhöfer, 1996; Yen and Strickler, 1996; van Duren and Videler, 2003; Catton et al., 2007) and through computer simulations (Jiang, 2002a,b). Both tethered and free-swimming animals have been studied, but Catton et al. (2007) showed that tethering dramatically modifies the flow produced by the animal. In the dorso-ventral view and in the side view of a free-swimming copepod in Catton et al. (2007), the flow converges slightly in front of the animal and subsequently diverges again behind the animal. A maximum flow velocity of 12 mm s^{-1} in the dorso-ventral view was found to the side of the animal's abdomen. In the side view, the maximum velocity (14 mm s^{-1}) was found beneath the animal, in the region behind the beating cephalic appendages. Simulations by Jiang et al. (2002b) agree with these experimental results and also show a funnel-like flow field that converges at the animal's cephalic appendages.

The second form of copepod locomotion is jumping, in which a copepod whips back its antennules and beats its larger swimming legs (instead of the cephalic appendages) to produce a sudden jump forward (Yen, 2000). Jumps may serve to relocate the animal, to

attack prey, or to escape from a predator (Jiang and Kiørboe, 2011). A distinction is generally made between escape jumps, which are characterized by multiple strokes of the swimming legs to achieve velocities up to 1 m s^{-1}, and the other types of jumps ('hops'), which are less powerful (Yen, 2000). In an *Acartia tonsa* hop, the leg pairs stroked sequentially backwards, pushing the animal to a peak velocity of 100 – 200 mm s^{-1} in 10 – 25 ms, followed by a rapid deceleration to rest. The Reynolds number in this repositioning jump ranged from 20 to 100 (Kiørboe et al., 2010a). In an escape jump, a copepod may beat its swimming legs multiple timesin a metachronal manner at a frequency ranging from 44 to 117 Hz, as shown for a *Temora longicornis* escaping at 108 mm s^{-1} (van Duren and Videler, 2003). The copepod *Calanus finmarchicus,* on the other hand, was found to escape at peak speeds of 800 mms^{-1} and to travel up to 7 mm during one power stroke (Lenz et al., 2004). *Oithona davisae* and *Acartia tonsa* were shown to have mean beat frequencies during escapes of 137 Hz and 134 Hz, respectively (Kiørboe et al., 2010b). The speeds reached during escape jumps mean that copepods move from a regime dominated by viscosity to one dominated by inertia (Yen, 2000; van Duren and Videler, 2003). Reynolds numbers of copepods performing escape jumps may range up to 1000 (Yen, 2000).

The flow resulting from a copepod jump has been investigated via Schlieren optics (Strickler, 1977; Yen and Strickler, 1996) and particle image velocimetry (van Duren and Videler, 2003). Yen and Strickler (1996) showed that a toroidal vortex was shed from each impulsive jump during an escape. Using high-speed 2D particle image velocimetry on a tethered *Temora longicornis*, van Duren and Videler (2003) also found a jet mushrooming into a toroidal vortex from the escape reaction of the kicking swimming

legs. Kiørboe et al. (2010a) measured the flow field resulting from a copepod hop and found a wake vortex behind the animal and a second vortex that formed around the body of the decelerating copepod. The flow of the wake vortex was first modeled as an impulsive Stokeslet, although the model was later revised to an impulsive stresslet (two counter-rotating viscous vortex rings of similar intensity) to include the effect of the vortex in front of the decelerating animal (Jiang and Kiørboe, 2010). Borazjani et al. (2010) have also used CFD to investigate the flow of copepod hopping (in a tethered copepod model) and found that the antennules play a significant role in generating force. While the flow of copepod hopping has been experimentally observed, the flow field of a copepod escape has proven almost impossible to capture. Due to the extreme difficulty in capturing this rapid motion with a quantitative flow imaging system, Jiang and Kiørboe (2011) resorted to modeling the flow associated with a copepod escape jump via computational fluid dynamics. They found two dominant flow structures, a wake vortex as described by Yen and Strickler (1996) and a vortex of opposite sign surrounding the copepod body (in good agreement with the PIV flow data). Between these two similarly-sized vortex structures was an elongated train of vorticity blobs associated with individual kicks of the copepod swimming legs (Jiang and Kiørboe, 2011).

2.2.1.2. *Feeding*

In a recent review of zooplankton feeding, Kiørboe (2010) identifies the following four feeding mechanisms: passive ambush, active ambush, feeding-current, and cruise feeding. Passive ambush, in which a moving prey contacts a passive, non-motile grazer,

is not seen in copepods and will not be considered here. Active ambush is common among small, cyclopoid copepods,while the feeding current and cruising techniques are more common among larger calanoid species (Kiørboe et al., 2010a). Some species, such as *Acartia tonsa*, can even switch between feeding mechanisms based on the availability of certain prey or the suitability of the environment (Kiørboe et al., 1996).Different feeding strategies involve different hydrodynamics, and these will be discussed below.

In active ambush, the stationary copepod detects its prey remotely, usually from a hydrodynamic signal generated by the prey, and initiates an attack jump. This raptorial technique is often seen among small, pelagic copepods such as in the genus *Oithona* (a cyclopoid copepod). In a study of *Acartia tonsa* feeding on planktonic ciliates, Jonsson and Tiselius (1990) found that, as the animal passively sank at a mean speed of 0.58 mm s^{-1}, detection of prey initiated a rapid reorientation of the body and an attack on the prey. Ciliates were detected by the first antennae at a distance ranging from 0.1 to 0.7 mm, and the prey size was correlated with detection distance such that larger ciliates were detected while further from the antennae (Jonsson and Tiselius, 1990). In a similar study of much smaller *Oithona similis*, the copepods were found to sink at a rate of 0.09 mm s^{-1} and to detect and attack dinoflagellate prey at a mean distance of 0.14 mm (Svensen and Kiørboe, 2000). Following the copepod's rapid repositioning jump (in less than 0.1 second), the mouthparts move to capture and ingest the prey, a process that may last over 1 second (Jonsson and Tiselius, 1990). Kiørboe et al. (2009) similarly found that *Acartia tonsa* and *Oithona davisae* rapidly attacked prey (at speeds of approximately 100 mm s^{-1} within a few milliseconds) that came within approximately 0.2 mm of the predators' antennae. These authors further argued, based on a CFD model, that this rapidity was key

in order to prevent the formation of a viscous boundary layer on the predatory copepod that would push away the prey (Kiørboe et al., 2009). Finally, copepods using an active ambush technique will perform several repositioning jumps per minute to maintain their position in the water column, the hydrodynamics of which were examined by Kiørboe et al. (2010a).

In cruise feeding, a copepod actively swims (using its cephalic appendages) at a relatively high speed in an attempt to encounter prey. Upon detection of the prey, most likely through a hydrodynamic disturbance perceived by the first antennules, the copepod lunges towards its prey (Kiørboe 2010). Tiselius and Jonsson (1990) identified this feeding technique, interrupted by sinking bouts, in *Centropages typicus* and *Centropages hamatus*. Similarly, Mazzocchi and Paffenhöfer (1999) found that the calanoid *Clausocalanus furcatus* swam at very high speeds of up to 17 mm s^{-1} and often performed somersaults in its search for prey. Doall et al. (2002) described the three-dimensional attack volume of the copepod *Euchaeta rimana* as it both hovered (at less than 3 mm s^{-1}) and cruised (at speeds up to 13 mm s^{-1}). The prey (smaller copepods) were detected and attacked within an ellipsoidal volume anterior to the long axis of the predator's first antennae, with clusters of attacks located near the longest and most sensitive setae. The predator attacked prey within this volume at a mean distance of 1.5 mm at a mean speed of 98.2 mms^{-1}. Propulsion towards the prey involved action of the swimming legs, flexion of the urosome, folding of the first antennae alongside the body, and occasional complex re-orientation of the body axis (Doall et al., 2002).

Feeding via generation of a feeding current, or suspension feeding, is seen in many calanoid copepods. A feeding current is generated by rapid vibration of the cephalic

appendages. Unless "tethered" by the force of gravity (Strickler, 1982), this activity tends to translate the animal as previously discussed for cruise swimming (Catton et al., 2007). As shown by Koehl and Strickler (1981), algae particles are not mechanically filtered onto a mesh but are individually perceived and directed towards the second maxillae where they are picked out of the current. For this reason, these feeding currents have been termed 'scanning currents' (Childress et al., 1987). Individual perception likely is achieved through chemical sensing of the phycosphere, the elongated chemical trail that surrounds an algal cell (Andrews, 1983). This trail reaches the copepod's chemoreceptors well before the actual food item, thereby alerting the copepod to actively trap the parcel of water containing the food item (Kiørboe, 2010).

Strickler (1982) visualized the feeding current flow field in *Eucalanus crassus* and found a double shear field, with flow converging both ventrally and laterally to produce a maximum flow near the beating cephalic appendages. Tiselius and Jonsson (1990) visualized the flow fields of several suspension feeding calanoid copepods and found that it was species-dependent and that it could generally be modeled as a point force acting in an infinite volume (a Stokeslet). Jonsson and Tiselius (1990) also investigated *Acartia tonsa*, which can switch between raptorial and suspension feeding, and found feeding current flow speeds of 8 mm s^{-1} near the second maxillae and 4 mm s^{-1} at a distance of 0.5 mm from the capture area. Fields and Yen (1993) characterized the three-dimensional structure of the copepod *Pleuromamma xiphias* and found speeds of up to 38 mms^{-1} in tethered animals. Yen and Strickler (1996) measured the flow field of tethered *Euchaeta rimana* and found a high-speed zone (16 – 20 mms^{-1}) around the beating antennae with steep velocity gradients both laterally and dorsally. It also was noted that the antennules

distally extended beyond the self-generated flow field in order to detect flow signals generated by predators (Yen and Strickler, 1996). Jiang et al. (2002b) performed CFD to model the flow field around a copepod swimming by feeding current generation and found a roughly conical streamtube extending from the 'capture area' of the copepod's feeding appendages. Essentially, this feeding current streamtube of laminar flow provides a three dimensional map of the animal's surroundings, with chemo- and mechanoreceptors receiving input from fairly well-defined locations (Yen, 2000). Finally, Malkiel et al. (2003) measured the three dimensional flow field of a feeding calanoid copepod via holographic PIV and found that, in the copepod's reference frame, the particles in the feeding current had a recirculating pattern that required the animal to hop occasionally in order to sample a new water volume.

2.2.1.3. *Sensing*

Although responsive to light, copepods primarily sense their world (i.e. food, prey, predators, mates) through chemoreception and mechanoreception, and both of these sensory systems are mediated by their fluid environment. As discussed in the previous section, chemical scents from an algal phycosphere are borne via the feeding current to aesthetascs located proximally on the antennules (Lenz et al., 1996; Yen, 2000). Female pheromones are also detected in this way by males, which have been shown to follow scent trails through the water (Doall et al., 1998). Males of some species (*Euchaeta*) have also been shown to lose mechanoreceptive ability and to obtain a second set of

aesthetascs in their final reproductive stage (Boxshall et al., 1997; Boxshall and Huys, 1998), presumably in order to better detect and pursue females.

Strickler and Bal (1973) proposed that setae located on the antennules functioned as mechanoreceptors which detects disturbances in the water from prey, predators, or mates. Landry (1980) also suggested the involvement of the first antennae in remotely sensing prey when he saw a decrease in predatory feeding (as opposed to suspension feeding) when the first antennae were amputated in *Calanus pacificus*. The distribution and structure of the setae on these antennae seem particularly well suited to detecting disturbances of different strengths and from different directions (Yen and Nicoll, 1990; Yen, 2000).The setae of different sizes and shapes, are oriented in multiple planes and seem to be concentrated proximally and distally (Yen et al., 1992; Lenz and Yen, 1993; Lenz et al., 1996). The proximal setae are useful in detecting prey in the feeding current while the distal setae (in the relatively quiet region outside the feeding current) serve to detect approaching predators. High-drag setae, which are long and feathered, bend at the slightest flow while filtering out high frequency background noise. In contrast, stiff hairs normally in the boundary layer could be useful for detecting high-speed flows (Yen, 2000; Fields et al., 2002). Electrophysiological studies have shown the extreme sensitivity of these setae (Yen et al., 1992; Gassie et al., 1993; Hartline et al., 1996). Yen et al. (1992) measured neural activity at the base of the large antennae in several copepod species in response to mechanical stimuli and found that displacements as low as 10 nm could cause a spike in neural activity. In addition, Fields et al. (2002) found directional bias in the bending of individual setae, with setae #8 exhibiting much greater neural activity when bending in the distal as opposed to the proximal direction. Fields and Yen

(2002) also showed that *Euchaeta rimana* responded differently (with antennal flicks, capture movements, or escapes) to hydrodynamic signals of increasing magnitude. The setal array on the copepod's antennules therefore provides a highly sophisticated detection system that allows the animal to localize, with great accuracy, opportunities due to prey or danger due to predators.

In parallel with an increased understanding of the morphology of the copepod antennal sensory system has come a better understanding of how the system responds to fluid disturbances. The exact fluid mechanical signal to which the animal behaviorally responds (usually by escaping) and the threshold of that signal have been particularly important questions. Before examining the fluid parameters that have been investigated as candidates, it is helpful to review basic fluid mechanics definitions of these parameters. In the following equations, standard index notation is used where *i* and *j* are each implied to be 1, 2, and 3 in a three dimensional coordinate system. For a given velocity field, any velocity gradient $\overline{\nabla}\bar{u}$ can be decomposed into a pure deformational component $\left[\frac{1}{2}\left(\frac{\partial u_i}{\partial x_j}+\frac{\partial u_j}{\partial x_i}\right)\right]$and a pure rotational component $\left[\frac{1}{2}\left(\frac{\partial u_i}{\partial x_j}-\frac{\partial u_j}{\partial x_i}\right)\right]$as follows:

$$\overline{\nabla}\bar{u}=\frac{\partial u_i}{\partial x_j}=\begin{bmatrix}\frac{\partial u_1}{\partial x_1} & \frac{\partial u_2}{\partial x_1} & \frac{\partial u_3}{\partial x_1}\\ \frac{\partial u_1}{\partial x_2} & \frac{\partial u_2}{\partial x_2} & \frac{\partial u_3}{\partial x_2}\\ \frac{\partial u_1}{\partial x_3} & \frac{\partial u_2}{\partial x_3} & \frac{\partial u_3}{\partial x_3}\end{bmatrix}=\frac{1}{2}\left(\frac{\partial u_i}{\partial x_j}+\frac{\partial u_j}{\partial x_i}\right)+\frac{1}{2}\left(\frac{\partial u_i}{\partial x_j}-\frac{\partial u_j}{\partial x_i}\right) \quad (1)$$

The deformation component is symmetric and is called the strain rate tensor (or the rate of deformation tensor) and may be represented as:

$$e_{ij} = \frac{1}{2}\left(\frac{\partial u_i}{\partial x_j} + \frac{\partial u_j}{\partial x_i}\right) = \begin{bmatrix} \frac{\partial u_1}{\partial x_1} & \frac{1}{2}\left(\frac{\partial u_2}{\partial x_1} + \frac{\partial u_1}{\partial x_2}\right) & \frac{1}{2}\left(\frac{\partial u_3}{\partial x_1} + \frac{\partial u_1}{\partial x_3}\right) \\ \frac{1}{2}\left(\frac{\partial u_2}{\partial x_1} + \frac{\partial u_1}{\partial x_2}\right) & \frac{\partial u_2}{\partial x_2} & \frac{1}{2}\left(\frac{\partial u_3}{\partial x_2} + \frac{\partial u_2}{\partial x_3}\right) \\ \frac{1}{2}\left(\frac{\partial u_3}{\partial x_1} + \frac{\partial u_1}{\partial x_3}\right) & \frac{1}{2}\left(\frac{\partial u_3}{\partial x_2} + \frac{\partial u_2}{\partial x_3}\right) & \frac{\partial u_3}{\partial x_3} \end{bmatrix} \quad (2)$$

The diagonal terms of the strain rate tensor represent extension or contraction ("linear" strain) of a local fluid element and are thus called "linear strain rates." The off-diagonal terms represent an angular squeezing or expansion ("shear" strain) and are therefore called "shear strain rates." The second (and anti-symmetric) component of the velocity gradient tensor $\overline{\nabla}\bar{u}$ is the rotational component $\frac{1}{2}\left(\frac{\partial u_i}{\partial x_j} - \frac{\partial u_j}{\partial x_i}\right)$. The elements of the rotation tensor then correspond to the vorticity vector $\bar{\omega} = \overline{\nabla} \times \bar{u}$ or$\omega_k = \frac{\partial u_j}{\partial x_i} - \frac{\partial u_i}{\partial x_j}$.

With these definitions in mind, one can then proceed to determine which fluid signal has been determined to elicit a response in copepods. Haury et al. (1980) first identified and investigated several possible stimuli that provoke escape responses in *Calanus finmarchicus.* These stimuli included pressure changes, acceleration, total fluid deformation, and deformation rate. These researchers hypothesized that a "rigid" copepod in a deforming fluid (or flow gradient) moves with the ambient flow, whereas its setae bend with the deforming flow. Their experiments showed that the deformation-associated quantities were the most likely candidates as mechanosensory cues that best explained behavior responses. Fields and Yen (1996, 1997) used siphon flows to mimic predator feeding currents and spatially quantified the associated flow and shear field. The locations of copepod escape responses in multiple species were recorded and related to various fluid signal parameters. The shear strain rate was found to be the least variable parameter that provoked an escape response, and the species-specific shear strain rate

threshold was found to vary from 1.5 to 51.5 s^{-1}. Kiørboe et al. (1999) also investigated the various components of a velocity gradient that a copepod might sense (acceleration, vorticity, linear strain rate, and shear strain rate) and concluded that strain rate was the most important flow characteristic. Furthermore, the estimated threshold for *Acartia tonsa* females was 0.4 s^{-1}, regardless of whether the copepod experienced pure linear or pure shear deformation. Kiørboe and Visser (1999) have further argued that only perception of predators by a copepod depends on the deformation rate whereas perception of prey (which are generally much smaller) depends solely on the absolute magnitude of the velocity produced by the moving prey. Visser (2001) also has extensively modeled the fluid mechanics of signal perception and reaction distance in the plankton for a variety of situations including feeding current generation, constant swimming at low and high *Re*, and a passive particle in a deforming flow and found that these models agreed reasonably well with existing data on reaction distances in copepods.

The extraordinary perceptive ability of the copepod sensory system is best exhibited in its ability to locate and attack prey and to escape from predators at a distance. Jiang and Paffenhöfer (2008) examined the attack kinematics and reaction distance of *Oithona plumifera* to motile *Strombilidium* ciliates. By overlaying ciliate hydrodynamics (calculated via CFD) onto the trajectory of the swimming ciliate, they were able to determine that the copepod is able to determine and project the ciliate's location and will wait for the ciliate to reach an optimal location for capture before initiating its attack. The fluid signals that the copepod responded to with an attack sequence varied greatly, with the smallest hydrodynamic signal of 12 μm s^{-1} being equivalent to a shear rate of 0.034 s^{-1} (over a setal length of 350 μm). Kerfoot (1978) and Kiørboe et al.(2009) have also

demonstrated the ability of copepods to localize a prey signal in 3D and to respond with a directed attack. In one instance, a copepod (*Acartia tonsa*) captured prey by turning 180° and rotating along its long body axis by 90° (Kiørboe et al., 2009).

The ability of copepods to accurately detect a predator or a predator mimic and appropriately respond with a directed escape response has been investigated by numerous researchers. Various stimuli used to induce escape behavior have included turbulence, various predators, siphons, and vibrating spheres, and many researchers have sought to find shear thresholds for these stimuli. Table 2.1 shows various studies in this vein, with the species, stimulus type, escape speed, and shear threshold (if found). One of the interesting behaviors learned from these studies was the ability of the animal to accurately localize the source of danger and to rapidly re-orient itself before performing the stereotypical escape jump sequence. For instance, Suchman (2000) found that *Acartia hudsonica* jumped away from a medusae predator most of the time. Buskey et al. (2002) also found that the copepods made an initial turn of 45-90° before jumping. In a study of force production during escape by a tethered animal, Lenz et al. (2004) also recorded preparatory movements likely corresponding to repositioning prior to the impulse of the escape jump. A reorientation before jumping was also seen in the studies by Burdick et al. (2007) and Kiørboe et al. (2010b), thus indicating that the animals could localize a hydromechanical signal indicating danger and respond with a directed jump away from that signal.

Table 2.1: Chronological list of papers examining sensitivity and escape reactions of various copepods (continued on next page)

Escaping Species	Stimulus	Escape speed (mm s^{-1})	Threshold Shear (s^{-1})	Authors	Year	Paper Title
Temora longicornis, Acartia clausii, Centropages hamatus, Portunus larvae, Tisbe furcata	Siphon tube			Singarajah	1975	Escape reactions of zooplankton: effects of light and turbulence
Centropages hamatus	Grid-generated turbulence		0.84 mm s^{-1} (minimum)	Hwang and Strickler	1994	Effects of periodic turbulent events upon escape reactions of a calanoid copepod
Pleuromamma xiphias	Siphon tube		7.2	Fields and Yen	1996	The escape response of *Pleuromamma xiphias* in response to a quantifiable fluid mechanical disturbance
Acartia tonsa adults	Siphon tube		1.5	Fields and Yen	1997	The escape behavior of marine copepods in response to a quantifiable fluid mechanical disturbance
Acartia tonsa nauplii			9.7			
Oithona			8.1			
Pleuromamma xiphia			7.2			
Euchaeta rimana			4.1			
Labidocera madurae			51.5			
Acartia	Siphon tube	55	Distance of 5 mm	Viitasalo and Rautio	1998	Zooplanktivory by *Praunus flexuousus*: functional responses and prey selection in relation to prey escape responses
Eurytemora affinis		41				
cladocerans			Unable to resist			
Acartia tonsa	various		0.5 - 5	Kiorboe, Saiz, and Visser	1999	Hydrodynamic signal perception in the copepod *Acartia tonsa*
Acartia hudsonica	Medusae (*Aurelia* and *Cyanea*)	33-59 (quite low)	distances of 4-10mm	Suchman	2000	Escape behavior of Acartia hudsonica copepods during interactions with scyphomedusae

Table 2.1 (continued)

Escaping Species	Stimulus	Escape speed (mm s^{-1})	Threshold Shear (s^{-1})	Authors	Year	Paper Title
Acartia	Siphon tube	40	3.9	Viitasalo, Flinkman, Viherluoto	2001	Zooplanktivory in the Baltic Sea: a comparison of prey selectivity by Clupea harengus and Mysis mixta, with reference to prey escape reactions
Eurytemora affinis		55	5.4			
Temora longicornis		43	10.4			
Pseudocalanus elongatus		47	14.1			
Acartia (tonsa and lilljeborgii)	Vibrating cylinder	~400	.4 - 12	Buskey, Lenz, and Hartline	2002	Escape behavior of planktonic copepods in response to hydrodynamics disturbances: high speed video analysis
Euchaeta rimana	Picojet			Fields and Yen	2002	Fluid mechanosensory stimulation of behaviour from a planktonic marine copepod, *Euchaeta rimana* Bradford
Acartia hudsonica	Vibrating cylinder / siphon tube	536 / 343	1.2 / .34	Burdick, Hartline, and Lenz	2007	Escape strategies in co-occurring calanoid copepods
Centropages hamatus		386 / 367	1.4 / 1.2			
Tortanus discaudatas		387 / 289	1.7 / 2.2			
Temora longicornis		262 / 244	>15 / 2.7			
Paracalanus parvus	Siphon tube		6.16	Waggett and Buskey	2007	Copepod escape behavior in non-turbulent and turbulent hydrodynamic regimes
Temora turbinata			3.93			
Paracalanus parvus	Predatory fish	253	1.74 mm (dist.)	Waggett and Buskey	2007	Calanoid copepod escape behavior in response to a visual predator
Temora turbinata		227	1.87 mm (dist.)			
Calanus	aquarium on speaker	100-250		Waggett and Buskey	2008	Escape reaction performance of myelinated and non-myelinated calanoid copepods

Table 2.1 (continued)

Escaping Species	Stimulus	Escape speed (mm s^{-1})	Threshold Shear (s^{-1})	Authors	Year	Paper Title
Calanus	northern krill pleopod beating	~150		Abrahamsen, Browman, Fields, and Skiftesvik	2010	The three-dimensional prey field of the northern krill, and the escape responses of their copepod prey
Oithona davisae	tap/pipette approach/ spontaneous	198		Kiorboe, Anderson, Langlois, Jakobsen	2010	Unsteady motion: escape jumps in planktonic copepods, their kinematics and energetics
Acartia tonsa		378				
Calanus finmarchicus		634				
Acartia tonsa		333		Jiang and Kiorboe	2011	Propulsion efficiency and imposed flow fields of a copepod jump
Calanus finmarchicus		756				

2.2.2. Daphniids

2.2.2.1. *Swimming*

Daphniids swim by periodically beating their second antennae. The second antennae are biramous such that the protopodite splits or branches into an exopodite and an endopodite. These two branches are spread during the power stroke and collapsed near the body during the recovery stroke (Kohlhage, 1994). Kohlhage (1994) found the stroke cycle of *Daphnia magna* lasted approximately 80 ms and that this time was evenly split between the power and recovery strokes. Daphniid stroke kinematics have not been quantified, but the stroke kinematics of a smaller cladoceran with similar swimming behavior, *Bosmina longirostris*, were quantified by Zaret and Kerfoot (1980). Dodson et al. (2010) recently commented that the daphniid "hopping motion has not yet been satisfactorily characterized."

Scourfield (1900) found that the antennal stroke plane did not align with the long axis of the body but was instead slightly inclined such that water was pushed dorsally backwards during the power stroke. The animal then was propelled forward but also rotated nose-down. Gravity then righted the animal while it was sinking such that its long axis aligned with the gravitational vector. Animal morphology and especially the location of the center of mass may then play an important role in determining swimming behavior. Jacobs (1964, 1967) found that animals with elongated cyclomorphic helmets swam more horizontally, presumably because an upward shift in the center of mass slowed the rotation of the animal while sinking. Fox and Mitchell (1953) also speculated that the

added weight of the ephippium (egg pouch) on the back of female daphniids changed the animal's center of mass and necessitated an increased antennal beat rate.

Swimming in daphniids can be divided into the normal 'hop and sink' swimming behavior, which is somewhat similar to the hopping of cyclopoid copepods, and a fast-swimming escape response. In hop and sink swimming, a power stroke that rapidly carries the animal forward approximately one body length is followed by a period of sinking. Jacobs (1964) found that, during normal swimming, the antennae were active for only 11-13% of the swimming time and that they acted as 'braking parachutes' for the remaining time. Instantaneous speeds during the power stroke may reach up to 60 mms^{-1} as calculated from Dodson and Ramcharan (1991), but average swimming speed under normal conditions is in the range of 0.5 to 8 mms^{-1}(Li and Li, 1979; Porter et al., 1982; Riessen et al., 1984; Dodson and Ramcharan, 1991; Dawidowicz and Loose, 1992; Cuddington and McCauley, 1994; Dodson et al., 1995; Gorski and Dodson, 1996; Dodson et al., 1997a, b; Pijanowska and Kowalczewski, 1997; O'Keefe et al., 1998; Brewer, 1998; Baillieul and Blust, 1999; Weber and van Noordwijk, 2002; Seuront et al., 2004; Ziarek et al., 2011). Swimming speed also scales with animal size, with larger animals able to attain higher speeds (Dodson and Ramcharan, 1991; Bailleul and Blust, 1999). The antennal beat frequency during normal swimming is in the range of 1.5 to 6 Hz (Fox and Mitchell, 1953; Porter et al., 1982; Kirk, 1985; Dodson and Ramcharan, 1991; Dawidowicz and Loose, 1992; Dodson et al., 1995; Gorski and Dodson, 1996; Bailleul and Blust, 1999). Fox and Mitchell (1953) found that antennal beat frequency increased with the number of eggs carried in the brood chamber. Studies have also shown

that, quite unusually, antennal beat frequency is independent of animal size (Dodson and Ramcharan, 1991; Bailleul and Blust, 1999).

Escape swimming in daphniids is characterized by high speed and antennal beat frequency, with no sinking between strokes (Dodson et al., 1997a). Brewer et al. (1999) defined escape swimming as having a speed greater than 10 mms^{-1}. Researchers have found maximum escape speeds of 40 mms^{-1} for *Daphnia pulex* (Browman et al., 1989; Chang and Hanazoto, 2003), 140 mms^{-1} for *Daphnia pulicaria* (Brewer et al., 1999), and 32 mms^{-1} for *Daphnia ambigua* (Chang and Hanazoto, 2003). Kirk (1985) found that antennal beat frequencies in *Daphnia pulex* during escape may reach up to 23 Hz. Distances traveled by escaping daphniids range from 4.5 mm (Browman et al., 1989) up to approximately 40 mm (Brewer et al., 1999). Escape swimming in daphniids at times may also be characterized by a looping, spinning, or spiraling swimming pattern. Li and Li (1979) found that *Daphnia pulex* swam in a somersaulting loop to avoid a predatorial copepod. Dodson et al. (1995) found a similar spinning motion in *Daphnia pulex* when the animals escaped from a fish. Pijanoska and Kowalczewski (1997) found that *Daphnia magna* performed somersaults more often in response to fish kairomones, and several other researchers have noted the presence of escape behavior without detailed descriptions of the swimming pattern (Szlauer, 1964; O'Brien and Vinyard, 1978; Riessen, 1982; Riessen et al., 1984; Kirk, 1985; Dodson and Ramcharan, 1991; O'Keefe et al., 1998; Brewer, 1998; Seuront et al., 2004; Pijanowska et al., 2006). As noted by Scourfield (1900), this somersaulting behavior is likely due to the high antennal beat rate. Without a pause for sinking and realigning with gravity between antennal strokes, the animal drives itself in a circle (Scourfield, 1900).

The fluid physics of daphniid swimming has been investigated very little. Dodson and Ramcharan (1991) estimated the Reynolds number of hop and sink swimming to range up to 15. Kirk (1985) used a hot-wire anemometer to measure flow speeds near free-swimming *Daphnia pulex* and found a maximum speed of 182 mms^{-1}. Flow speeds in the range of 1 to 10 mms^{-1}were also measured around tethered *Daphnia* (Kirk, 1985). Kohlhage (1994) performed flow visualization with ink on a tethered *Daphnia magna*, but tethering has been shown to irrevocably alter the flow field (Catton et al., 2007). The fluid physics of daphniid swimming has been visualized via Schlieren optics using a density gradient by several researchers (Kerfoot et al., 1980; Brewer, 1998; Gries et al., 1999). Kerfoot et al. (1980) visualized the flow around a hopping juvenile and stated that it creates "an indistinct wake that quickly disappears." Brewer (1998) showed that the hydrodynamic disturbance (the wake) of a daphniid persisted for several body lengths behind the animal. Gries et al. (1999) described the downward flow from the 'hop and sink' antennal stroke forming a toroidal vortex (upside down mushroom shape). This flow feature was attributed to the less dense water beginning to rise after being pushed downward by the animal. No work has yet attempted to quantify the flow physics of daphniid swimming.

2.2.2.2. *Feeding*

Daphniids generate a feeding current that draws water through the ventral opening of their carapace and into a filtering chamber. In a 2 – 3 mm Daphnia, the flow speed at the intake is approximately 1.5 cms^{-1}. As observed by Scavia et al. (1984), the excurrent is

directed downward through the same ventral opening. Multiple appendage pairs inside the filter chamber generate the feeding current and capture food particles (Gerritsen et al., 1988). Penalva-Arana et al. (2007) found that males have a higher appendage beat frequency (5 Hz) than females (3.3 Hz) and that the beat became more irregular in the presence of food. Visualization with Schlieren optics has shown that the outflow is a pulsed current (Penalva-Arana et al., 2007). In contrast with calanoid copepods, the feeding current does not seem to be integrated to play a role in sensing mechanical disturbances as well as in gathering food.

2.2.2.3. *Sensing*

Like copepods, daphniids sense their environment through chemo- and mechanosensory means. Vision also plays a role in daphniids. In comparison to copepods, however, the sensory capabilities of daphniids are much less well studied and understood.

Chemosensing in daphniids is accomplished through the small first antennae (Dodson et al., 2010). Chemical scents released from predators, such as fish, have been shown to modify daphniid swimming behavior and to increase their wariness of predators. Dodson et al. (1997b) showed that a greater percentage of daphniids swam downwards (to avoid visual predators) at a higher speed when fish smell was present. Pijanowska and Kowalczewski (1997) showed that exposure to fish kairomones induced aggregation, caused the animals to swim significantly slower (to reduce contact rate with predators), and induced more escape events. Pijanowska et al. (2006) also showed that daphniids, pre-sensitized to fish and insect larvae scent, survived exposure to those predators better

than control animals. Kairomone-treated daphniids also were shown to respond more sensitively to mechanical signals and to survive predation by guppies better than control animals (Brewer et al., 1999). Sensitivity to these chemical signals has also been shown to be highly clone-specific, with some types of daphniids exhibiting no response to kairomones (Pijanowska and Kowalczewski, 1997; Brewer et al., 1999).

The sensitivity of daphniids to hydrodynamic signals is not well understood, but there is evidence that daphniids do respond to mechanical disturbances in the water. The mechanism by which daphniids sense hydrodynamic disturbances has not been investigated, but the setae on the second antennae could possibly provide this capability. Szlauer (1964) examined the response of *Daphnia* to the approach of other daphniids, a glass wand, or a stream from a pipette. Female daphniids avoided other daphniids from a distance while male daphniids detected other daphniids from a distance and pursued them in an attempt to mate. The same response was seen with the approach of a glass wand. Streams of water passing "at a considerable distance" also evoked a strong avoidance reaction in female *Daphnia* (Szlauer, 1964). The number of animals caught in a tube lowered at different speeds also provided Szlauer (1964) with a measure of daphniid sensitivity to fluid disturbance. More animals were caught at high (52 cms^{-1}) and low (0.33 cms^{-1}) speeds than at medium speeds. This bimodal distribution could indicate a shear threshold necessary to evoke a response from the animals. More animals also were caught when the tube was lifted from the bottom than when it was lowered from the top, possibly indicating a directional sensitivity to disturbance in the water. The second antennae, which could be used in mechanoreception, are located anteriorly and could provide an earlier warning for dangers from above than below. Many more animals were

also caught in dark conditions than in light conditions, indicating that vision plays a role in evasive abilities (Szlauer, 1964). Li and Li (1979) indicated that *Daphnia pulex* individuals escaped much more strongly from nearby predators than from conspecifics, thus indicating a possible ability to recognize and differentiate between hydrodynamic signals of varying strengths. Riessen (1982) stated that *Daphnia* sometimes jumped away from an approaching predator (the water mite *Piona constricta*), thereby indicating an ability to detect hydrodynamic signals. Browman et al. (1989) quantified the distance between a *Daphnia* and a predatorial *Leptodora* at the instance of daphniid escape and found this distance ranged from 4.7 to 7.7 mm for adult daphniids and 3 – 6 mm for juvenile daphniids. For comparison, the copepods *Diaptomus* and *Mesocyclops* escaped at a smaller distance to the predator (1.5 – 5.9 mm). Brewer (1998), in a study of cladoceran mating, showed that males (*Daphnia pulicaria*) began pursuit of conspecifics at a mean distance of 3.85 mm (range from 0.3 to 6.4 mm, where 6.4 mm represents four body lengths). Brewer et al. (1999) investigated the escape response of *Daphnia* to a 4.3 mm diameter sphere dropped from above at a speed of 60 mms^{-1}, a stimulus similar to the attack of a ram-feeding fish. The flow speed due to the dropping sphere was calculated at the point of the animal. The most sensitive animals responded to flow speeds of approximately 0.4 mms^{-1}, but no attempt to calculate strain rate. Furthermore, this response was increased in response to predator kairomones, thus indicating that the sensitivity of *Daphnia* to hydromechanical stimuli is mediated by chemical means. Finally, animals that had been exposed to predator kairomones did not exhibit an increased tendency to escape when exposed to crowded conspecifics, thereby indicating an ability to distinguish signals of varying magnitudes (Brewer et al., 1999). Daphniids

therefore seem capable of detecting hydromechanical signals generated by a predator or conspecific at a distance, but the characteristics of that signal remains unknown. No attempt has been made to obtain a shear rate threshold for cladocerans as several similar attempts have been made for copepods.

2.2.3 Krill

2.2.3.1 *Swimming*

Swimming in krill is accomplished by rapid metachronal beating of five sets of oar-like swimming legs known as pleopods (Kils, 1981). Krill, or euphausiids, are generally highly motile, and the largest euphausiid, the Antarctic krill, has been classified as nekton rather than plankton for its excellent swimming ability. Many species of krill exhibit diurnal vertical migration over several hundred meters (Nicol and Endo 1997). In addition, schools of *E. superba* have been observed migrating at an average rate of 12 kilometers per day over the course of several days (Kanda et al. 1982). Krill also are known to hover and 'parachute' (Kils 1981) and to swim upside down as they feed on algae on the underside of ice sheets (Stretch et al. 1988).

2.2.3.2 *Sensing*

Hydrodynamic signals are thought to be an important part of euphausiid behavior and are thought to play a role in schooling in Antarctic krill (Hamner et al., 1983; Hamner, 1984; Wiese and Marschall, 1990; Wiese and Ebina, 1995; Wiese, 1996) but have not been

investigated in great detail. Krill have three sets of antennules that are oriented in different directions and can sense high frequency (>40 Hz) flow disturbances (Patria and Wiese, 2004). Bending at the antennule base can sense fluid disturbances in the range of 5 – 40 Hz, thereby providing flow sensitivity over a wide range of frequencies. The velocity threshold for Antarctic krill has been found to be as low as 0.15 mm s^{-1}. (Patria and Wiese, 2004).

CHAPTER 3

METACHRONAL KINEMATICS OF ANTARCTIC KRILL

Metachronal swimming, in which adjacent appendages stroke in sequence, is widespread among crustaceans inhabiting the transitional flow realm in which both viscosity and inertia effects are important. However, the design and operation of this propulsion system in response to various hydrodynamic, energetic, and behavioral needs have not been well investigated. We examine free-swimming Antarctic krill (*Euphausia superba*) as a model species and identify three distinct behavioral swimming gaits. The pleopod kinematics of these gaits, hovering, fast forward swimming, and upside down swimming, are quantified via image analysis of high-speed video. Pleopod stroke amplitude and frequency were found to vary significantly among these swimming modes. In order to increase swimming speed, krill were found first to increase beat amplitude and secondarily to increase beat frequency. The kinematics of these distinct swimming modes provide insight as we consider multi-appendage metachronal swimming from a design standpoint. The ratio of the distance between adjacent appendage bases and appendage length is identified as a key parameter in metachrony, the value of which is constrained to a narrow range for a wide variety of species.

3.1. Introduction

Free-swimming crustaceans such as krill, mysids, and remipedes are characterized by multiple pairs of closely spaced swimming appendages. Since the spacing between these leg pairs is generally too small to allow independent operation of each pair without interference, the question is raised: How does an animal move its multiple sets of legs to efficiently accomplish propulsion? Coordination between leg pairs is required to avoid interference between adjacent appendages. Almost all free-swimming crustaceans have settled on some version of metachronism as the solution to this challenge.

In metachronism, periodically stroking appendages are phase-shifted in time relative to the neighboring appendage, resulting in a wave of appendage motion traveling along the body. In crustaceans, the appendages usually move in an adlocomotory sequence, in which the wave travels in the same direction as the animal (Knight-Jones and Macfadyen 1959). In the most basic form of adlocomotory metachronism, the posterior pair of swimming legs initiates a power stroke and is followed at some phase lag by its adjacent leg pair. This sequence continues until all legs have stroked. At some phase lag after the anterior-most pair has stroked, the posterior pair, having already performed a recovery stroke, begins a new power stroke. The overall effect is that of a wave passing from back to front along the animal. In addition to the advantage of avoiding interference between adjacent legs, this technique is thought to increase propulsive efficiency by accelerating water to a greater velocity than would be possible with a single appendage (Sleigh and Barlow 1980). Indeed, a recent model of krill pleopod motion by Alben et al. (2010) showed that a metachronal stroke (as opposed to a synchronous or intermediate stroke) gave the largest average body speed.

One aspect of the metachronal propulsion system that remains relatively unexplored is how it adapts to different locomotory needs. Swimming crustaceans may at different times need to hover, accelerate, escape, migrate long distances, feed, and navigate unfamiliar substrate. The kinematic and thus the hydrodynamic features of a metachronal propulsion system could thus be expected to have some adaptive ability for these exigencies. Linking specific kinematics with certain swimming modes is challenging, however, as it often requires high-speed filming of free-swimming animals behaving normally in order to first identify distinct modes and then to characterize the associated kinematics for those modes. In copepods, distinct cruise and escape swimming modes have been identified and their kinematics characterized (van Duren and Videler 2003). These animals, however, use different sets of appendages for different swimming modes (Borazjani et al. 2010). There is thus a need to examine the adaptability of a single set of metachronally operating swimming appendages, especially in larger crustaceans in which the swimming modes are not as well described. For instance, only a few researchers have commented on different swimming modes (e.g., Kohlhage and Yager 1994; Tarling and Johnson 2006) or investigated a link between stroke kinematics and animal speed (e.g., Kils 1981; Alexander 1988; Swadling et al. 2005). The aim of this chapter therefore is to examine the behavior of the Antarctic krill (*E. superba*) in order to identify and characterize distinct metachronal swimming gaits associated with certain behaviors. The design elements contributing to the success of the krill's metachronal propulsion system also will be considered.

E. superba is an ideal choice to study various metachronal swimming gaits because it is a highly motile pelagic species. For instance, many species of krill exhibit diurnal vertical

migration over several hundred meters (Nicol and Endo 1997). In addition, schools of *E. superba* have been observed migrating at an average rate of 12 kilometers per day over the course of several days (Kanda et al. 1982). Krill also are known to hover and 'parachute' (Kils 1981) and to swim upside down as they feed on algae on the underside of ice sheets (Stretch et al. 1988). Each of these behaviors would seem to have distinct hydrodynamic characteristics and requirements that should be reflected in distinct metachronal swimming gaits.

3.2. Materials and Methods

3.2.1. Experiment Description

Euphausia superba were filmed during the austral winter of 2008 at the Australian Antarctic Division (AAD) in Kingston, Tasmania, Australia where several thousand animals are regularly maintained in a number of tanks with volumes ranging up to 1806 L (Kawaguchi et al. 2010). Krill filmed in this study included both males and females at various stages of development and several juveniles. Johnson and Tarling (2008) found significant differences in beat frequency with gender and molt stage in *E. superba*. Females had a higher beat frequency but stroked with less power, a trend possibly related to the less rigid pleopod cuticle in females. These differences (up to 1 Hz in pleopod beat frequency) were greatest for large adult animals. The animals used in this study were somewhat smaller and no difference was observed in beat frequency, hence no distinction based on gender was made in subsequent analysis. Animals to be filmed were transferred to one of two custom-built aquaria. The larger tank, with a volume of roughly 100 L, was

cylindrical with a window pane on the side to allow filming. The smaller tank was approximately cubical with a volume of about 8 L and allowed optical access from two orthogonal tank sides. Two walls of this aquarium were double-paned. In order to maintain the temperature of the water at 0.5°C, chilled water continuously ran through the outer compartment. Because the water temperature in the un-chilled (larger) aquarium increased with time, filming sessions lasted no more than about thirty minutes (including several minutes at the beginning in which the animals were allowed to acclimate to the aquarium). Up to twenty animals were placed in the large aquarium and four to eight were placed in the small aquarium during a filming session. To commence filming, the aquarium was brightly lit with a halogen lamp. A high-speed camera with an 800 x 600 pixel array (AOS X-PRI from AOS Technologies, Baden Daettwil, Switzerland) and a 50 mm lens (Navitar, Rochester, NY, USA) was aimed through one of the aquarium walls. The camera was manually triggered when an animal swam into the field of view and filmed at 250 fps. Dimensional calibration was accomplished by photographing a ruler that was temporarily mounted in the tank. In a few cases, the fluid flow was visualized by the addition of a small volume of concentrated phytoplankton (*Pyramimonas gelidicola*).

Animals often swam along the edge of the aquarium near the water surface, providing a clean lateral view for the camera. In all, 120 video sequences were collected, of which about 40 were selected for further analysis. The selected video sequences were those in which the camera had a clear lateral view of the animal and the animal performed at least one complete stroke cycle. The sequences contained between one and fifteen consecutive stroke cycles. Video sequences in which an individual animal displayed multiple

swimming modes were split accordingly, resulting in a total of 55 isolated video sequences.

3.2.2. Image analyses

All image analyses were performed using ImageJ (National Institutes of Health, USA). For each video sequence, swimming speed, animal length (eyeball tip to end of telson), and body angle relative to the horizontal water surface (measured from a line fitted by hand to the pleopod bases) were measured. Extreme curvature of the abdomen, which could affect the body angle measurement, was seen rarely, although some curvature of the abdomen seemed to be associated with upside down swimming. These parameters were used to classify the video sequences into three main swimming modes (hovering, fast forward swimming, and upside down swimming), which will be detailed subsequently. A subset of video sequences within each category was then selected for further kinematic analysis. The following three points on each pleopod were manually located in each still frame of the sequence: the pleopod base, the joint between the protopodite and the endo/exopodite, and the endopodite tip. Of primary interest was the angle between the long axis of the body and the pleopod pair, the pleopod angle α (see Figure 3.1). One arm of this angle was obviously the ray between the pleopod base and the middle pleopod joint. The other arm consisted of the ray between the pleopod base and the pleopod base of the next most anterior pleopod. In calculating α for the most anterior pleopod pair, the ray from the second pleopod pair to the first was used. The second angle of interest was the interior angle between the protopodite and the

endo/exopodite, denoted β (see Figure 3.1). Approximately 4600 frames representing 18.2 seconds of data were analyzed in this manner.

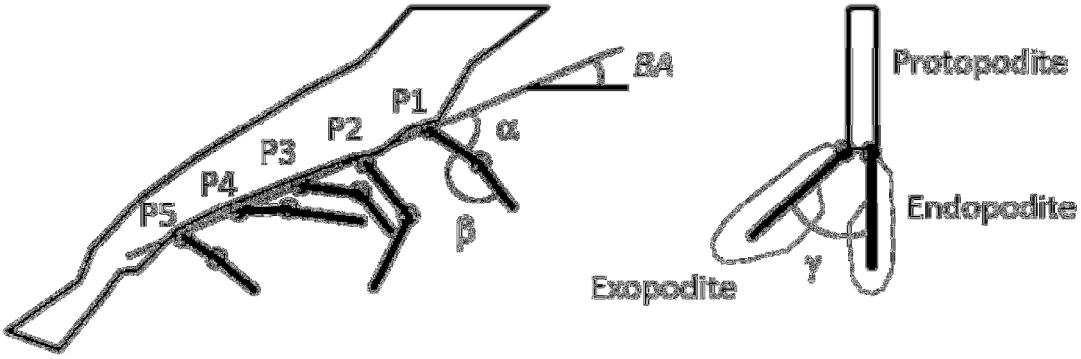

Figure 3.1 Diagram showing the various measured angles. The diagram on the left is a lateral view of the animal. The diagram on the right is a view of a left pleopod from the animal's posterior such that the exopodite extends to the left. α is the angle between the protopodite and the long axis of the body. β is the angle between the protopodite and the endopodite and exopodite. γ is the angle between the exopodite and endopodite. *BA* is the angle of the body with respect to horizontal. Pleopods are numbered one through five, anterior to posterior, and are abbreviated P1 to P5

For data sequences in which multiple stroke cycles were recorded, the pleopod angle time series were divided and phase-averaged (temporally aligning from the initiation of the power stoke) to produce one standard cycle (for both α and β) for each pleopod pair. The number of data points in this cycle naturally depended on the animal's beat frequency. The pleopod angle data then were time-standardized by scaling to the mean beat duration for each behavioral gait. Cubic spline functions were fit to each time-standardized record using the splinetool function in Matlab (Mathworks, Natick, MA, USA), and 100 equally-spaced points were calculated based on the fitted functions. The equally-spaced points from each video sequence were averaged to produce the mean pleopod angle curves for

each gait for both α and β. As an example, Figure 3.2 shows six time-standardized profile curves (from different video sequences) for the fourth pleopod angle α, where α = 0° corresponds to the pleopod pointing forward and α = 90° corresponds to the pleopod aligning approximately perpendicular to the body. The mean and standard deviation of the spline functions are also shown.

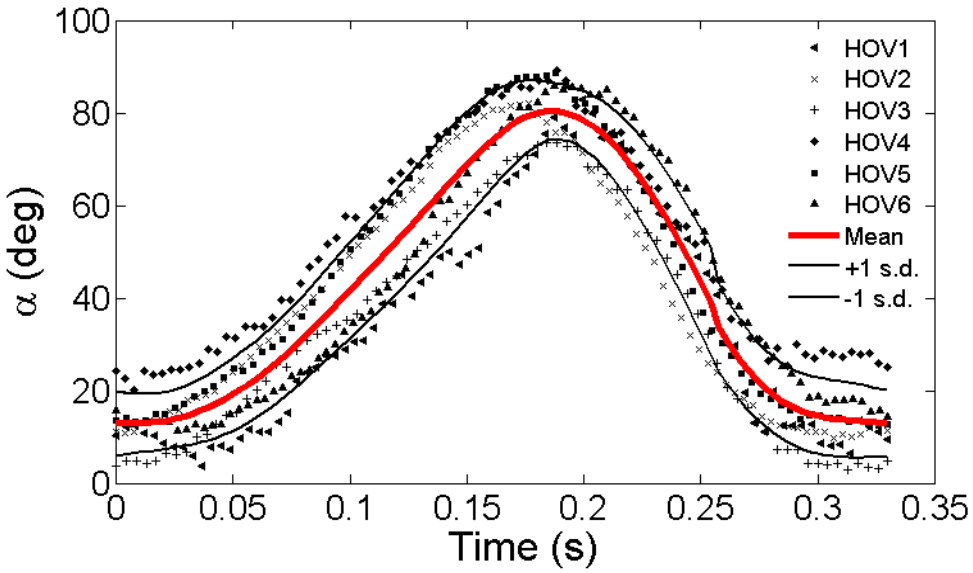

Figure 3.2 Six time-standardized records (HOV1 – HOV6) for P4 angle α. The mean and standard deviation of the smoothing splines fit to these data are also shown

3.2.3. Statistical Analysis

In order to perform statistical tests comparing various kinematic parameters (pleopod stroke magnitude, beat frequency, and phase lag between consecutive pleopod strokes) among the three swimming modes, the data sets were tested for normality (by an Anderson-Darling test) and for equal variances (by Bartlett's and Levene's tests) in

Minitab. The variance of beat frequency (but not beat magnitude or phase lag) was found to vary significantly among swimming modes. A Kruskal-Wallis test therefore was used to determine if beat frequency significantly differed among swimming modes. All kinematic parameters (except for the phase lag between the fourth and fifth pleopods in the upside down swimming mode) met the requirements for normality, and a one-way ANOVA test therefore was performed on each of these parameters. If a significant difference was found between the population means, then multiple comparison t-tests with a Bonferroni correction were applied to compare between swimming modes. The Bonferroni correction divides the chosen significance level by the number of comparisons to find a corrected significance level. With a chosen significance level of 0.05 and comparisons among three swimming modes, the corrected significance level was 0.017.

3.3. Results

3.3.1. Behavioral Classification

Krill swimming video sequences were classified into three distinct swimming behaviors by plotting normalized velocity (body lengths per second) versus the body angle (Figure 3.3D). The swimming behaviors were defined as hovering (Figure 3.3A), fast forward swimming (Figure 3.3B), and upside down swimming (Figure 3.3C). Hovering (HOV) was defined as those instances when the normalized krill body speed was less than half of a body length per second with a body angle (relative to the surface) in the range of 25 - 50°. Upside down swimming (USD) was identified from the cluster of points in Figure

3.3D where the body angle is approximately 125° and the absolute normalized body speed is in the range of 1.3-2.2 body lengths per second. At the lower speeds characteristic of hovering and upside down swimming, only certain combinations of body angle and normalized speed satisfy the animal's requirement for equilibrium weight support; relatively tight clustering of data points is therefore expected (and observed) for these swimming modes. Fast forward swimming (FFW) was defined as the case where the normalized body speed was greater than 2 body lengths per second, with no restriction on body angle. Since at these higher speeds the animal may swim in any direction without regard to equilibrium weight support, no clustering of points was expected for this swimming mode. A transitional region between hovering and fast forward swimming was identified in the range of 0.5-2 body lengths per second. Body angle, in the range from 10-50°, appears to decrease with increasing normalized speed across the hovering and transitional regimes, a trend also seen for *E. pacifica* by Miyashita et al. (1996). The morphological parameters for the video sequences included in this analysis are shown in Table 3.1.

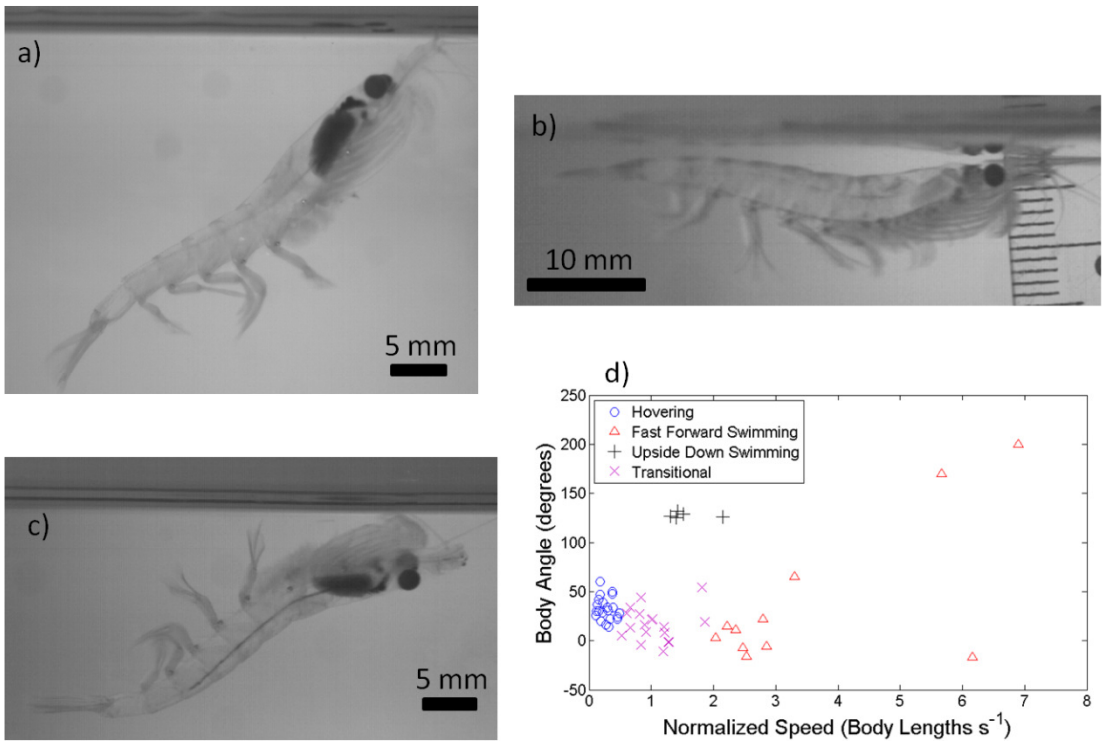

Figure 3.3 Three swimming modes defined by plotting normalized speed versus body angle. (a) Photographic example of hovering (HOV); (b) Photographic example of fast forward swimming (FFW); (c) Photographic example of upside down swimming (USD); and (d) Plot of normalized speed versus body angle demonstrating the differing regimes of behavior. The mean body length (± s.d.) was 3.4 ± 0.9 cm

Table 3.1 Morphometric and swimming speed data for *E. superba* for various swimming modes (HOV, hovering; FFW, fast forward swimming; USD, Upside down swimming); BL = body length; n = beat frequency; V = swimming speed; V_n = normalized swimming speed; BA = body angle

Individual	Cycles	BL (cm)	*n* (Hz)	*V* (cm s^{-1})	V_n (BL s^{-1})	BA (°)
HOV1	1	4.1	3.0	0.4	0.11	26
HOV2	15	4.1	3.0	0.5	0.12	30
HOV3	4	3.1	3.1	0.6	0.19	20
HOV4	2	4.1	2.9	0.9	0.21	29
HOV5	6	4.1	3.3	1.8	0.45	24
HOV6	7	3.9	2.7	1.7	0.45	22
HOV mean (sd)		3.9 (0.4)	3.0 (0.2)	1.0 (0.6)	0.25 (0.2)	25 (4)
FFW1	2.5	4.6	4.5	9.2	2.0	3
FFW2	1.5	4.2	4.0	10.5	2.5	-16
FFW3	2	4.3	6.0	12.0	2.8	22
FFW4	2	4.0	4.4	11.4	2.8	-6
FFW5	2.5	3.7	4.8	12.3	3.3	65
FFW6	1	4.4	6.1	25.0	5.7	170
FFW7	2.5	1.0	7.9	6.0	6.2	-17
FFW8	3	2.0	7.5	13.9	6.9	200
FFW mean (sd)		3.5 (1.3)	5.6 (1.5)	12.6 (5.6)	4.0 (1.9)	53 (86)
USD1	1	3.8	3.2	5.0	1.3	127
USD2	2.5	3.7	3.5	5.2	1.4	125
USD3	2	4.2	3.6	5.9	1.4	132
USD4	3	3.8	3.0	5.7	1.5	129
USD5	4	2.0	5.0	4.3	2.1	126
USD mean (sd)		3.5 (0.8)	3.7 (0.8)	5.2 (0.6)	1.6 (0.3)	128 (3)

3.3.2. General Description of Single Pleopod Stroke

Figure 3.4 reports the relationship between α and β throughout a complete stroke cycle. These data correspond to the second pleopod (P2) of a 3.2 cm krill swimming at 7 cm s^{-1}. Also shown is γ, the internal angle between the endopodite and the exopodite, defined in Figure 3.1. This angle was measured in one experiment in which two synchronized high-speed cameras with identical frame capture rates captured orthogonal views of a swimming krill. The angle γ was measured in images from the camera with a posterior view. The data allowed estimation of the time points at which exopodite abduction and adduction began but did not allow measurement throughout the entire power stroke.

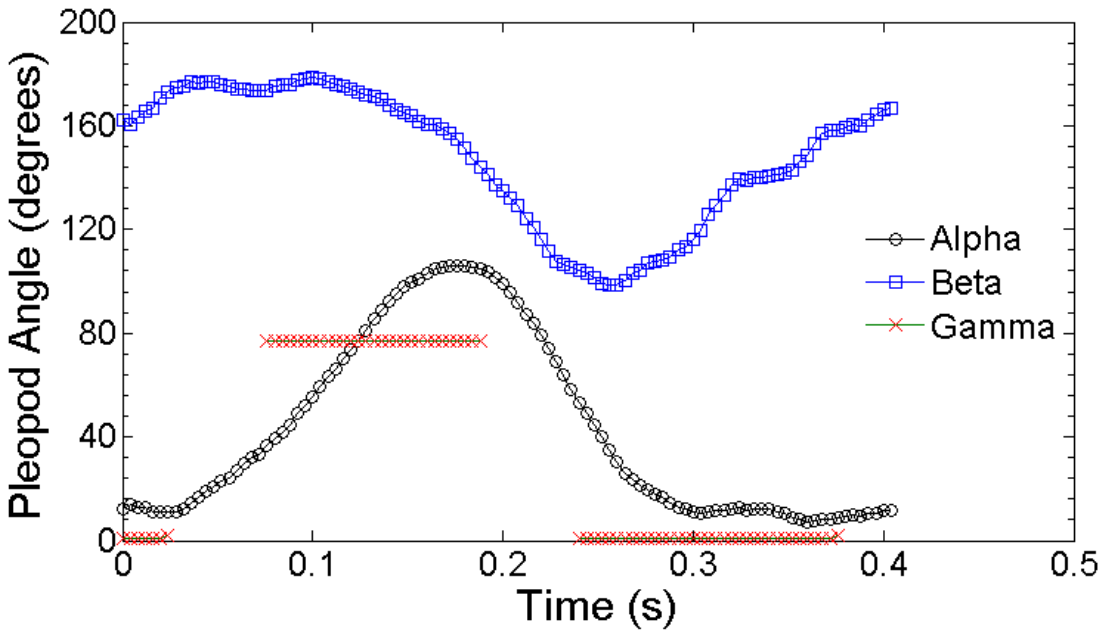

Figure 3.4 Record of pleopod angles α, β, and γ through one stroke cycle for the second pleopod (P2) of a fast forward swimming krill swimming at 2.2 body lengths per second

At the beginning of the power stroke, α is small (~15°) as the protopodite lies close to the krill's body. As the power stroke begins and α increases, the drag on the endopodite and exopodite push β to its maximum (near 180°). The exopodite simultaneously begins its abduction, thereby increasing γ. At 20% through the cycle (t = 0.07 s), the exopodite is at its maximum position (γ ~77°) where it remains throughout the power stroke. At the end of the power stroke (about 50% of the stroke cycle, t = 0.18 s), the exopodite adducts and the pleopod comes into contact with its posterior neighbor. The return stroke then begins, corresponding to decreasing α. The angle β decreases as the distal leg segments fold over those of their posterior neighbors. Midway through the return stroke (t = 0.26 s), the distal leg segments contact the anterior pleopod. The angle β then begins to increase as the distal leg segments unfold to prepare for the next power stroke.

3.3.3. Kinematics

Figure 3.5 shows time sequences for mean α and β for all five pleopods for the three swimming modes identified in *E. superba*. The mean stroke period in the hovering gait was 0.33 s (equivalent to a beat frequency of 3.0 Hz). In the hovering gait, all five pleopods reach a minimum α of approximately 12°. The maximum α varies with the pleopod position. Pleopod 5 (P5) reaches 86° and thus has the greatest amplitude. More anterior pleopods stroke with progressively smaller amplitudes until P1, which has a maximum α of 62°. The β angle in the hovering gait consistently reaches a maximum of about 172° for all five pleopods. Minimum values for β increase slightly from posterior (117° for P5) to anterior (125° for P1).

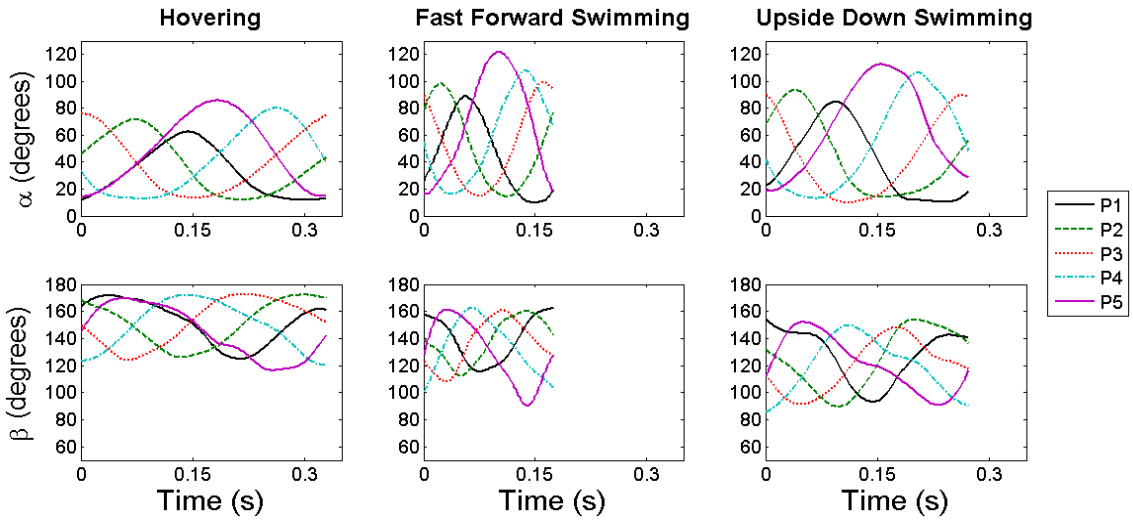

Figure 3.5 Time-standardized records of the mean pleopod angles α and β for hovering, fast forward swimming, and upside down swimming

In the fast forward swimming gait, the mean stroke period was shorter at 0.17 s (equivalent to a beat frequency of 5.9 Hz). The five pleopods reach a minimum α of approximately 15°. The most posterior pleopod, P5, reaches a maximum α of 121°. Values of α decrease anteriorly until P1, which has a maximum α of 88°. The maximum angle β for all pleopod pairs for fast forward swimming is approximately 160°. Minimum values for β increase anteriorly from 92° for P5 to 117° for P1.

In the upside down swimming gait, the mean stroke period was 0.27 s (equivalent to a beat frequency of 3.7 Hz). The minimum value for α was approximately 14°. The posterior-most pleopod pair (P5) reached a maximum α of 112°. Values of α decreased anteriorly to P1, which has a maximum α of 85°. The maximum angle β for all pleopod pairs for upside down swimming is approximately 150°. Minimum values for β generally increase anteriorly from 86° for P5 to 91° for P1.

Figure 3.6 compares the stroke amplitudes of all pleopods for each of the three swimming gaits. In each of the gaits, P5 has the largest stroke amplitude. Stroke amplitude then decreases anteriorly. The ANOVA tests indicated a significant difference ($F = 16.9, 25.3, 21.2, 31.7, 18.7$ for P1 to P5, respectively; $p < 0.05$) in stroke amplitude for each pleopod (P1–P5) when comparing among swimming modes. Multiple comparison t-tests with a Bonferroni correction showed that, for each pleopod (P1–P5), the stroke amplitude for hovering was significantly different from the amplitudes of the fast forward swimming mode ($p < 0.017$). For pleopods one through four, the hovering stroke amplitude was significantly different from the amplitudes of the upside down swimming mode ($p < 0.017$). The difference was not statistically significant in the amplitude of pleopod five when comparing these two swimming modes. The stroke amplitudes were not significantly different when comparing the fast forward and upside down swimming gaits.

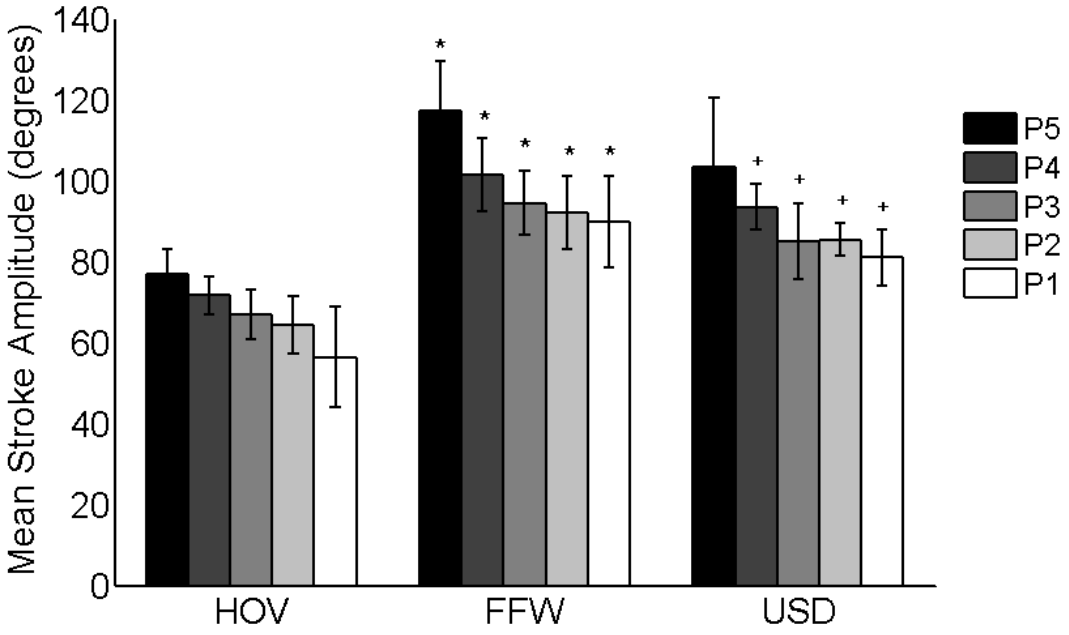

Figure 3.6 Mean stroke amplitude for each pleopod for hovering (HOV), fast forward swimming (FFW), and upside down swimming (USD). Error bars indicate standard deviation. An asterisk (*) indicates a significant statistical difference between data for HOV and FFW and + indicates a significant statistical difference between data for HOV and USD. No significant differences were observed when comparing the data for FFW and USD.

A Kruskal-Wallis test showed that a significant difference existed between the beat frequency of each swimming mode ($p < 0.05$), and the multiple comparison t-test with Bonferroni correction showed that the beat frequency of hovering was significantly different from that of fast forward swimming ($p < 0.017$).

Figure 3.7 shows the mean phase lags for the three swimming gaits described in this work. Phase lag was defined as the time period between the initiation of consecutive pleopod power strokes normalized by the time of the complete cycle. Phase lag is reported as fraction of a complete cycle. In a perfectly metachronal system with five leg

pairs, the phase lag between the initiation of each consecutively stroking leg pair would be 0.2. In this case, the fast forward swimming gait approximates metachrony fairly well. In hovering and upside down swimming, however, the phase lag between P1 and P5 is less than 0.2, indicating that the posterior leg pair is beginning a new stroke earlier than expected for metachrony. This deviation is especially pronounced in hovering, for which the mean phase lag between P1 and P5 is 0.1. In some individual cases, the first and last leg pairs beat in almost exact synchrony. The ANOVA test showed that significant differences existed among the three swimming modes for the P5-P4, P2-P1, and P1-P5 pleopod phase lags ($F = 6.7, 4.1, 9.4$, respectively; $p < 0.05$). The multiple comparison t-tests with a Bonferroni correction showed that the following swimming modes had significantly different phase lags: hovering and fast forward swimming for P5-P4, hovering and upside down swimming for P2-P1, and hovering and fast forward swimming for P1-P5 ($p < 0.017$). No significant phase lags differences were found between fast forward swimming and upside down swimming.

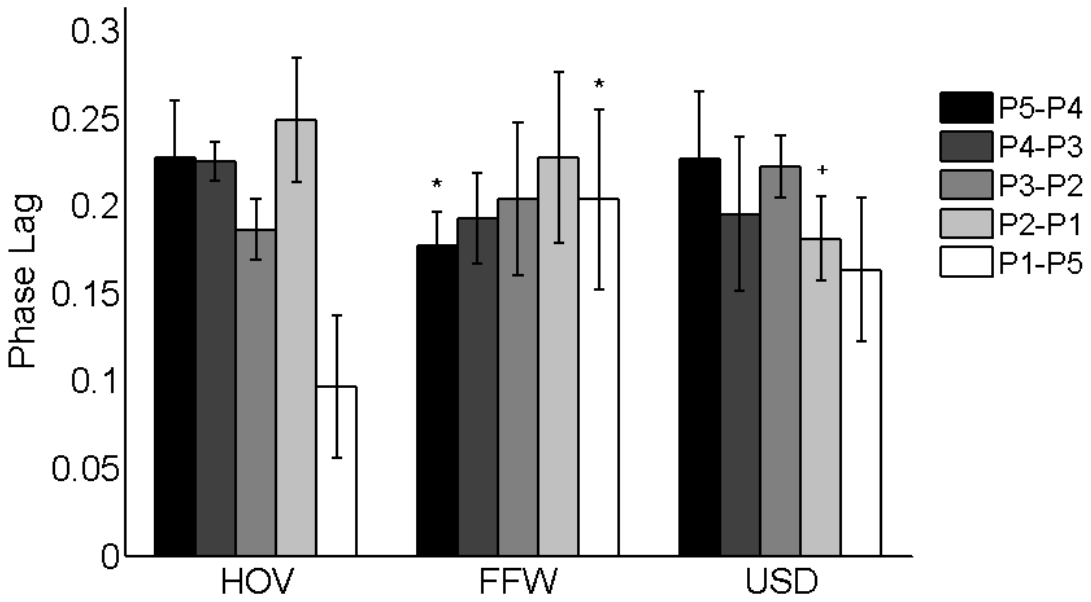

Figure 3.7 Phase lag between consecutive pleopod strokes (reported as fraction of a complete cycle) for hovering (HOV), fast forward swimming (FFW), and upside down swimming (USD). Error bars indicate standard deviation. * indicates a significant statistical difference between data for HOV and FFW and + indicates a significant statistical difference between data for HOV and USD. No significant differences were observed when comparing the data for FFW and USD

3.3.4. Induced Fluid Velocity

Flow visualization shows that pleopod action during hovering results in a posteriorly-directed jet-like flow angled ventrally. The body angle of the hovering animal in the water (in the range of 25-50°) ensures that the resulting jet is pointed down. Flow visualization was used to estimate the flow speed in 10 instances by measuring the displacement of a particle or flow feature over a specified time delay. Table 3.2 reports, for hovering krill ranging in size from 3.2 to 3.8 cm, that the jet speed in the wake v_w at a distance less than one body length away from the animal was 4.5 ± 1.2 cm s^{-1}, N=10

(mean ± s.d.). Catton et al. (2011) measured flow fields for free-swimming *E. pacifica* and *E. superba*. The maximum flow velocities, animal sizes, beat frequencies, and swimming speeds of these animals are also reported in Table 3.2. According to the behavioral swimming modes identified in this study, *E. pacifica* in Catton et al. (2011) were in the transitional swimming mode (0.9 body lengths per second) and the *E. superba* straddled the transitional and fast forward swimming modes (approximately 0.9–2.2 body lengths per second). For free-swimming *E. superba*, maximum flow velocities then range from 4.5 cm s^{-1} for hovering to 6.2 cm s^{-1} for fast forward swimming at 2.2 body lengths per second. Since *E. superba* may swim up to 7 body lengths per second, actual maximum flow velocities may range much larger. Previous flow measurements reported for tethered animals are likely characteristic of maximum flow velocities for fast forward swimming animals rather than for hovering animals. This discrepancy probably exists because tethered animals are trying to escape by beating their pleopods at a higher frequency, and the greater beat frequency will cause a greater induced flow. For instance, Alben et al. (2010) found that tethered and fast forward swimming *E. pacifica* beat their pleopods with the same beat frequency (approximately 10.5 Hz) while the free-swimming *E. pacifica* (in the transitional swimming mode) in Catton et al. (2011) beat their pleopods with a much lower frequency. This difference in beat frequency probably translates into a difference in induced flow velocity. For example, Catton et al. (2011) measured induced flows of 3.4 cm s^{-1} for free-swimming *E. pacifica* in the transitional swimming mode. In contrast, Yen et al. (2003) found larger maximum velocities of 4.86 cm s^{-1} for a 2 cm tethered *E. pacifica*. Tethering and presumed higher beat frequency are likely the reasons that this smaller animal was able to produce a greater maximum flow

velocity in comparison with the larger *E. superba* in the current study. As summarized in Table 3.2, this comparison illustrates the importance of both recognizing the effect of tethering and of comparing similar swimming modes when examining the flow fields of animals using a metachronal propulsion system.

Table 3.2 Values of fluid velocity in the wake (v_w), body length (BL), beat frequency (n), and swimming speed (V) for three euphausiid species. Body length in Catton et al. (2011) was measured from the furthest extent of the antennae to the tail but was measured from eyeball tip to tail in this study

Species	v_w (cm s^{-1})	BL (cm)	n (Hz)	V (cm s^{-1})	Swimming Mode	Source
E. superba	4.5 ± 1.2	3.2 – 3.8	3.0 ± 0.2	1.0 ± 0.6	HOV	Current study
E. superba	6.2 ± 1.3	5.1 ± 0.5	3.0 ± 0.2	7.7 ± 3.3	Transitional, FFW	Catton et al. (2011)
E. pacifica	3.4 ± 1.1	2.7 ± 0.2	5.6 ± 0.7	2.5 ± 0.5	Transitional	Catton et al. (2011)
E. pacifica	4.86	2	-	Tethered	-	Yen et al. (2003)
E. pacifica	-	3.2	10.9	15.5	FFW	Alben et al. (2010)
E. pacifica	-	3.2	10.4	Tethered	-	Alben et al. (2010)
M. norvegica	6	4	7.3	Tethered	-	Kils (1981)

3.4. Discussion

3.4.1. Metachronal System Design

In this study, we examine both the design and operation of the metachronal locomotion system. The Antarctic krill *E. superba* has served as our model species to examine the operation and especially the adaptability of this propulsion system. Understanding the metachronal system operation in Antarctic krill, however, requires an understanding of the fundamental design elements which comprise the system. It is also helpful to consider the position of the Antarctic krill in the metachronal design space relative to that occupied by other crustacean species. The success of the metachronal propulsion system is predicated on three known design elements: 1) the appendage morphology, 2) the coordinated movement of the appendages through the water (i.e. the stroke kinematics), and 3) the hydrodynamic result of the stroking appendages. Each of these three interlocking design elements will be examined in more detail. A fourth design element, i.e. the spacing between appendages, is identified in this study and will be presented after discussions of the metachronal system design and operation.

Appendage morphology: Metachronal swimming in crustaceans is a drag-based mechanism in which the swimming appendages serve as paddles. In order to generate forward propulsion, the drag of the appendage during the power stroke must be larger than that during the recovery stroke. One way to achieve this asymmetry is by varying the surface area of the appendage during the stroke cycle. Species using the metachronal propulsion system have developed three methods of increasing their appendage profile on the power stroke and decreasing it during the recovery stroke. First, rowing appendages

are often designed, either with an articulation or with asymmetric bending rigidity, such that they flex posteriorly but not anteriorly (Hessler 1985; Johnson and Tarling 2008). During the recovery stroke, the limb therefore flexes, decreasing form drag. Second, the distal portion of the rowing limb is often biramous. The two appendage segments are actively spread laterally during the power stroke to increase drag and folded together during the recovery stroke to decrease drag. Species employing this strategy range across the crustaceans and include the Antarctic krill *Euphausia superba* (Kils 1981), remipedes (Kohlhage and Yager 1994), the tube-dwelling shrimp *Callianasa subterranea* (Stamhuis and Videler 1998a), and the calanoid copepod *Calanus finmarchicus* (Lenz et al. 2004). Third, the distal appendage segments of most swimming crustaceans bear a fringe of setae. These setae, which may be asymmetrically hinged (Wootton 1999), increase the surface area of the paddle during the power stroke and passively fold together during recovery. Because viscous forces are predominant at the velocity and length scales at which crustacean appendages operate (i.e. small Reynolds number), these setae act as leaky paddles (Cheer and Koehl 1987).

Stroke kinematics: In a presumed attempt to avoid appendage interference or to increase swimming efficiency, organisms that use an adlocomotory metachronal rhythm show a wide variety of stroke kinematics. Differences may be seen in stroke plane and left-right symmetry as well as in kinematic parameters such as stroke amplitude, beat frequency, and phase lag.

Stroke plane: Krill (Kils 1981), lobsters (Lim and DeMont 2009), amphipods (Boudrias 2002), shrimp (Cowles 1994; Stamhius and Videler 1998a), and isopods (Alexander 1988) beat their swimming appendages in a sagittal plane (due to their ventral

placement). Conversely, the leg segments of remipedes are directed laterally and thus beat in a horizontal plane (Kohlhage and Yager 1994). Mysids, which rely on eight pairs of laterally-directed thoracic exopodites for locomotion, beat their appendages in an elliptical pathway. In order to minimize congestion, each exopodite traces a different ellipse. The major axes of these ellipses are rostro-caudal (Laverack et al. 1977; Schabes and Hamner 1992).

Symmetry: Contralateral synchrony, in which the left and right swimming appendages beat together, is observed in many species using adlocomotory metachronal propulsion. This is the case for krill (Kils 1981), adult lobster pleopods (Davis 1968), amphipods (Boudrias 2002), shrimp (Cowles 1994; Stamhius and Videler 1998a), and isopods (Alexander 1988). In mysids and pycnogonids, there is an antiphase relationship between contralateral appendages (Morgan 1972; Laverack et al. 1977; Schabes and Hamner 1992). Less coordination is seen between the contralateral exopodites of the lobster *Homarus gammarus* in its larval form. In this species the phase relationship between the left and right sides undergoes a constant progression, a phenomenon known as gliding coordination (Macmillan et al. 1976).

Kinematic Parameters: Kinematic parameters such as beat amplitude, frequency, and phase lag between ipsilateral appendages have been previously recorded for many species. Great variation is seen among species. Beat amplitudes of up to 131° have been recorded for freely swimming isopods (Alexander 1988), whereas amplitudes as small as 34° have been reported for slowly swimming *E. superba* (Kils 1981). Beat frequency, which is known to scale with animal size (Alexander 2003), varies over two orders of magnitude for metachronal swimmers. For small metachronal swimmers such as the

calanoid copepod *Temora longicornis* during an escape, the beat frequency can reach 117 Hz (van Duren and Videler 2003). For jet-assisted walking in the much larger American lobster (*Homarus americanus*), pleopod beat frequencies as small as 1.3 Hz have been recorded (Lim and Demont 2009). Beat pattern also varies greatly. For instance, some species such as isopods, copepods, and stomatopods incorporate a pause after the power stroke in order to perform a recovery stroke with all legs simultaneously (Alexander 1988; Lenz et al. 2004; Campos 2009; Kiørboe et al. 2010), whereas other species such as Pacific krill *Euphausia pacifica* beat with almost perfect metachrony (Alben et al. 2010).

Hydrodynamics: The hydrodynamic result of a metachronal stroke has been investigated qualitatively in mysids (Schabes and Hamner 1992) and northern krill *Meganychtiphanes norvegica* (Kils 1981; Patria and Wiese 2004) and quantitatively in Pacific krill *E. pacifica* (Yen et al. 2003; Goldthwait et al. 2004; Catton et al. 2011), Antarctic krill *E. superba* (Catton et al. 2011), calanoid copepods (Yen and Strickler 1996; van Duren and Videler 2003; Catton et al. 2007; Jiang and Kiørboe 2011), tube-dwelling shrimp (Stamhuis and Videler 1998b), and lobsters (Lim and DeMont 2009). In each of these species, a narrow, ventroposteriorly directed jet is generated, the direction of which may be controlled by flexion of the tail (Yen et al. 2003; Kils 1981). The jet velocity may pulse close to the animal body but becomes steadier further downstream (Lim and DeMont 2009). The effect of the jet is to propel the animal forward at a Reynolds number in the range from 2 (for a swimming copepod) to 10,000 (for a cruising krill) (Kils 1981; Yen and Strickler 1996). These values place the metachronal propulsion system in the unusual transition zone in which both viscous and inertial effects are important (Walker 2002; Sensenig et al. 2009).

3.4.2 Swimming Modes

The adaptability of the metachronal locomotion system to various needs (i.e. hydrodynamic, energetic, or behavioral) is expressed through the swimming modes. The three swimming modes identified here, hovering, fast forward swimming, and upside down swimming, are illustrative because they likely represent *extrema* in the metachronal design space defined by swimming speed and body angle.

In hovering, the pleopods beat with small amplitude (50-74°) and low beat frequency (3 Hz). Fast forward swimming is characterized by large stroke amplitude (73-106°) and high beat frequency (5.9 Hz) and thus will be more energetically expensive than hovering. Figure 3.5 shows that larger amplitudes are obtained not by drawing the pleopods further in towards the body during the recovery stroke (smaller minimum α) but rather by dramatically increasing the excursion of the pleopod (larger maximum α). The result of this further excursion is to impart more backward momentum to the surrounding fluid and hence generate greater thrust force. From a hydrodynamic perspective, weight support ceases to be the primary purpose of the propulsion jet produced by the pleopods. Kils (1981) showed that dynamic lift forces capable of supporting the animal's entire underwater weight developed at body speeds of approximately 7 cm s^{-1}. Therefore, the effect of the beating pleopods at larger speeds is to provide thrust that overcomes the animal's profile drag. For a horizontally-swimming animal, this jet therefore will be directed posteriorly but still angled slightly downward, as shown by Catton et al. (2011) for *E. superba* and by Yen et al. (2003) for tethered *E. pacifica*. Streamlining of the body form becomes important at these larger speeds. Figure 3.5 shows that the minimum value of β is smaller for fast forward swimming than it is for hovering. A smaller minimum β

means that the endopodite and exopodite are held more closely to the body during the recovery stroke. It is not known whether this is a passive effect resulting from the greater angular velocities in fast forward swimming or an active attempt to reduce drag.

In upside down swimming, the stroke amplitudes were again large (71-98°), but the beat frequency was lower than in fast forward swimming (3.7 Hz). Of particular interest for this swimming mode is how the animal maintains its vertical position. In this mode, the body is angled such that the beating appendages produce a jet that is pointed horizontally and only slightly downward. Furthermore, as seen in Figure 3.3C, the telson is held horizontally, preventing flow in the downward direction. How, then, does the krill impart enough downward momentum to prevent sinking? While it is likely that dynamic lift contributes the most vertical force, the minimum values of β for all pleopods in upside down swimming are much smaller than in either hovering or fast forward swimming (Figure 3.5). Small values of β at the body angle used in upside down swimming indicate that the exopodites are possibly imparting fluid momentum downward around the sides of the body. If this conjecture is correct, then the phenomenon highlights the importance of the lateral extension of the exopodites well beyond the edges of the body during the power stroke. While no flow visualization was captured for upside down swimming in the current study, two flow visualization instances captured during hovering show an unusually powerful fifth pleopod stroke that demonstrates horizontal ejection of fluid past the tail. A similar fluid ejection during upside down swimming would be consistent with the idea of imparting fluid momentum downward given the body angle during that swimming mode. Furthermore, during the recovery stroke, the jet produced by the exopodites is not obstructed by the recovering pleopods, thereby reducing drag and

increasing thrust. Lim and DeMont (2009) and Stamhuis and Videler (1998b) used particle image velocimetry (PIV) to show a similar phenomenon in the metachronal beat of pleopods in lobster and tube-dwelling mud shrimp, respectively.

Since animals were mostly filmed from a lateral position, it is not known whether there is any variation in the internal angle γ (between the endopodite and exopodite) among these three swimming modes. Active control over the extension of the exopodite could provide an additional way to modulate thrust production. It is not yet known how swimming krill are able to turn, but the ability to asymmetrically extend contralateral exopodites and therefore asymmetrically generate thrust could also provide maneuvering capability.

3.4.3. Method of Increasing Speed

It has been shown that pleopod beat frequency and stroke amplitude vary significantly among swimming modes. Hovering animals beat with a low frequency and amplitude, whereas fast forward swimming animals beat with a high frequency and amplitude, but how do these factors (beat frequency and amplitude) vary with animal speed? Kils (1981) described the relationship between stroke kinematics and speed for adult animals in the 40-55 mm length range and showed that a two-stage relationship existed. Animals swimming up to 15 cm s^{-1} increased their speed by modifying their stroke execution (i.e. stroke amplitude). Once this speed was reached, the stroke was "optimally executed." To attain greater speeds, the beat frequency then was increased. Figure 3.8 shows the relationship found in the current study between displacement per beat (body lengths per beat, a measure of stroke efficiency) versus normalized speed (body lengths per second).

Kils' (1981) data (normalized by an animal length of 47.5 mm, the midpoint of his reported range) are shown for comparison, and a good match with the current data is achieved. The linear increase of the curve for normalized speeds less than 3 BL s^{-1} is due to increased stroke efficiency. The increase in stroke efficiency is due to greater stroke amplitude. Figure 3.9 shows the mean stroke amplitude of the first, third, and fifth pleopod pairs of each swimming animal. The second and fourth pleopod pairs are omitted for the sake of clarity. Pleopod stroke amplitude increases with normalized speed for speeds less than 2 BL s^{-1}. For larger values of normalized speed, the stroke amplitude remains approximately constant, even as the body speed increases up to 7 BL s^{-1}. For normalized speed values greater than 2 BL s^{-1}, further increases in speed are achieved entirely through increased beat frequency. This point is illustrated in Figure 3.10, which shows beat frequency as a function of normalized speed. At speeds less than 2 BL s^{-1}, the beat frequency is essentially constant. At greater normalized speeds, the beat frequency increases linearly with normalized animal speed.

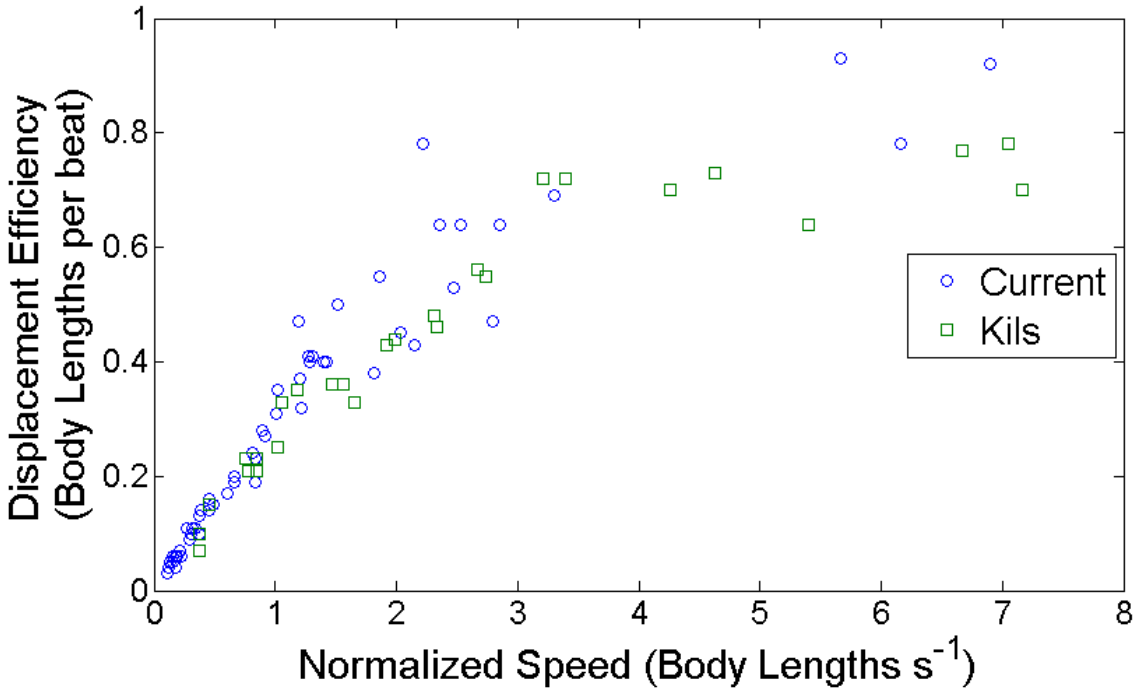

Figure 3.8 The relationship between stroke efficiency (as measured by displacement per beat) and normalized animal swimming speed (body lengths second^{-1}). Data shown from current study and from Kils (1981)

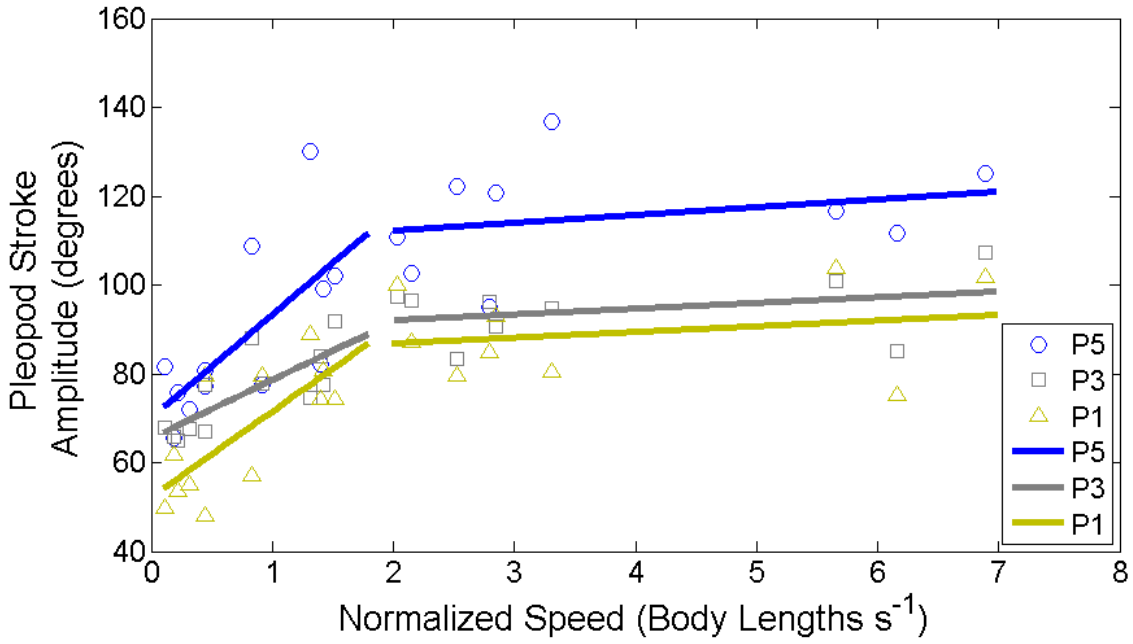

Figure 3.9 The relationship between pleopod angle amplitude and normalized animal swimming speed

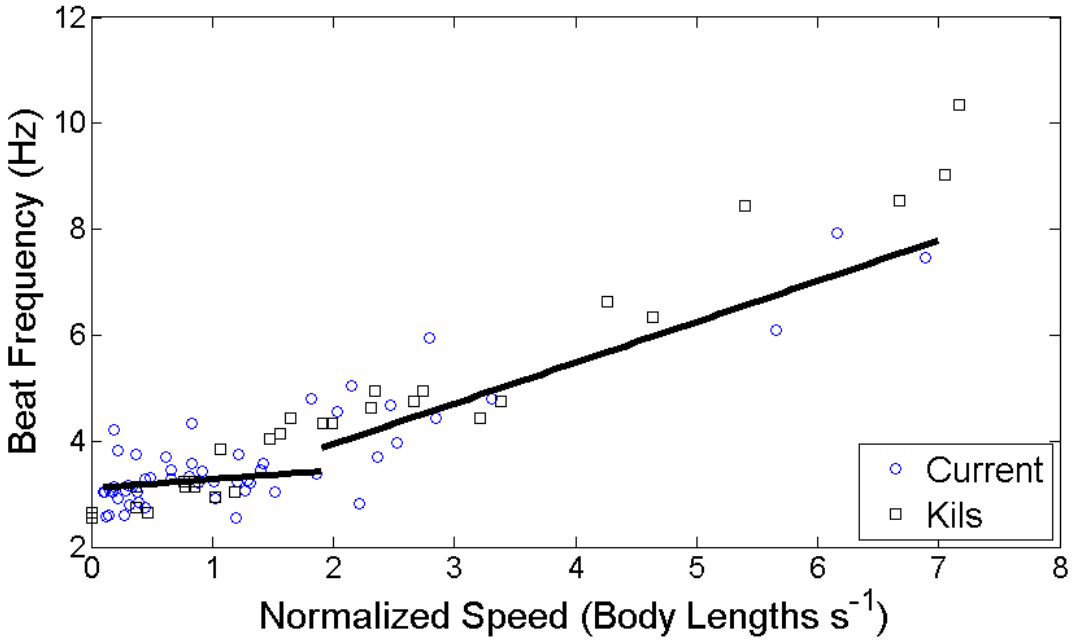

Figure 3.10 The relationship between beat frequency and animal swimming speed. Data shown from current study and from Kils (1981)

3.4.4. Inter-stroke Phase Lag

The phase lag between consecutive strokes (i.e. the inter-stroke phase lag between P5 and P1) also was shown to vary significantly between hovering and fast forward swimming. In order to examine the relationship between this parameter and normalized animal speed, the inter-stroke phase lags were analyzed in all hovering and fast forward swimming video sequences. The P1 and P5 stroke initiation time points for two consecutive strokes were recorded and used to calculate an average P1-P5 phase lag for each video sequence (mean value reported in Figure 3.7). Figure 3.11 shows the P1-P5 phase lag as a function of normalized animal speed. The relationship again seems to be two-stage, with inter-stroke phase lags increasing with normalized speed until

approximately 2 BL s^{-1} and then remaining constant at larger normalized speeds. The 'early' initiation of the P5 power stroke during hovering means that consecutive stroke sequences overlap. More downward momentum therefore is imparted during a given time period (i.e. a stroke) than would be if strict metachrony were observed. For instance, if strict metachrony were observed, then five pleopod pairs would contribute downward momentum in a given stroke period. With early initiation of the P5 stroke (i.e. inter-stroke phase lag of nearly zero), however, six pleopod pairs contribute downward momentum in that same time period since the fifth pleopod pair will stroke twice (once at the stroke beginning and again in near-synchrony with P1). Elimination of the phase lag between P1 and P5 thus translates into a higher effective beat frequency, the effect of which is to increase thrust force without increasing beat amplitude. The synchrony also may indicate the minimum distance between pleopods needed to prevent fluid interference between pleopods.

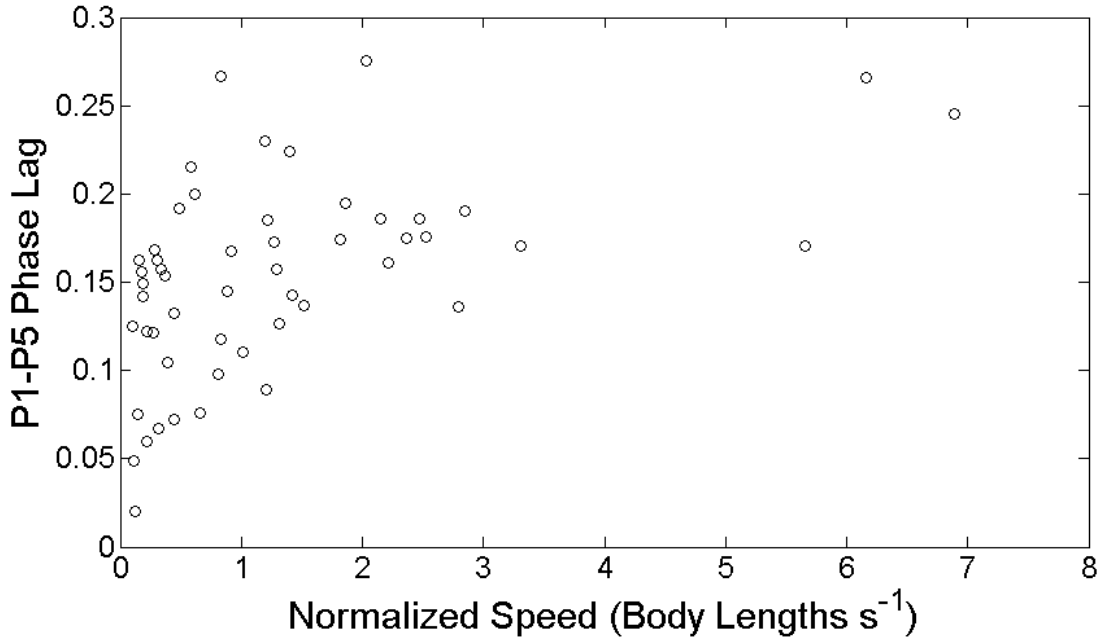

Figure 3.11 The relationship between normalized body speed and interstroke (P1-P5) phase lag

3.4.5. Design Aspects of Metachrony

The detailed pleopod kinematics data provided herein give insight into the advantages, design, and operation of the widely-used metachronal propulsion system. Even without accounting for unsteady hydrodynamic interactions between pleopods that may provide extra thrust (Lim and DeMont 2009), Alben et al. (2010) found that the metachronal stroke rhythm was advantageous over more synchronous stroke rhythms in producing larger average propulsion velocity. The advantage of multiple appendages operating with a metachronal rhythm can be encapsulated in the concept of the advance ratio (Ellington 1984). The advance ratio *J* is the forward speed of the animal standardized by the mean velocity of the tip of the appendage:

$$J = \frac{V}{2\theta nL}$$

where V is the animal speed, θ is the stroke amplitude in radians, n is the beat frequency, and L is the appendage length. Typical values of J for rowing animals with a single pair of appendages range from 0.1 to 0.6, but Walker (2002) noted that remipedes have a $J >$ 1. Similarly, substituting typical values of these parameters for a fast forward swimming *E. superba* (pleopod length of L = 0.65 cm) gives values of J from 1.1 to 1.5. For *E. pacifica* (pleopod length of L = 0.25 cm), typical values of J range up to 1.7. These values indicate that the animal speed is greater than its appendage speed, a counterintuitive situation for drag-based locomotion. Normalizing the advance ratio by m, the number of pairs of legs for metachronal locomotion, J_m, gives values that may be compared to the original advance ratio for animals with a single pair of rowing appendages:

$$J_m = \frac{V}{2\theta nmL}$$

J_m then ranges from 0.2 to 0.3 for euphausiid locomotion, which is comparable to J for single-appendage rowing systems. The advantage of a multi-appendage metachronal rowing system over a single appendage rowing system (both operating with the same appendage tip speed) is that the metachronal system will reach greater body speeds ($J >$ 1). Conversely, assuming a given body speed between these two types of rowing animals, the animal with a multi-appendage metachronal system will have to produce a much lower appendage tip speed. This lower tip speed may be accomplished by stroking at a lower frequency, decreasing the stroke amplitude, or having a shorter appendage.

Essentially, metachronism allows animals with multiple appendages to operate those appendages at a smaller Reynolds number while still maintaining the capability of achieving large body speeds. Operating swimming appendages in a more viscous regime is crucial to generating thrust as a "paddle" considering the plumose nature of these appendages (Cheer and Koehl 1987) and might be important in protecting the fragile bristle structures from potentially damaging inertial forces.

E. superba illustrates the way in which many metachronally-propelled crustaceans exhibit adaptations characteristic of organisms influenced by both inertial and viscous forces. Based on a characteristic body length of 5 cm and a fast forward swimming speed of 40 cm s^{-1}, an *E. superba* operates at a fairly high Reynolds number on the order of 10,000. At this Reynolds number, form drag is an important consideration, and Kils (1981) found that krill body forms are highly streamlined. Using empirical relationships reported by Kils (1981), the drag coefficient of the characteristic fast forward swimming krill is approximately 0.26. In comparison with the krill body, the typical pleopod operates at a Reynolds number that is two orders of magnitude smaller. The effective width of an exopodite (approximately 2 mm including setae) can be used as a characteristic length scale. Using a typical pleopod length of 6.5 mm, a beat magnitude of 110 degrees, and a beat frequency of 8 Hz to obtain a characteristic velocity, the Reynolds number of a pleopod is on the order of magnitude of 100. A large pleopod drag coefficient is advantageous during the power stroke and was estimated by Alben et al. (2010) to be similar to that of a plate transverse to the flow (approximately 2). Since metachrony essentially enables the appendages to operate at lower Reynolds numbers,

metachrony itself could be considered characteristic of the transitional Reynolds number realm where both viscous and inertial effects are important.

The success of the metachronal system depends on how the appendage morphology, stroke kinematics, and resulting hydrodynamics interact to produce locomotion. One important aspect of the appendage morphology that has not been previously recognized is the spacing between appendages, particularly with respect to the appendage length. The ratio of the length between adjacent appendages B to the appendage length L will affect the range of possible kinematics available to the metachronal system as a whole, assuming that the appendages operate in a single stroke plane. For instance, if $B/L > 2$, the spacing between the appendages is twice the appendage length, and each appendage may operate independently without the possibility of interference. However, this arrangement is not seen in nature, possibly indicating that the hydrodynamic benefits of metachrony outweigh the added complexity necessary to coordinate many appendages. Table 3.3 shows typical values of B/L for a range of aquatic species using a metachronal stroke, including the comb jelly which metachronally strokes its ctenes to accomplish locomotion (Sleigh and Barlow 1980; Vannier et al. 1997; Ivanenko et al. 2007; Alben et al. 2010; Anker 2010). The value of this ratio for all species examined fall within $0.2 < B/L < 0.65$, and most lie in a smaller range. The paucity of values outside this range can perhaps provide insight into the metachronal system design.

Table 3.3 Values of the ratio *B/L* for a variety of species, where B is the distance between adjacent appendages and L is the appendage length

Species	B / L
Antarctic krill (*Euphausia superba*)	**0.45**
Pacific krill (*Euphausia pacifica*)	**0.65**
Northern krill (*Meganyctiphanes norvegica*)	**0.48**
Other euphausiids (3 species)	**0.42 – 0.52**
Remipedes (7 species)	**0.3 – 0.53**
Lobster (*Homarus americanus*)	**0.44**
Stomatopods (4 species)	**0.36 – 0.6**
Amphipods (3 species)	**0.38 – 0.45**
Penaeid shrimp (3 species)	**0.37 – 0.51**
Alpheid shrimp (2 species)	**0.44**
Brine shrimp (*Artemia salina*)	**0.25 – 0.30**
Ghost shrimp (*Callianassidae*)	**0.40**
Nebalia bipes	**0.21**
Idoteid isopod (*Idotea resecata*)	**0.21**
Calanoid copepod (*Calanus finmarchicus*)	**0.25**
Calanoid copepod (*Methocalanus gabonicus*)	**0.28**
Comb jelly (*Pleurobrachia pileus*)	**0.56**

Small values of *B*/*L* could be achieved by either small spacing between adjacent appendages (small *B*) or by long appendages (large *L*). A 'large *L*' design is likely disadvantageous, however, because it requires greater limb rigidity and musculature to compensate for the larger hydrodynamic loads experienced by the longer limb moving through the water. A 'small *B*' design with closely spaced limbs, on the other hand, decreases the range of limb motion. For instance, anterior limbs near the end of the power stroke could prevent posterior limbs from recovering, necessitating a change in stroke kinematics. In Table 3.3, for example, the three species with the smallest *B/L* values are the leptostracan *Nebalia bipes*, the isopod *Idotea resecata*, and the copepod *Calanus finmarchicus*. All three of these species exhibit a simultaneous recovery stroke, a pattern likely due to the small *B/L* ratio (Vannier et al. 1997; Alexander 1988; Lenz et al. 2004). Species with larger *B/L* values exhibit a more metachronal recovery stroke.

Alternatively, large values of *B*/*L* could be achieved either by large limb spacing (large *B*) or by short appendages (small *L*). The disadvantage of a 'small *L*' design is that short appendages yield small amounts of forward thrust. A 'large *B*' design, on the other hand, requires more space on the animal and may isolate each limb hydrodynamically. The hydrodynamic interaction between adjacent limbs is not fully understood but could possibly provide extra thrust. For instance, Lim and Demont (2009) found inter-pleopod jets that formed when pleopods squeezed together late in the power stroke in their lobster model.

Even in animals with less extreme *B*/*L* ratios such as krill, the appendage kinematics are linked with the spacing and length of the appendages. The anteriorly-decreasing magnitude of the pleopod stroke amplitude seen in Figure 3.6 is a reflection of the close

spacing of the five pleopod pairs. P5 is able to stroke with the largest amplitude because it is the most posterior and therefore unimpeded. The stroke amplitude for P4 is smaller because it is impeded by the recovering P5. The more anterior pleopods experience the same phenomenon and stroke with even smaller amplitudes. A further adaptation to accommodate the close spacing of appendages is to vary the appendage length. Table 3.4 shows mean appendage lengths for the *E. superba* in this study. In krill, remipedes, and *Artemia* the anterior and posterior appendages are shorter than the medial appendages (Sleigh and Barlow 1980; Kohlhage and Yager 1994). Shorter posterior appendages are advantageous because they allow those limbs to recover with less interference from the more anterior limbs. An increased number of articulations in the appendage (as seen in the remipede) or increased appendage flexibility also could help minimize congestion during the recovery stroke by keeping the limb tip close to the body. A parametric study with a dynamically-scaled physical model using appendage kinematics similar to those found in this study could ideally elucidate the role that each of these factors play in promoting the success of the metachronal propulsion system.

Table 3.4 Mean protopodite and endopodite lengths for adult krill (BL > 2 cm; N=16) in this study

	P5 (cm)	**P4 (cm)**	**P3 (cm)**	**P2 (cm)**	**P1 (cm)**
Protopodite	**0.20**	**0.25**	**0.28**	**0.31**	**0.32**
Endopodite	**0.37**	**0.40**	**0.43**	**0.41**	**0.35**
Total	**0.57**	**0.65**	**0.71**	**0.71**	**0.67**

CHAPTER 4

A HIGH SPEED TOMOGRAPHIC PIV SYSTEM FOR MEASURING ZOOPLANKTONIC FLOW

Quantification of the hydrodynamic disturbance of free-swimming zooplankton provides insight into propulsion as well as organism sensory interactions. Current flow measurement techniques, such as planar particle image velocimetry (PIV), are limited by their two dimensional nature. These techniques also are challenged by the small spatial scale of zooplankton, by the high speeds achieved by many zooplankton species, and by zooplankton photosensitivity to a broad range of wavelengths. We present a high speed tomographic PIV system using near-infrared laser illumination that is capable of measuring three-dimensional velocity vectors in a volume surrounding a plankter. This technique is assessed by recording and analyzing the time-resolved flow field created by a high-speed escape of a copepod (*Calanus finmarchicus*). Persistent body and wake vortices are created by the impulsive momentum transfer to the fluid surrounding the animal. It is shown that some aspects of this flow can be analytically modeled as an impulsive stresslet. Azimuthal asymmetry of the strength and position of the wake vortex is analyzed and attributed to the strong ventral flows created by the metachronally beating swimming legs. In addition, the energy required by a copepod escape jump is estimated by calculating the viscous energy dissipation rate using the spatial gradients of the measured three dimensional velocity field. Finally, the challenges and benefits of the tomographic PIV technique are discussed.

4.1. Introduction

4.1.1 Zooplanktonic Flow

Quantification of the flow produced by zooplankton as they swim and feed yields insight into locomotion techniques, social aggregations, feeding strategies, and energetics. For instance, various feeding strategies employed by zooplankton have been illuminated by considering the fluid mechanics involved. Fields and Yen (1993) mapped the three-dimensional feeding current of a filter-feeding calanoid copepod (*Pleuromamma xiphias*) to quantify the volumetric extent of its signature that might be visible to prey or predators. Fields and Yen (1997) also showed how vorticity in the feeding current of the copepod *Euchaeta rimana* orients the entrained prey such that an escape attempt will transmit positional information to the predator's antennal sensory array. Similarly, Malkiel et al. (2003) showed, using three-dimensional velocity measurements, that filter-feeding copepods must occasionally jump in order to avoid re-sampling the same fluid volume. Kiørboe et al. (2009) investigated ambush-feeding copepods such as *Acartia tonsa* and *Oithona davisae* and showed, using fluid simulations, how these predators can rapidly accelerate towards their prey without developing a significant flow disturbance that would push the prey away. Kiørboe et al. (2010a) also demonstrated with flow measurements how ambush feeding, as opposed to filter- or cruise-feeding, generates a smaller time-averaged flow signal (and thus a lower predation risk) for copepods smaller than 1 mm, whereas the opposite is true for larger copepods. Further, quantification of zooplankton-generated flow fields can provide energetic estimates of the cost of propulsion or feeding through the viscous dissipation of kinetic energy, a calculation that involves the spatial gradients of the velocity field (Catton et al. 2007). For example, van

Duren and Videler (2003) showed that the rate of energy dissipation in tethered *Temora longicornis* was two orders of magnitude higher for escape responses than for feeding. These examples indicate that key aspects of zooplankton behavior and interactions can be understood only by quantifying the flows that they produce and to which they respond.

Various particle image velocimetry (PIV) techniques have been used to quantify flow fields associated with free-swimming zooplankton behavior (e.g., Stamhuis et al. 2002). Planar PIV has been used to measure the flow fields associated with copepod swimming and jumping (Catton et al. 2007, 2012; Kiørboe et al. 2010a). Digital holographic PIV has been used to measure feeding flow in a three-dimensional volume (Malkiel et al. 2003). While these previous studies were successful to some extent, quantifying the flow surrounding zooplankton presents the following four unique challenges: 1) Zooplankton behavior and flow disturbances are intrinsically three-dimensional, and capturing certain behaviors (such as a high-speed escape) within a laser light sheet is rare. 2D and stereo PIV are therefore highly restrictive for this purpose since they are inherently confined to quantifying the velocity field in a single illumination plane. 2) Zooplankton are small (0.1 to 5 mm) and respond to small strain rates (0.025 s^{-1}). Hence, resolution of corresponding velocity gradients requires medium to high particle seeding and dense fields of velocity vectors. 3) Zooplankton swim quickly and generate highly unsteady flows, with copepod escape speeds reaching 1 m s^{-1} (500 body lengths per second) (Yen 2000). High temporal resolution is therefore required to resolve these events. 4) Zooplankton are phototactic to a broad range of wavelengths in the visual band. Use of intense laser illumination in this range induces a response that interferes with behavioral assays. Taken together, these

four challenges necessitate a new approach to quantifying the flow fields surrounding zooplankton.

4.1.2. Extensions to Planar PIV

Several approaches to extending the planar PIV technique to 3D have been developed during the past few years (Arroyo and Hinsch 2008). These include holographic PIV, scanning illumination approaches, defocusing PIV, and tomographic PIV. The advantages, disadvantages, and limitations of these approaches are briefly discussed. Holographic PIV has been developed by several researchers and offers the greatest spatial resolution (e.g., Hinsch 2002, Pu and Meng 2005, Katz and Sheng 2010, Orlov et al. 2010). The technique consists of recording a hologram of the light scattered off suspended particles in the flow to determine the 3D position of particles during post-processing (i.e., reconstruction) of the hologram. Subsequent cross-correlation or particle tracking analysis yields the 3D velocity vector field in the holographic volume. The disadvantages of the holographic PIV approach include processing of the emulsion plate in the dark room, tedious extraction of the particle positions during hologram interrogation, and lack of temporal repetition. Commercial holographic PIV systems are not available largely because of these disadvantages along with the advanced technical intricacy of the optical systems (Meng et al. 2004). In the past few years, the use of digital recording medium, such as CCD cameras, has been suggested as a method to overcome these disadvantages (Meng et al. 2004, Orlov et al. 2010). For instance, Malkiel et al. (2003) employed a 2K×2K digital camera, which effectively records orders

of magnitude less information than silver halide holographic film. The camera resolution necessitated low particle density, which resulted in modest velocity vector density and fairly high uncertainty for the velocity measurements. Holographic PIV has great promise and continues to be developed, but it currently lacks the robust operation with high spatial and temporal resolution that the application of flow around zooplankton requires.

One technique to overcome the particle density limitation is to illuminate and image individual planes. Brücker (1997), Liberzon et al. (2004), Hoyer et al. (2005), and Cheng et al. (2011) each used a variation of the basic approach of illuminating parallel planes with a light sheet and recording the particle locations in each plane. The seeding density often can be similar to that for traditional 2D and stereo PIV. One disadvantage of this approach is that the planes often are illuminated sequentially; hence the image acquisition is not simultaneous for parallel planes. Alternatively, Liberzon et al. (2004) illuminated three planes simultaneously, which limits the seeding density and requires sophisticated post-processing to separate the imaged planes. Another disadvantage of the parallel plane illumination technique is that it results in discrete separation of the measurement planes.

Another approach is to record the particle positions with three or more cameras during volume illumination of the flow. Willert and Gharib (1992), Pereira et al. (2000), and Kajitani and Dabiri (2005) describe a defocusing approach that employs offset apertures for three digital sensors to yield defocused images of the particles. The aperture geometry combined with the information from the three sensors yields the particle position relative to the focus plane. A potential advantage is that once the aperture arrangement is set, the system is effectively calibrated. However, commercially available

systems that follow this approach are relatively inflexible in terms of size and resolution of the measurement volume.

In tomographic PIV, the three-dimensional light intensity field of illuminated tracer particles in the flow is reconstructed from multiple cameras viewing the interrogation volume from different angles. The 3D volume of light scattered from the particle distribution is typically reconstructed via a multiplicative algebraic reconstruction technique (MART) algorithm. Velocity vectors are computed via an iterative three-dimensional cross-correlation technique between consecutive reconstructed light intensity volumes using deformed interrogation volumes (Elsinga et al. 2006, 2008). The method has been advanced in recent years with the development of robust and efficient reconstruction procedures (Atkinson and Soria 2009, Novara et al. 2010), volumetric self-calibration techniques (Wieneke 2008), and identification techniques for ghost particles (Elsinga et al. 2011). Tomographic PIV has the advantage of a simple optical arrangement while allowing medium seeding density. Tomographic PIV also allows for flexible selection of camera specifications and illumination type. The method is also attractive because it builds on the success of stereo PIV techniques with a simple modification to the illumination optics and more sophisticated post-processing software.

In this paper, we describe the development of a high-speed tomographic PIV system that addresses the four challenges described above for flow measurements surrounding zooplankton. Further, we present an example application of an escaping copepod that highlights the system's ability to capture the ephemeral, three-dimensional flows produced by zooplankton.

4.2. Materials and Procedures

The tomographic PIV system developed to characterize zooplankton flow features four Phantom v210 cameras (Vision Research, Wayne, NJ) capable of filming at up to 2190 frames per second. This frame rate is sufficient to resolve unsteady flow generated by a copepod's powerful escape and to track the high-speed swimming trajectory of an escaping animal at 1 m s^{-1}. With 1280 x 800 pixels, the spatial resolution of the cameras is sufficient to resolve fine velocity structures that an animal may produce. Each camera is equipped with a 30 mm extension ring, a 2× teleconverter, and a 200 mm focal length lens (Nikon, Tokyo, Japan) in order to obtain a field of view of approximately 1 to 2 cm^2. The aperture is generally set to f/11 or f/16 to maintain a large depth of field. Scheimpflug mounts are used to correct for off-axis viewing distortion. As shown in Figure 4.1, the four cameras are positioned on one side of the interrogation volume (inside an aquarium) via three-axis gear heads (Manfrotto, Cassola, Italy) and high-rigidity optical rails, all of which are mounted on an optical table. The gear heads were used to roll the cameras to an angle that accommodated the Scheimpflug mounts.

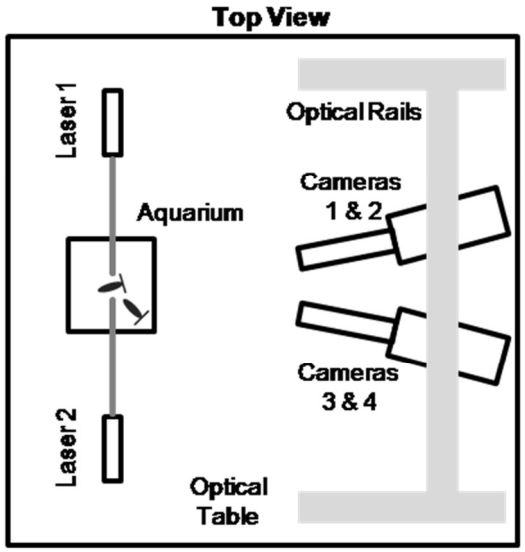

Figure 4.1 Diagram of setup of tomographic PIV system.

The target volume is illuminated by two continuous wave 7 W lasers (CrystaLaser, Reno, NV) lasing with a near-infrared (IR) wavelength (808 nm). Previous tests have shown that the target copepod species are not affected by light in the near-IR wavelengths (Catton et al. 2007, 2012). The two lasers are positioned in a counter-propagating manner to minimize shadowing of the tracer particles by the presence of the animal. The laser beam is expanded and collimated using spherical plano-concave and biconvex lenses, and an adjustable aperture is used to create a beam with rectangular cross-section of approximately 20 × 8 mm (height × width). The width of the beam defines the depth of the illuminated interrogation volume from the view of the cameras. The positive z-axis was defined as pointing towards the cameras, with the x- and y-axes defined as horizontal and vertical, respectively, in the imaged plane.

Image acquisition is controlled through DaVis software (LaVision, Ypsilanti, MI) on a laptop PC and is synchronized by a high-speed controller that generates timing signals for the cameras. Images are pre-processed (sliding minimum subtraction over 3 × 3 pixels; normalization with local average over 100 × 100 pixels; Gaussian smoothing and subsequent sharpening of particles), and volume self-calibration is iteratively performed to correct for errors in the calibration (Wieneke 2008). Images are reconstructed into a light intensity volume by the MART algorithm in DaVis. Reconstructions with an animal in the field of view present a problem since the reconstructed animal contaminates the subsequent volumetric cross-correlations, leading to spurious vectors representing animal motion rather than fluid motion. Following the technique of Adhikari and Longmire (2012), the animal is volumetrically masked out of the reconstructed volume using the visual hull method (illustrated in Figure 4.2). For each time point the animal is traced manually in each of the four camera images in DaVis. Each image is binarized so that the animal has a value of unity while the background has a value of zero. The four animal silhouettes are back-projected into a volume and multiplied together using the Multiplicative Line of Sight (MLOS) algorithm in DaVis. The volume in which the four back-projections intersect is the animal's visual hull. This visual hull is then applied as a mask to the reconstructed volume; thus all light variation within the volume occupied by the animal was removed. After the masking, consecutive reconstructed volumes are cross-correlated in a multi-pass process to produce a volume field of three-component velocity vectors. A 24-processor server is used to perform these computations.

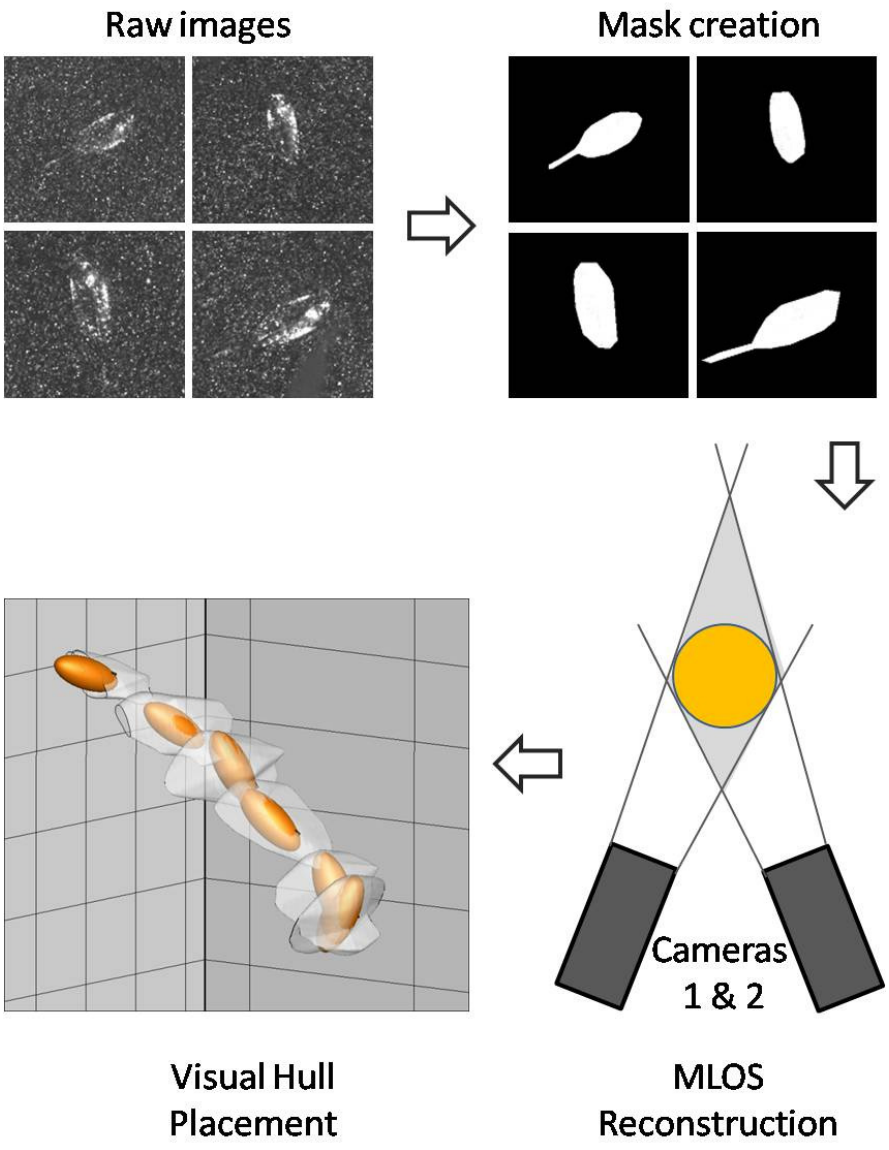

Figure 4.2 The animal body in the raw images is manually masked to create a visual hull at each time point. The animal silhouette in each image is then back-projected to define the volume surrounding the animal. The shaded, diamond-shaped intersection of the back-projections is found by the MLOS algorithm (illustration shown for a two-dimensional example). The visual hull for each animal position, illustrated in the final panel, shows that a good match is achieved between the visual hull (transparent gray envelope) and the animal outline (orange prolate spheroids). The visual hull does not completely surround the left-most prolate spheroid because the copepod has partially exited the imaged volume at this time point.

Once images of zooplankton behavior are acquired and processed into velocity vector volumes, it is necessary to accurately represent the animal's position and orientation within the volume at each time point. The visual hull, which represents the maximum volume possibly occupied by the animal, can be used to estimate the animal's position and orientation. However, in order to measure kinematic parameters such as swimming speed, a more precise 3D point tracking technique is required. The raw PIV and calibration images from the four cameras therefore are exported to DLTdv5, a MATLAB-based digitization program (Hedrick 2008). After calibrating the system with the Direct Linear Transform (DLT) method (using the same images used for tomographic PIV calibration), points on the head, tail, and antennal tips are digitized in each video to quantify their 3D coordinates. From the sequence of 3D positions, swimming speed and other kinematic parameters are calculated. In addition, a simple CAD model of the animal (generally consisting of a prolate spheroid with a 'rudder' indicating the position of the posterio-ventral swimming legs and thin, cylindrical antennules) is created in Solid Edge and imported into the volumetric flow field in TecPlot 360 (TecPlot, Bellevue, WA). The length and width of the model are based on measurements of the animal prosome made in DLTdv5. Coordinate transformations then are used to translate and rotate the model into the appropriate position in the flow field at each time point in the time-resolved flow, as determined by measurements of animal position in DLTdv5. As seen in Figure 4.2, the visual hull (imported into TecPlot as a CAD model) and the prolate spheroid match well, with the prolate spheroid rarely protruding through the visual hull surface. The prolate spheroid model therefore provides information on the animal orientation that is not evident from the visual hull.

In order to assess the capabilities of the described tomographic PIV system, measurements of an escaping copepod (*Calanus finmarchicus*) were taken. Images were acquired at 200 frames per second in an aquarium measuring 5 cm on each side filled with seawater at a temperature of 12°C. The copepod's prosome length was measured in DLTdv5 at 2.1 mm. The flow was seeded with titanium dioxide particles with a mean diameter of less than 10 μm. The copepod's escape jump was self-initiated and possibly was triggered by the approach of a second copepod (which is visible at the edge of the original images for the example presented herein). The field of view of each camera was approximately 19 × 13 mm, and a volume of 12 × 13.5 × 7.5 mm (x × y × z) was reconstructed. The reconstructed volume was approximately 187 times greater than the copepod volume. Cross correlation between consecutive volumes, with a window size decreasing down to 48 cubic pixels and an overlap of 75%, resulted in vector spacing of approximately 0.2 mm. Due to the impulse that a copepod escape jump applies to the surrounding fluid, the resulting flow field contains highly localized velocity peaks, and great care was taken in ensuring that only truly spurious vectors were removed and replaced. The universal outlier detection scheme (with a remove threshold of 4) was applied to remove and replace spurious vectors (Westerweel and Scarano 2005). In order to preserve steep velocity gradients, the resulting three dimensional velocity field was only lightly smoothed in the DaVis software with a 3 × 3 × 3 smoothing kernel with a strength of 0.05 (where a strength of 0 corresponds to no smoothing, 0.5 corresponds to Gaussian smoothing, and 1 corresponds to local averaging).

4.3. Assessment

The capabilities of the tomographic PIV system and the new opportunities opened by the acquisition of volumetric velocity data around zooplankton will be demonstrated by analysis of an escape event by a calanoid copepod. The copepod escape kinematics will be presented first, followed by a demonstration of three unique capabilities of the tomographic PIV system. First, time-resolved flow measurements surrounding the escaping animal will be presented and compared to a computational fluid dynamics (CFD) simulation (Jiang and Kiørboe 2011a) and two analytical solutions that model the flow (Kiørboe et al. 2010a, Jiang and Kiørboe 2011b). Second, a volumetric measurement of the flow disturbance generated by the escaping copepod then will be presented. Finally, the energy dissipated by viscous effects will be calculated based on spatial gradients of velocity and used to estimate the energy expended by the copepod to accomplish the jump. The results in all three cases are compared with relevant data for other copepod species in order to highlight the capabilities of the tomographic PIV system and to accentuate the added informational advantage of volumetric velocity fields.

4.3.1. Kinematics

Figure 4.3 shows the position of the smaller (escaping) copepod at consecutive time points during its escape and the position of the larger copepod (with antennules) at the time point at which the smaller copepod initiates its escape. The antennules of the smaller copepod could not be located in the PIV images (and hence are not shown). The larger copepod is swimming upward at an average speed of approximately 20 mm s^{-1}. The first position of the smaller copepod (nearest the larger copepod) represents its initial

stationary position (t = 0 ms). In its second position (t = 5 ms), the copepod has reoriented its body's long axis by 46 degrees, likely by an extremely rapid (< 5 ms) manipulation of its urosome (Kiørboe et al. 2010b), and is accelerating into its escape jump (directed away from the larger approaching animal) at a speed of 114 mm s^{-1}. A time record of the animal's speed is shown in Figure 4.4. In its third position (t = 10 ms), the escaping copepod is travelling at a speed of 479 mm s^{-1}. Between its second and third positions, the copepod accelerates at approximately 73 m s^{-2} (or 7.4 g). The copepod speed decreases to 316 mm s^{-1} in its fourth position as the swimming legs recover. Swimming leg recovery (and possible urosome action) also seem to rotate the body so that the nose is yawed to a more vertical position, an effect also seen by Kiørboe et al. (2010b). A second power stroke between the fourth and fifth positions then increases its speed to its maximum of 522 mm s^{-1}. The second power stroke also reorients the animal on a slightly more horizontal trajectory. After the sixth position shown in Figure 4.3, the escaping copepod exits the field of view.

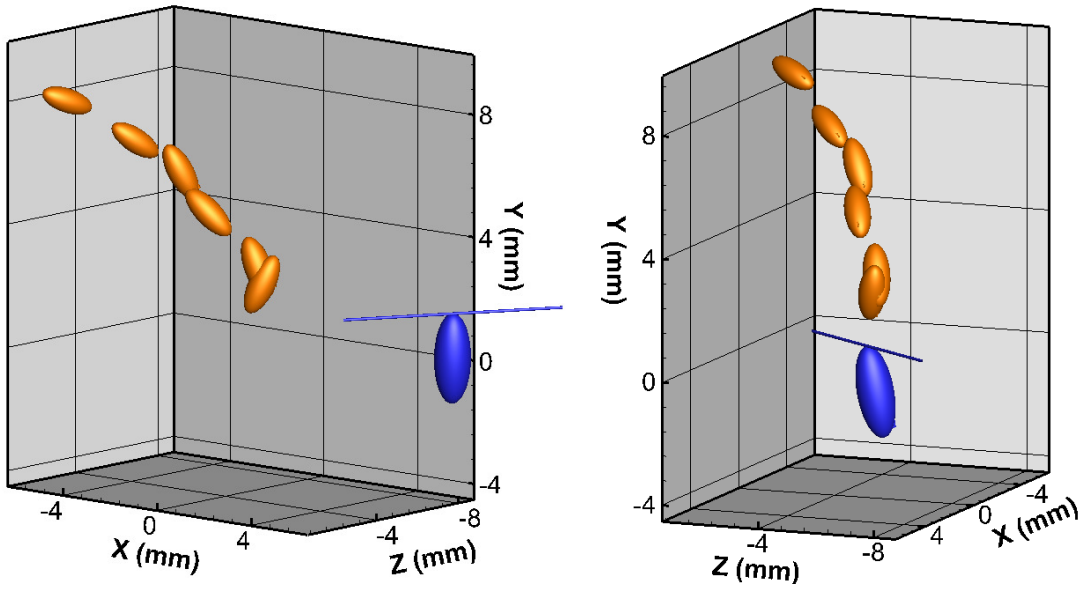

Figure 4.3 Two views of the three dimensional escape trajectory of the smaller copepod (orange prolate spheroid) away from the larger copepod (blue prolate spheroid with antennules). The escaping copepod positions correspond to consecutive time points and are separated by 5 ms (the distance from the larger copepod increases with time). A protruding black 'rudder' on the small copepod (facing the viewer in the image on the right) represents its posterior ventral side.

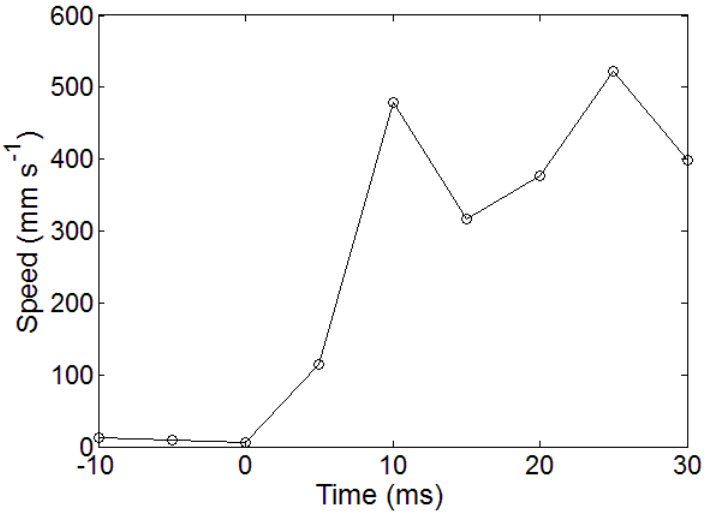

Figure 4.4 Speed of the escaping copepod as a function of time. The copepod accelerates from rest to 479 mm s^{-1} within 10 ms.

4.3.2. Flow Measurements

The flow generated by the copepod in the 20 ms following initiation of its escape is shown in the four frames in Figure 4.5. A single oblique plane is plotted in Figure 4.5, and the plane is aligned with the dorso-ventral plane of the copepod at the initiation of the escape. Each of these frames represents a time period of 5 ms over which two consecutive images were cross-correlated to measure the flow motion, and the copepod position at the beginning and end of this time period is shown. It is also important to note that by 15 ms after the jump initiation, the copepod has left the represented plane. For ease of viewing, only the components of the velocity vectors parallel to the plane are plotted. Finally, areas in the plane in which vectors are absent represent the volume masked by the visual hull (i.e. occluded by the animal).

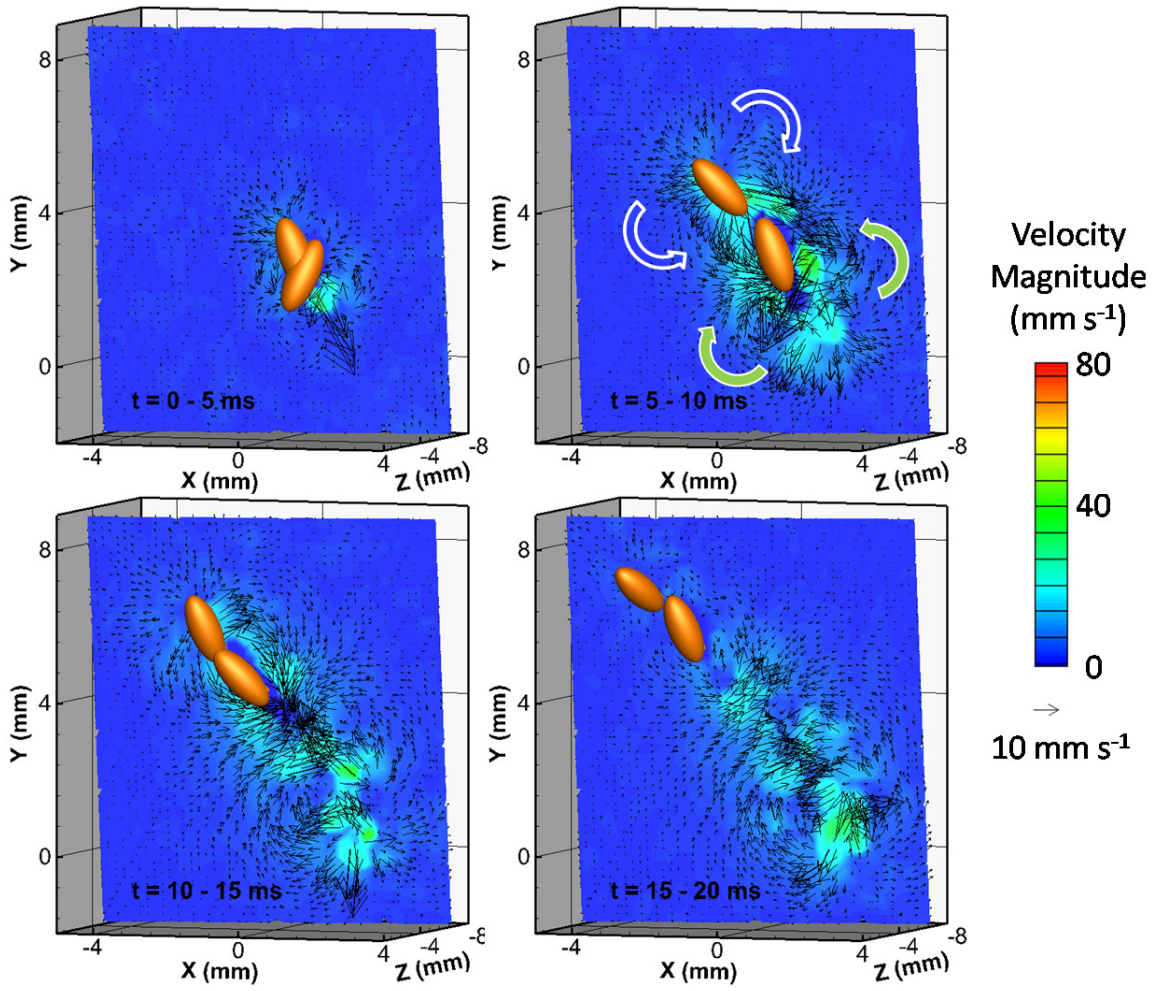

Figure 4.5 Flow created by the escaping copepod in the 20 ms following jump initiation. The right side of the spheroid corresponds to the copepod's ventral surface, and the left side corresponds to its dorsal surface. A single oblique plane is shown that is aligned with the dorso-ventral plane of the copepod at the beginning of its jump. Vectors indicate the local velocity and the color contours represent velocity magnitude. Only every other vector is displayed for the sake of clarity. Each frame represents the flow field corresponding to a 5 ms period (as noted). The position of the copepod at the beginning and end of the time period is shown. In the second panel (5-10 ms), the body vortex motion and location are indicated by the hollow curved arrows while that of the wake vortex are indicated by the solid green arrows.

Within the first 5 ms, the animal reorients and metachronally strikes with its swimming legs. As seen in the first frame, this motion creates a highly localized impulsive jet directly behind the animal, with flow speeds up to 50 mm s^{-1}. This jet is likely due to the most posterior pair of swimming legs which strike first and may sweep backwards unobstructed by other leg pairs (Murphy et al. 2011). The jet immediately forms into a toroidal wake vortex (indicated by the filled arrows) as the fluid curls forward to fill the space evacuated by the animal. As the copepod is accelerated forward by this impulsive transfer of momentum to the fluid, it pushes the fluid in front of it forward and to the sides. This fluid also curls around to fill the space evacuated by the animal to form a weaker body vortex (indicated by the hollow arrows).

The copepod continues to accelerate in the subsequent frame (t = 5-10 ms), and the flow disturbance created by the animal greatly increases. The effect of the swimming legs on creating flow asymmetry around the animal is particularly noticeable. The flow on the ventral side of the animal is much greater than that on the dorsal side. The larger velocity on the ventral side at this time point represents flow being dragged down by the copepod's more anterior (thus later striking) swimming legs. The toroidal vortex in the wake of the animal continues to develop and decay in the two subsequent frames. As the animal travels at high speed in the period 10 to 20 ms after jump initiation, it continues to form a travelling body vortex as it pushes forward. This flow feature isn't seen in the last frame of this sequence since the animal's anterior prosome has left the represented plane. In the period 15 to 20 ms after the initial jump, the copepod recovers its swimming legs

and performs another power stroke. The flow associated with this stroke is not apparent in Figure 4.5 since the animal has largely left the represented plane by this time.

Figure 4.6 shows the flow created by the copepod on a longer time scale of 125 ms, represented by five time-averaged intervals of 25 ms each, with a final time-averaged frame showing 500 - 530 ms. The oblique plane represented in Figure 4.6 (the same as that shown in Figure 4.5) illustrates the effect of the second power stroke, and the contours of the z-component of vorticity demonstrates the rotation of the body and wake vortices. The initial body position (after the copepod has reoriented) is shown in the first frame. In the first 25 ms, both the wake vortex (solid curved arrows) and body vortex (hollow curved arrows) are evident, although the wake vortex appears to be much stronger. During the second time period shown (25 – 50 ms), ventral flow from the first power stroke becomes evident (white straight arrow). In addition, the initial body vortex appears to have been revitalized by the second power stroke (black straight arrow). This phenomenon is unexpected since a second power stroke has been assumed to create a wake vortex with the same sense of rotation as the first wake vortex that would cancel out the initial body vortex (Jiang and Kiørboe 2011a). Two factors appear to cause this alteration, and both are related to the significant body rotation (yawing) that the copepod undergoes throughout its stroke. First, the copepod yaws (nose-upward) as it recovers its swimming legs. Its posterior end therefore drags fluid in its wake, which strengthens the vortex ring on its dorsal side. Second, the copepod is yawed (nose-downward) by the power stroke of the posterior-most swimming legs. The resulting momentum impulse of the second power stroke therefore is angled such that it re-energizes the vortex core that formed on its ventral side. This development is made more apparent in the third frame

(50 – 75 ms), as a strong flow with speeds up to 40 mm s^{-1} develops ventrally from the second power stroke. The vortex rings continue to evolve in the next two frames (75 – 100 ms and 100 – 125 ms) as they decay and separate from each other. The last frame in Figure 4.6 shows the flow at 500 ms after jump initiation (a time average of the flow over a 30 ms interval). At this time point, circulation from the body and wake vortices has dissipated, but posterior flows with speeds up to 5 mm s^{-1} resulting from both copepod power strokes still are evident (indicated by white and black arrows).

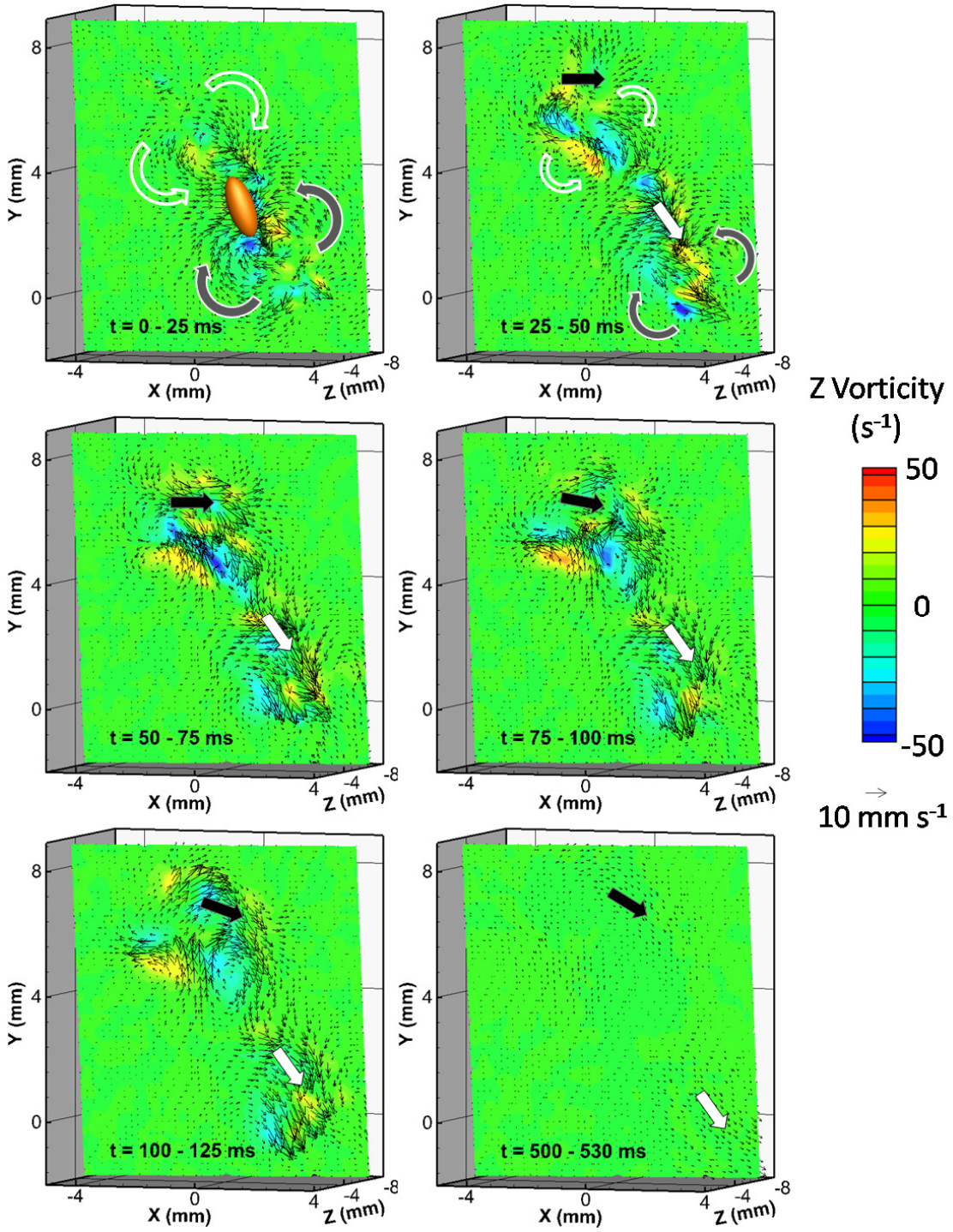

Figure 4.6 Flow created by copepod escape jump composed of two power strokes. Velocity vectors are averaged over the indicated time intervals after jump initiation. A single oblique plane is shown that is aligned with the dorso-ventral plane of the copepod at the beginning of its jump. Vectors indicate the local velocity and the color contours represent the z-component of vorticity. Only every other vector is displayed for the sake of clarity.

Figure 4.7 schematically summarizes the main flow features found in this copepod jump. In panel A, the copepod has just begun its metachronal swimming stroke with its posterior-most swimming legs and by this action has initiated a wake vortex and body vortex. In panel B, the power strokes of the remaining swimming legs have dragged down a posteriorly directed jet-like flow ventral to the animal. In panel C, this jet moves the ventral region of the toroidal wake vortex in a ventral direction (a phenomenon that will be quantified below). Also in panel C, the copepod has moved through its initial body vortex and recovered its swimming legs for another stroke, an action that has yawed the animal nose upward (into a more vertical position). This rotation creates a strong dorsal flow by directing the flow dragged behind the animal in a dorsal direction. In panel D, the copepod kicks again, which rotates its body nose downward into a more horizontal orientation. The flow created by the copepod's second kick then is directed toward and strengthens the ventral side of the initial body vortex.

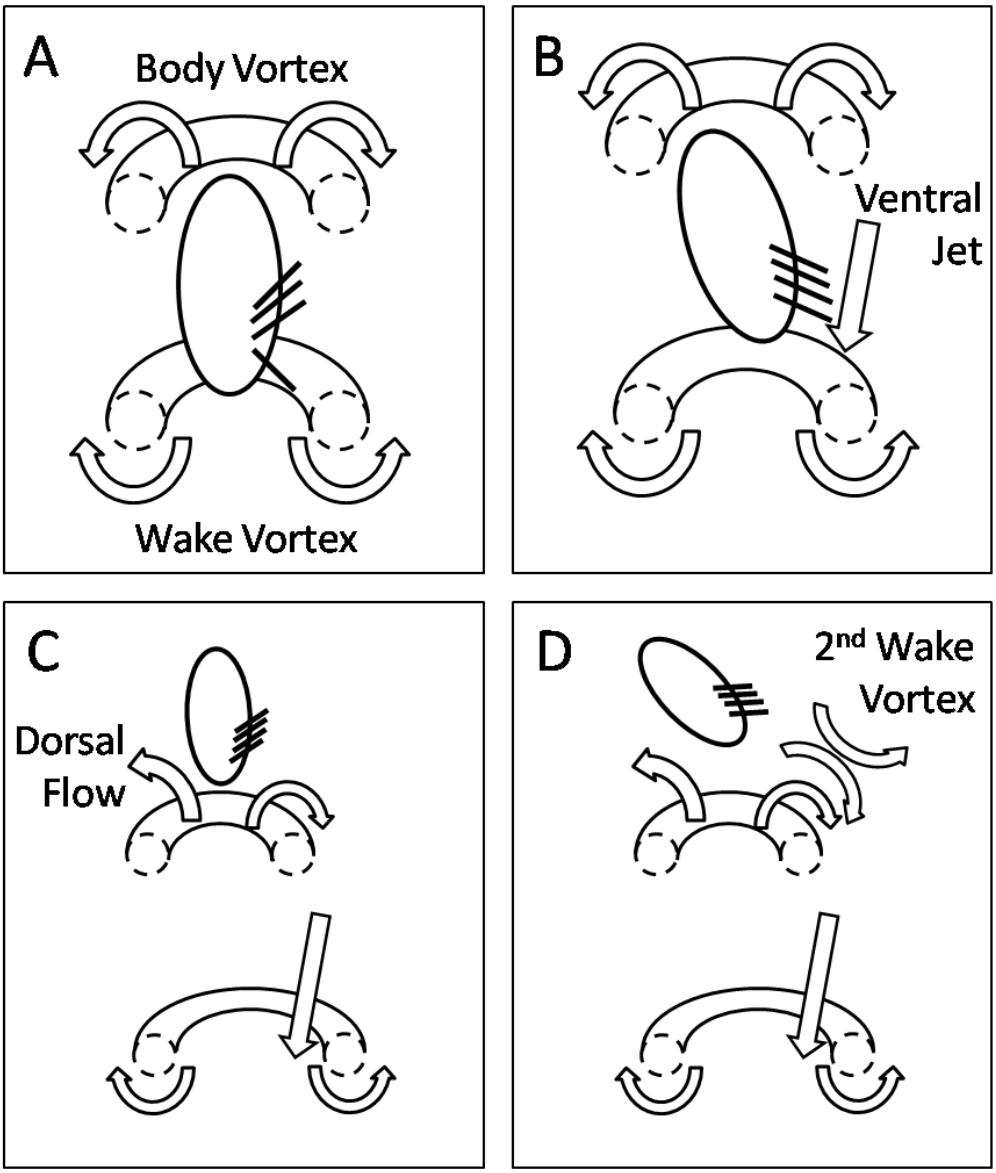

Figure 4.7 Diagram presenting the flow sequence created by the escape jump of a copepod.

4.3.3. Comparison with CFD

A volumetric flow measurement technique such as tomographic PIV also allows further investigation into the characteristics of the flow produced by the copepod escape jump that could not be addressed using planar or stereo PIV and allows validation of assumptions made in 3D computational fluid dynamics (CFD) models. The CFD simulation of Jiang and Kiørboe (2011a) modeling the escape jump (with 7 power strokes) of a 3 mm long *Calanus finmarchicus* copepod (modeled as a prolate spheroid) escaping at a maximum speed of 732 mm s^{-1} provides a useful point of comparison. In this simulation, the copepod's metachronal power stroke was approximated as an azimuthally axisymmetric swimming leg force that was swept anterior to posterior in an arc meant to cover the volume swept out by the swimming legs during an actual power stroke. These researchers found that the dominant flow features were a wake vortex that remained at the animal's initial position and a similarly sized body vortex that moved with the animal, both of which were persistent features. In addition, a trail of flow dragged along its path by the copepod was accompanied by periodic bursts of vorticity (of the same sign as the wake vortex) that indicated additional power strokes. These vorticity bursts were found to quickly decay and disappear as they interacted with the flow trail, which had an opposite sign of vorticity.

While agreeing with the main features of Jiang and Kiørboe's simulation (2011a), two significant and instructive differences with the current experimental work exist, and the three-dimensional nature of the measurements allows these to be examined in detail. The greatest difference between these experiments and the simulations is that the flow created by the second power stroke did not roll up into a burst of vorticity with the same sign as

the initial wake vortex and effectively cancel the body vortex. Instead, as seen in Figure 4.6, flow from the second power stroke re-energized the ventral side of the body vortex that was initially formed when the copepod accelerated through that volume. The resulting flow consisted of a pair of oppositely signed toroidal vortices (the wake vortex and the body vortex) that did not dissipate quickly but were persistent in time. This difference largely depends on significant body rotation (yawing) that was not accounted for in the simulation. A second difference, the effect of the swimming legs on the distribution and asymmetry of the flow in the wake vortex, is apparent in Figure 4.6. Whereas in the simulation, the swimming leg force swept front to back to create a single flow feature (an impulsive wake vortex), in the experiments, the posterior-most swimming legs (which strike first) created the impulsive wake vortex while the later-striking anterior legs created a jet-like flow to the ventral side of the animal's initial position. As will be shown, this strong flow substantially affects the ventral position of the wake vortex, thereby creating asymmetry in the wake vortex. The strength of the wake vortex seems to be affected to a lesser extent. These two differences between the empirically-derived and model results will be examined in greater detail and analyzed with the aid of analytical flow models.

4.3.3.1 *Body Vortex*

Various analytical models such as an impulsive Stokeslet and an impulsive stresslet have been proposed to model the flow associated with various copepod jumping behaviors (Kiørboe et al. 2010a, Jiang and Kiørboe 2011b). An impulsive Stokeslet consists of an impulsive force applied at a point in the fluid, whereas an impulsive stresslet consists of two opposed forces impulsively applied at a point in the fluid. The impulsive stresslet has

been found to nicely match the flow produced by a short copepod jump (of approximately 1 – 2 body lengths), in which the animal's body vortex and wake vortex remain close to and interact with each other (Jiang and Kiørboe 2011a). Based on CFD simulations, Jiang and Kiorboe (2011a) proposed that long escape jumps could be modeled as an impulsive Stokeslet since their simulation showed that the body vortex is pushed along in front of the escaping animal, leaving the wake vortex to decay alone. The experiments presented here, however, show both a persistent wake vortex and body vortex initiated by the copepod escape jump. This raises the question of whether the flow of copepod escape jumps should be modeled by an impulsive stresslet rather than an impulsive Stokeslet.

The circulation Γ of a vortex in a meridional half-plane (such that the vorticity is single-signed) produced by an impulsive Stokeslet is:

$$\Gamma(\mathrm{t}) = \frac{I}{4\pi\nu t}$$

where *I* is the hydrodynamic impulse. The circulation Γ of a vortex (either the wake or body vortex) in a meridional half-plane (such that the vorticity is single-signed) produced by an impulsive stresslet is:

$$\Gamma(t) = \frac{M}{8(\pi\nu t)^{3/2}}$$

where M is the impulsive stresslet strength. Nonlinear regression can be used to fit the measured circulation of the vortex core to reveal which analytical model is a better fit. It can also provide insight into the symmetry of the wake and body vortices. Circulation can be measured by performing a line integral of the velocity component tangential to the line integral pathway around a closed curve according to:

$$\Gamma = \oint \vec{v} \cdot d\vec{r}$$

As shown in Figure 4.8a, eight rectangular pathways (measuring 5 mm × 3.3 mm) encompassing the wake vortex circulation were defined in uniformly-spaced meridional planes surrounding the position of the copepod 5 ms after its jump initiation. Eight identically shaped pathways were similarly defined around the copepod position at 10 ms after jump initiation in order to measure the body vortex circulation. An approximately 20° change in the copeopd's swimming direction between these two time points is therefore reflected in the line integral pathway positions. In the wake vortex pathways, the closed curve's uppermost inner corner corresponds to the center of the animal's position at 5 ms after jump initiation. In the body vortex pathways, the center of the long side of the pathway corresponds to the center of the animal's position at 10 ms after jump initiation. Initial pathways were constructed to align as closely as possible to the animal's dorsoventral and mediolateral planes (as measured from DLTdv5), and subsequent pathways were constructed at uniform angle spacing relative to these (Figure 4.8a). Pathways in the wake vortex measurement that extended beyond the measured volume were modified to follow the edge of the measured volume. Circulation was calculated at each time point for both the body and wake vortices using these pathways. Figure 4.8b shows an example of three dimensional velocity vectors along selected wake vortex and body vortex line integral pathways. The vectors clearly reflect the general pattern of a wake vortex and body vortex.

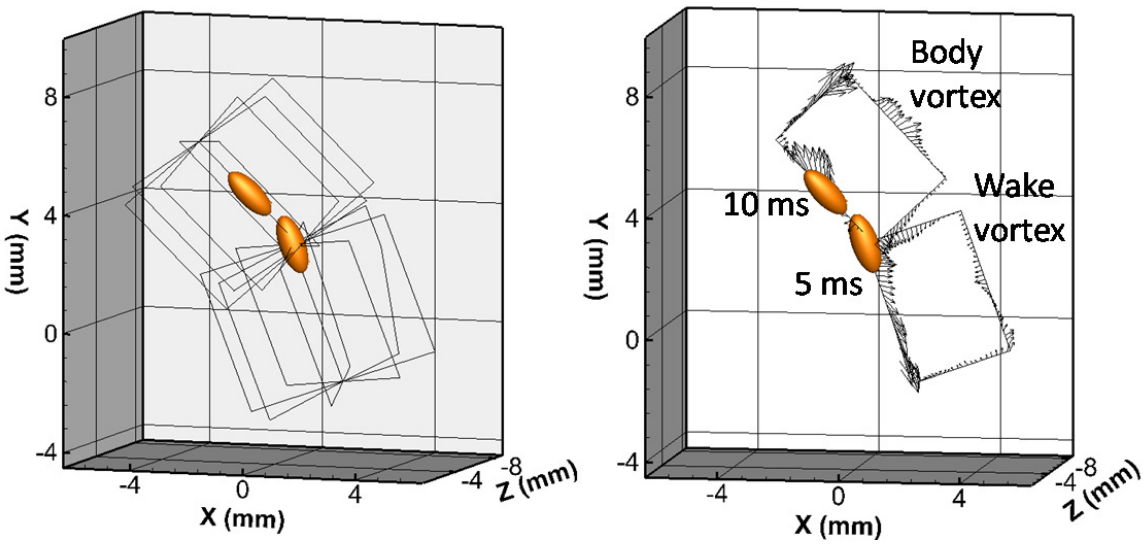

Figure 4.8 Illustration of pathways used to calculate circulation. The copepod body positions at 5 and 10 ms after jump initiation are shown (corresponding to the second panel of Figure 4.5). The left panel shows the eight integration pathways (azimuthally spaced at 45°) used to calculate circulation of both the wake and body vortices. The right panel shows velocity vectors along two example line integration pathways to illustrate the process.

Figure 4.9 shows the time series of circulation in each of the eight meridional half-planes for the wake vortex and body vortex. In each case, the circulation spikes soon after the animal begins its jump. In every case except for plane 7 for the body vortex (in which a strong flow from the copepod's second kick is evident), the circulation quickly decays. The azimuthally-averaged wake vortex circulation (beginning at 0.125 s) was fit to the impulsive stresslet and impulsive Stokeslet models by nonlinear regression (Figure 4.10). The root-mean-square of the residual error for the impulsive stresslet fit was 1.1 whereas that for the impulsive Stokeslet fit was 1.8. Therefore, the temporal pattern of the flow generated by the escaping copepod is better described by the impulsive stresslet model. The impulsive stresslet strength of the wake vortex (averaged for the eight planes) was 77.7 $mm^5\ s^{-1}$, whereas that for the body vortex (excluding plane 7) was 26 $mm^5\ s^{-1}$. Thus,

there is an asymmetry between the stronger wake vortex and weaker body vortex (which appears to decay more quickly in Figure 4.9). The peak circulation of the wake vortex found in these experiments (42 mm^2 s^{-1} from Figure 4.9) is compared with values found by other researchers both experimentally and computationally for other species performing both escape and repositioning jumps in Figure 4.11. Smaller copepods such as *Acartia* and copepods performing shorter repositioning jumps generally produce smaller values of peak circulation. Larger copepods such as *Calanus*, which are able to generate higher impulsive forces, produce greater peak circulation.

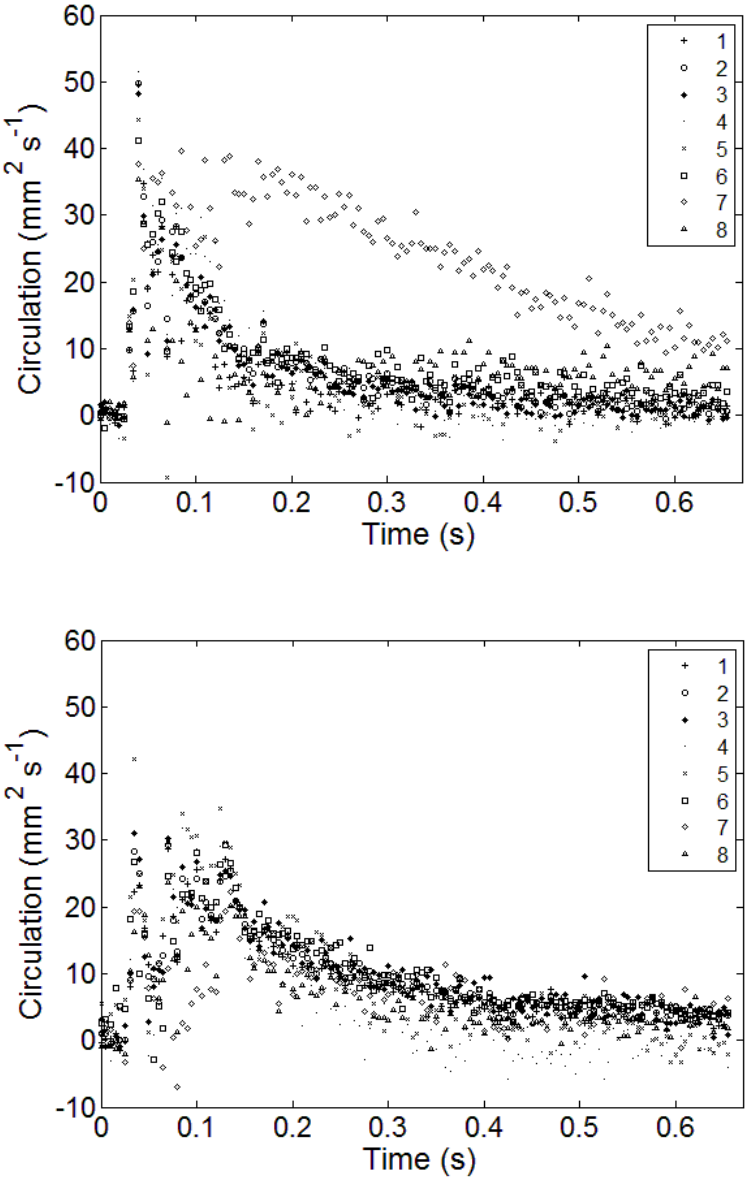

Figure 4.9 Circulation in each of the eight meridional half-planes (1 - 8) for the body vortex (top) and the wake vortex (bottom). The half-planes are azimuthally separated by 45°. Plane 7 corresponds to strong flow induced by the copepod's second kick.

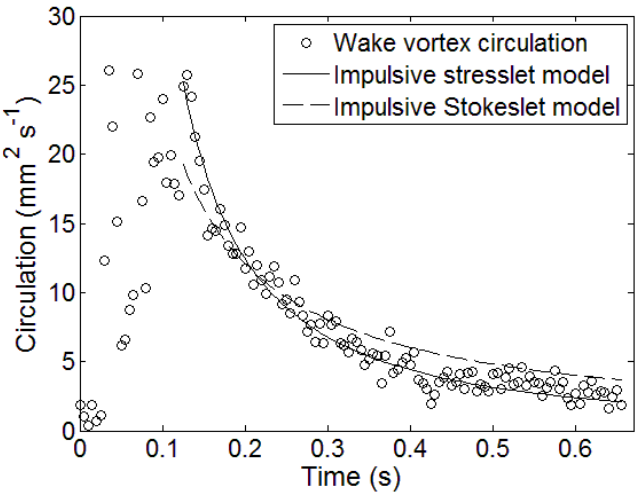

Figure 4.10 Wake vortex circulation averaged over the eight meridional half-planes with impulsive stresslet and impulsive Stokeslet models fitted to the data by nonlinear regression.

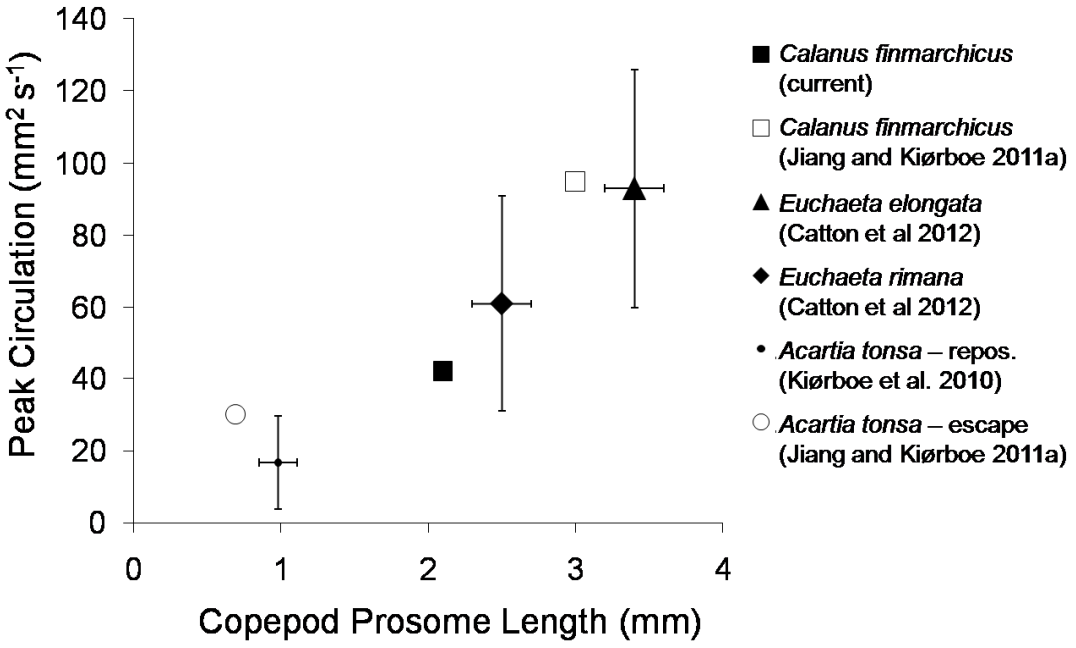

Figure 4.11 Peak circulation as a function of copepod prosome length. Each species is represented by a different symbol shape. Filled symbols represent experimental results whereas open symbols represent computational results. Large symbols represent escape jumps whereas small symbols represent repositioning jumps.

4.3.3.1 *Vortex Asymmetry*

A second difference between the experimental work here and the simulations of Jiang and Kiørboe (2011a) is the effect of the swimming legs on the distribution and asymmetry of the flow in the wake vortex. Webster and Longmire (1998) found that azimuthally asymmetric vortex rings propagated a shorter distance and died out more quickly than symmetric vortex rings. The possibility then arises that any asymmetry in the wake vortex produced by the action of the swimming legs could erase the animal's wake signature more quickly. This rapid vortex decay could more effectively camouflage the escaping copepod from the pursuit of predators. In order to investigate this possibility, the strength and position of the vortices in the meridional half planes surrounding the animal were examined.

The wake and body vortex strengths were examined by fitting the impulsive stresslet model to the circulation measured in each meridional half-plane (i.e. the pathways shown in Figure 4.8). Figure 4.12 shows the impulsive stresslet strength M in each half-plane (except for plane 7 for the body vortex, for which the impulsive stresslet model is not a good fit). The animal's ventral side is in the region of planes 6 and 7, and the dorsal side is in the region of planes 2 and 3. The wake vortex impulsive stresslet strength M seems to be slightly larger on the animal's ventral and dorsal sides than on its lateral sides. No strong pattern is seen in the distribution of the body vortex strength.

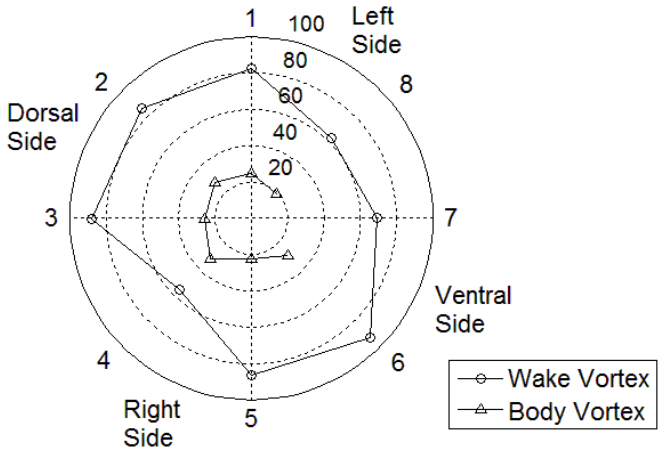

Figure 4.12 Impulsive stresslet strength (measured in $mm^5\ s^{-1}$) for the wake vortex and body vortex measured in each of the eight meridional half-planes surrounding the escaping copepod. As indicated, the copepod's ventral side is located in the region of planes 6 and 7 while its dorsal side is located in the region of planes 2 and 3.

The position of the vortex center is another measure by which the symmetry of the wake vortex can be investigated. The vortex center position is known analytically from the solution of the impulsive stresslet, and it has been shown that, in a cylindrical polar coordinate system (x, r, φ) where x is the axial distance, r is the radial distance, and φ is the azimuthal angle, the radial position of the vortex center relative to the central axis is, from Jiang and Kiørboe (2011b),

$$r(t) = 2.63505\sqrt{\nu t}$$

and the axial position of the vortex center relative to the point at which the impulsive force was applied is

$$x(t) = \mp 1.86326\sqrt{\nu t}\ .$$

Figure 4.13 reveals that the axial locations of the vortex centers for planes 2 and 6 match well with each other but not with the analytical prediction for the impulsive stresslet. Even accounting for an offset of approximately 1 mm (the distance from the center to the posterior of the prosome, where the impulsive force is more realistically applied), the wake vortex translates away from the origin much more quickly than the analytical prediction suggests it should. The radial location of the vortex center in plane 2 (dorsal) matches the analytical prediction of the impulsive stresslet quite well. The radial location of the vortex center in plane 6 (ventral), however, becomes much larger than the impulsive stresslet model suggests it should. The difference appears to be due to flow generated ventrally by the swimming legs. This flow, which can be seen beginning in the second frame of Figure 4.6, pushes the vortex center away from the central axis. The dorso-ventral stretching of the wake vortex could explain why the fitted impulsive stresslet strengths on the lateral sides of the animal were weaker in Figure 4.12. The wake vortex therefore seems to be slightly asymmetric in terms of vortex strength and extremely spatially asymmetric. The possibility of these characteristics leading to accelerated vortex dissipation and superior copepod camouflage will be discussed below.

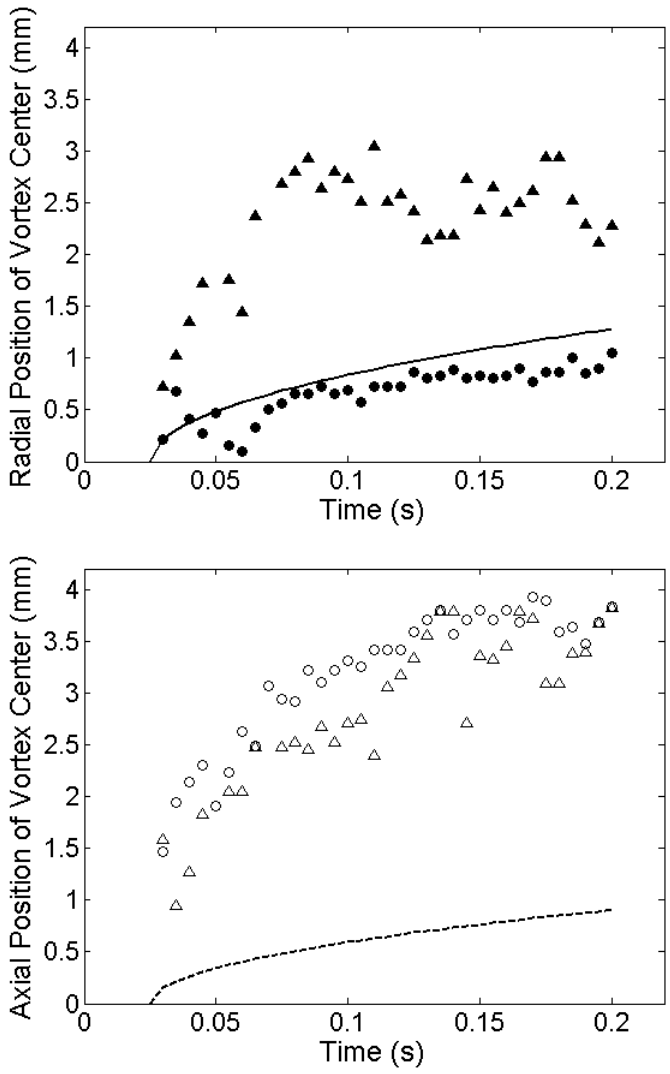

Figure 4.13 Radial and axial positions of the wake vortex center (stagnation point) in two opposing half planes, Planes 2 (circles) and 6 (triangles). The lines correspond to the analytical prediction.

Finally, the impulsive stresslet model analytically predicts that the positions of maximum vorticity and the vortex center (the flow stagnation point) will not coincide (Jiang and Kiørboe 2011b). Figure 4.14 illustrates this phenomenon on the body vortex by showing an iso-surface of vorticity magnitude ($\omega = 53\ s^{-1}$) and a slice that displays velocity vectors and a color contour of vorticity in the z direction at a point in time 75 ms after jump initiation. The copepod has already exited the field of view by this time point, and the animal's earlier positions (at 5, 10, and 15 ms after jump initiation) are shown to illustrate its pathway. The three-dimensional iso-surface shows a "vortex ring" created by the passage of the copepod. However, the vector slice shows that this ring does not coincide with the vortex center (flow stagnation point), which is marked by the yellow arrow.

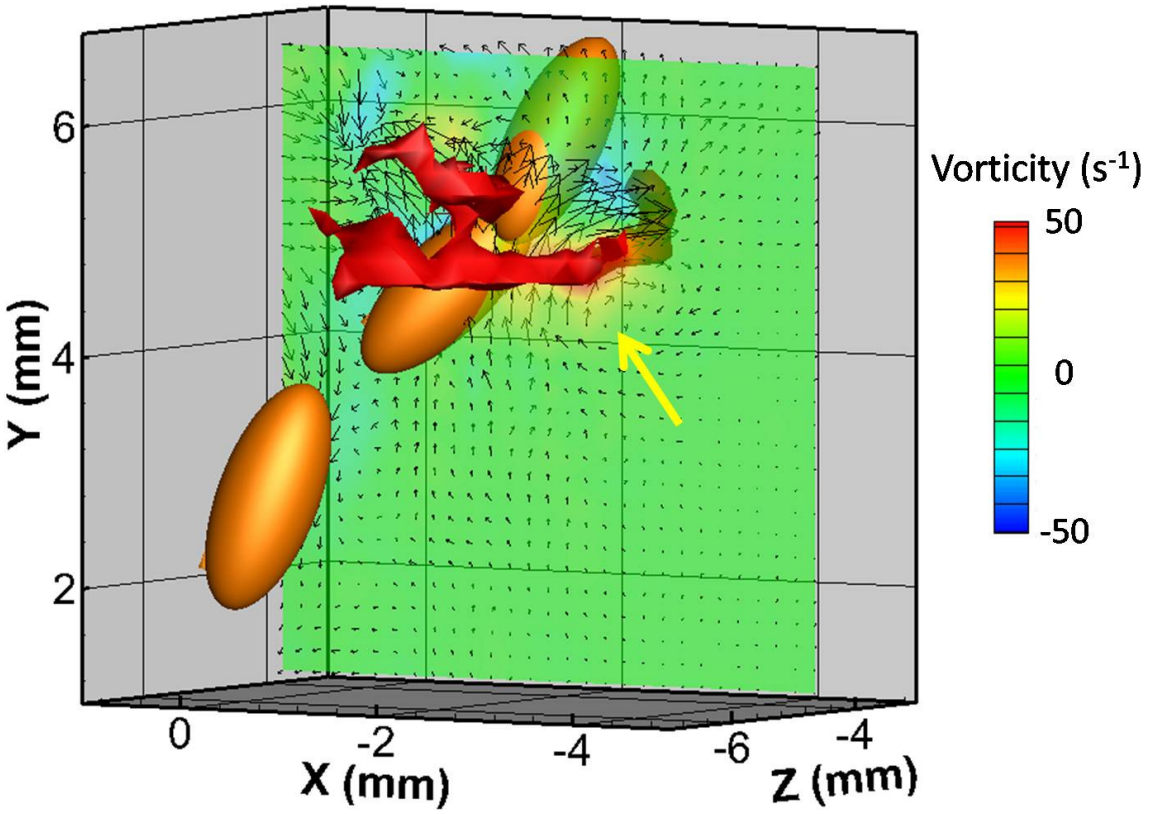

Figure 4.14 Formation of a body "vortex ring" from the passage of the escaping copepod at a point in time 75 ms after jump initiation. The copepod's earlier positions at 5, 10, and 15 ms after jump initiation are shown. The three-dimensional iso-surface shown around the copepod's pathway connects points in space that have a vorticity magnitude of 53 s^{-1}. Color contours in the plotted plane represent vorticity in the z direction. The yellow arrow indicates the center (stagnation point) of the body vortex while the three-dimensional iso-surface indicates the region in which vorticity magnitude is greatest. The separation of these two locations is characteristic of viscous vortices.

4.3.3.3. *Implications*

In sum, the tomographic PIV results of an escaping calanoid copepod have revealed a picture that is more complicated than the axisymmetric simulations of Jiang and Kiørboe (2011a) and the analytical models of the impulsive stresslet and impulsive Stokeslet. Instead of a single persistent wake vortex as predicted by the simulations and the impulsive Stokeslet model, the empirically derived results showed the presence of oppositely signed, persistent body and wake vortices, a pattern more reflective of the impulsive stresslet model. The body and wake vortices differed in strength, however, so it appears that the impulsive stresslet model does not perfectly correspond to the physical flow either (but is nonetheless useful for understanding the flow physics). The metachronal nature of the swimming leg stroke also gives rise to a flow disturbance that is more spatially distributed (along the path of the escaping copepod) than either the computational or analytical models appreciate. Furthermore, the experiments revealed azimuthal asymmetry caused by body yawing and the action of the swimming legs that was not predicted by the computational model. Similarly, Drescher et al (2010) found azimuthal flow asymmetry in the biflagellate green alga *Chlamydomonas reinhardtii*; this flow asymmetry did not match their axisymmetric model and was caused by three-dimensionality of the swimming appendage motion. In the copepod, strong ventral flows caused by the later-striking swimming legs during the first kick distort the initial wake vortex, and the flow generated by the second kick seems to ventrally strengthen, not cancel out, the initial body vortex. This strengthening effect was due to the copepod's body rotation after the first kick, a yaw that may be due to swimming leg recovery and urosome action (Jiang and Kiørboe 2011b). Body yawing also led to strengthened dorsal

flow as the copepod decelerated after its first power stroke. Copepods exhibit a high degree of directional control during their escape jump (the copepod here escaped in a direction away from a larger, approaching copepod), and so it is not clear whether this periodic yawing with every power and recovery stroke is a universal feature in all copepod jumps. The results of Jiang and Kiørboe (2011b) suggest, however, that it is a common feature and that it should be considered in future studies of copepod escape behavior. Contrary to the long-lasting flow trail pointing towards the copepod found in the simulation of Jiang and Kiørboe (2011a), periodic yawing also could serve to distort or break up the trail of flow dragged behind the copepod, thereby preventing predators from following its trail. Replicates of the current data set would be useful in better understanding this aspect of copepod escapes.

4.3.4. Hydromechanical Cue Extent

Tomographic PIV also has the ability to make volumetric measurements of the flow disturbance surrounding a swimming copepod. The volume around an animal in which the flow velocity exceeds a certain threshold is important when studying the vulnerability of zooplankton to predators since many predators are thought to use the velocity magnitude to detect prey (Kiørboe and Visser 1999). Velocity thresholds ranging from 1 to 10 mm s^{-1} have been used to define the hydrodynamic envelope surrounding different copepod species (Kiørboe et al. 2010a; Catton 2009). For the current study, velocity thresholds of 5 mm s^{-1} and 10 mm s^{-1} were selected as example thresholds, and the volume in the flow field in which the velocity generated by the animal exceeded each

threshold was found at each time point (Figure 4.15). Figure 4.15 shows that the volume exceeding the 5 mm s^{-1} threshold spikes to approximately 43 mm^3 (a volume 61 times greater than the copepod's volume) before dropping precipitously. Within 250 ms, the affected volume in the current experiment has dropped to 5 mm^3 (only 7 times the animal's volume). This pattern is markedly different from the high speed planar PIV analysis of smaller *Acartia tonsa* repositioning jumps performed by Kiørboe et al. (2010a), in which the area exceeding the thresholds ranging from 1 – 6 mm s^{-1} declined more gradually. This difference is partially explained by the three dimensional nature of the current work and also likely reflects a hydrodynamic difference between small copepods performing short repositioning jumps and larger copepods performing more powerful escape jumps.

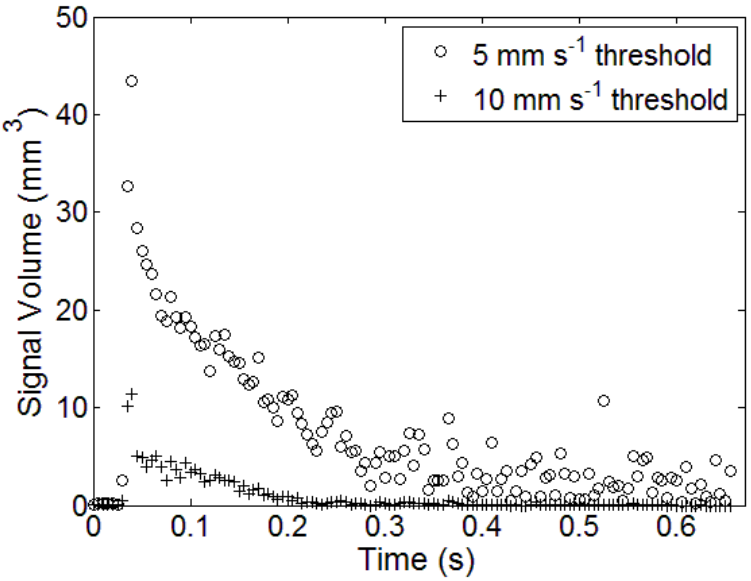

Figure 4.15 Volume for which the measured velocity exceeds thresholds of 5 and 10 mm s^{-1} following the escape jump of a *Calanus finmarchicus* copepod.

The data do not support the hypothesis that azimuthal asymmetry in the wake and body vortices cause the vortices to break down more quickly than would otherwise be the case. Jiang and Kiørboe (2011b) showed using dimensional analysis for the impulsive stresslet that the time t^* required for the entire flow field to fall below a velocity threshold U^* is:

$$t^* = \frac{0.068}{\nu}\left(\frac{M}{U^*}\right)^{1/2}$$

where M is the impulsive stresslet strength. Using the calculated value of M = 77.7 mm^5 s^{-1} and a velocity threshold of U^* = 5 mm s^{-1}, the required time t* was found to be 255 ms. However, according to Figure 4.15, a volume of 4 mm^3 contains velocity greater than the 5 mm s^{-1} threshold value at this time point. An additional 150 ms is required for the flow to fall beneath the threshold. Considering that the impulsive stresslet models the flow fairly well, it seems unlikely that the vortex asymmetry measured here contributes to accelerated vortex dissipation. On the contrary, hydrodynamic camouflage is likely not a high priority for the copepod during the initial part of its escape. Impulsively creating a large, persistent flow disturbance at its starting point (as was measured in this experiment) is likely a necessary component of its high-speed, long distance escape strategy. At a point several body lengths away from its starting point, however, stealth likely becomes more important, and it seems plausible that a much smaller hydrodynamic signature during the remainder of its escape would be a useful survival strategy for the copepod.

4.3.5 Viscous Energy Dissipation

An additional advantage of three-dimensional velocity measurements is the ability to directly quantify velocity gradients in all directions. Specifically, tomographic PIV allows direct estimates of the viscous energy dissipation rate ψ (with units of W m^{-3}), which is defined as:

$$\psi = \mu\left[2\left(\frac{\partial u_x}{\partial x}\right)^2 + 2\left(\frac{\partial u_y}{\partial y}\right)^2 + 2\left(\frac{\partial u_z}{\partial z}\right)^2 + \left(\frac{\partial u_x}{\partial y} + \frac{\partial u_y}{\partial x}\right)^2 + \left(\frac{\partial u_x}{\partial z} + \frac{\partial u_z}{\partial x}\right)^2 + \left(\frac{\partial u_y}{\partial z} + \frac{\partial u_z}{\partial y}\right)^2\right]$$

Integrating ψ over a volume gives the total energy dissipation rate. Previous estimates of dissipation rate using planar PIV were not able to measure the velocity in the *z* direction or directly determine derivatives in the z direction. The $\partial u_z/\partial z$ term was estimated using the incompressible Continuity equation and the other unknown terms involving the *z*-derivative were assumed to be approximately equal to one of the measured terms (Catton et al. 2007). Furthermore, because velocity data were limited to one plane with planar PIV, previous researchers either had to assume some type of body axisymmetry to obtain a volumetric measure of energy dissipation (Yen et al. 1991; van Duren and Videler 2003) or calculate a reduced dimension (i.e. 2D) parameter with the units of W m^{-1} (Catton et al. 2007). Tomographic PIV allows all of the terms to be directly calculated. For the escape event presented herein, ψ was calculated at each time point and was integrated over the measurement volume to give the total viscous energy dissipation rate (Figure 4.16). The energy dissipation rate spikes to approximately 4.4 x 10^{-7} W before

quickly dropping. Peak values are therefore one to two orders of magnitude greater than that estimated for tethered *Temora longicornis* (van Duren and Videler 2003), which is a smaller copepod species. In addition, a reduced dimension (i.e. 2D) dissipation rate estimate (in W m^{-1}) calculated from one plane in the velocity field intersecting the animal showed that the 2D estimate used by Catton et al (2007) and the 3D estimate of ψ (integrated over an area in the plane) gave similar results, thereby confirming that the 2D estimate used in the past is a valid technique for comparing trends and relative values (but not absolute magnitudes) in dissipation rate.

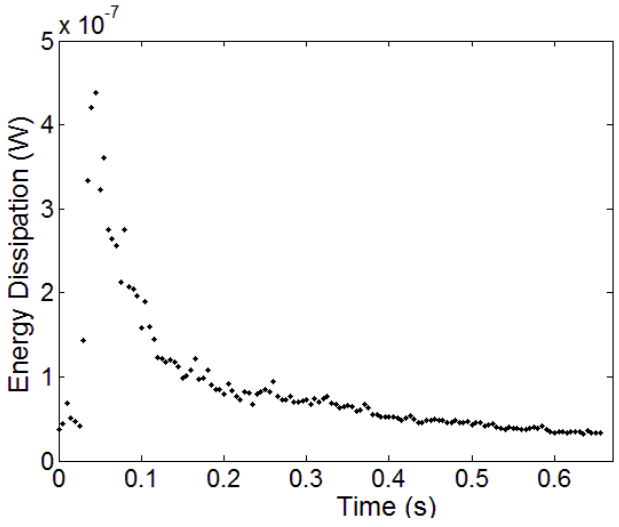

Figure 4.16 Viscous energy dissipation as a function of time during an escape jump by *Calanus finmarchicus*.

Power expended by the swimming leg muscles can be estimated from measurements of the energy dissipated in the water and can yield insight into the high accelerations achieved by escaping copepods. Integrating the energy dissipation rate beginning from the time of jump initiation gives an estimate of 5.58×10^{-8} J for the total energy delivered to the fluid by the copepod's swimming legs. This value is smaller than but comparable to the simulated values of $1.6 - 9.8 \times 10^{-7}$ J found by Jiang and Kiørboe (2011a) for a larger copepod. Accounting for a hydromechanical efficiency of 0.97 (Jiang and Kiørboe 2011a) and a muscle efficiency of 0.25 (van Duren and Videler 2003) gives a value of 2.3×10^{-7} J for the work expended by the copepod in this experiment. Dividing this work by the amount of time over which the swimming legs acted (approximately 10 ms for two kicks) gives an estimate of 2.3×10^{-5} W for the power provided by the swimming legs. Applying the same efficiency values to an average specific power value of 20 W kg^{-1} from the simulations of Kiørboe et al (2010b) and assuming a copepod mass of 1 mg (corresponding to wet weight) gives an estimate of 8.25×10^{-5} W for the power expended by the swimming legs, a value which is only slightly larger than the current value. As noted by Kiørboe et al. (2010b) and Lenz et al. (2004), copepod muscles are able to provide power at levels significantly higher than other organisms, a capability that contributes to their success in performing high-acceleration, impulsive escapes.

The ratio of the power expended in an escape jump to that of the basal metabolism also provides insight into the relative cost of escaping and has been estimated as high as 400 (Strickler 1975; Alcaraz and Strickler 1988). In order to estimate the base metabolism, the prosome length was used to reckon the copepod's body mass (dry weight) as 0.19 mg

(Cohen and Lough 1981). Following the calculation of Jiang and Kiørboe (2011a) and using a conversion value of 20.1 J = 1 ml O_2 per individual per hour (van Duren and Videler 2003), the body mass and temperature (12°C) were used to estimate the metabolic rate (2.27×10^{-6} W) using the regression relationship of Ikeda et al. (2001). The escape jump energy consumption is therefore 1014% of (or 10.1 times greater than) the baseline metabolic rate. Jiang and Kiørboe (2011a) found, for the 3 mm long prolate spheroid model of an escaping *Calanus finmarchicus*, an energy consumption of 414% of the baseline metabolic rate. However, these values are not directly comparable since Jiang and Kiørboe (2011a) do not account for efficiency losses from the muscle (hence they instead compare the work done on the water to the metabolic rate) and since they divide the total work by the time during which the copepod is in motion as opposed to the much shorter time period over which the swimming legs act. These measurements therefore underscore the costliness of performing an escape jump and show how the viscous energy dissipation provided by high speed tomographic PIV can be used to build energy budgets for various behaviors such as swimming or generating a feeding current.

4.4. Discussion

The tomographic PIV system described here successfully answers the four challenges of planktonic PIV enumerated in the Introduction. The three-dimensional nature of zooplankton flow and swimming patterns has been overcome by illuminating and measuring within a volume with multiple cameras. The small spatial scale and high speeds of zooplankton behavior have been addressed by using a high speed camera

system with high magnification. Zooplankton phototaxis to visual light has been overcome by employing near-IR laser illumination. This system thus allows for the non-intrusive measurement of 3D velocity vectors in the volume around planktonic organisms at high spatial and temporal resolution without disturbance to the animal.

While a tomographic PIV system is comparatively easy to set up and use, processing and analysis of tomographic PIV data containing free-swimming zooplankton is time-consuming and complicated. One reason for this is the visual hull creation, which often requires manual tracing of the animal in multiple camera views. Automated masking based on an intensity threshold is possible in theory but proves difficult in practice due to unequal illumination across the animal's complicated morphology. Also, reconstruction of the light intensity field and cross-correlation of these fields is computationally intensive. Finally, visualization of three-dimensional vector fields (especially those containing arbitrary objects within them) is challenging and stretches the capabilities of current flow visualization techniques. While only one event is presented herein, the event was analyzed in depth with regard to the flow patterns produced, the flow signal created, and the energy used by the copepod in order to display the possibilities that tomographic PIV creates.

Despite the challenges enumerated above, tomographic PIV allows insight that was previously unavailable and is thus a valuable technique for investigating zooplankton behavior. As shown in the presented data of an escape jump by a *Calanus finmarchicus* copepod, measurement of volumetric flow fields is now possible. Highly three-dimensional and ephemeral flow patterns can now be directly measured without resorting to assumptions of spatial axisymmetry or flow steadiness that are often made when using

planar PIV. Also, assumptions made in CFD simulations and analytical models can be better grounded in reality. Analysis of the axisymmetry of the body and wake vortices created by the copepod jump, as shown here, would never have been possible without a volumetric technique. Volumetric measurements of flow can also lead to better estimates of filtration rates, encounter rates, and the cue extent created by various zooplankton species. In addition, direct measurement of parameters such as viscous dissipation rate that previously were unavailable or that required unrealistic assumptions of flow axisymmetry can be made in order to build better energy budgets for various animal behaviors. Finally, tomographic PIV could also be used to measure flow fields around zooplankton sensory appendages in order to quantify hydrodynamic signal thresholds for escape or other behaviors. In sum, tomographic PIV is a powerful new tool that allows quantification and analysis of the flow patterns produced by zooplankton and of the stimuli to which they respond.

CHAPTER 5

HYDRODYNAMICS OF ANTARCTIC KRILL HOVERING

In the final part of this study, the flow associated with metachronal hovering in Antarctic krill is experimentally and theoretically investigated in regards to the energy requirements of the pelagic lifestyle. Volumetric flow measurements of a hovering Antarctic krill are obtained and used to examine the flow generated by the pleopods and the pulsed, jet-like flow in the krill's wake. Actuator disk theory is used to make theoretical estimates of the induced power necessary to hover, the results of which are compared to induced power values calculated from measured flow gradients contributing to viscous energy dissipation. The Strouhal number for Antarctic krill swimming is found to remain in or near an energetically favorable range for both hovering and forward swimming.

5.1 Introduction

Pelagic animals must contend with the constant downward force of gravity in order to maintain their position in the water column, and various species have adopted different strategies to minimize the energy required to do so. Some fish, such as sharks, generate hydrodynamic lift with their pectoral fins when swimming while many other fish species possess a swimbladder that provides an upward buoyant force (Alexander, 1990; Pelster, 1998). The storage of lipids, which have a density 10-15% less than that of seawater, has also been shown to contribute to buoyancy control in zooplankton and fish (Campbell and Dower, 2003; Pelster, 1998). Tissue density is also an important part of the balance

between gravity and buoyancy, with some fish species decreasing skeletal mineralization or accumulating water in muscle tissues to decrease their excess weight (Pelster, 1998). Aleyev (1977) showed, for instance, that most pelagic fish and invertebrates (such as squid) have densities that very nearly match or only slightly exceed that of the seawater in which they live.

The Antarctic krill (*Euphausia superba*) is a notable outlier when considering tissue density. The tissue density of Antarctic krill is extremely high (1.060 - 1.070 g cm^{-3}), and this species lacks the buoyancy aids (such as a swimbladder or lipid storage) that characterize other pelagic species (Kils 1981). Even considering that Antarctic krill live in cold Antarctic seawater with a high density of 1.028 g cm^{-3}, the density difference between the seawater and the krill body still is greater than that found in other nektonic species (Aleyev, 1977). Kils (1981) showed that a non-swimming krill would sink to a depth of 500 m within 3 hours. For these reasons, it has been said that it seems that Antarctic krill are "not well-suited for a pelagic way of life" (Kils 1981).Antarctic krill, however, are an extremely successful species that dominates the biomass of the Southern Ocean (Knox, 1994). How then do Antarctic krill compensate for their exceptionally high density?

Kils (1981) investigated the swimming behavior and energetics of Antarctic krill and showed that its unique swimming system was finely tuned to counterbalance its excess weight. An Antarctic krill swims by metachronally beating its five pairs of pleopods in a back-to-front pattern. Each biramous pleopod spreads its two segments (the endopodite and exopodite) to drag flow backwards during its power stroke and contracts and folds the distal leg segments to minimize its surface area during the recovery stroke. Flow is

thus propelled posterior to the animal. Murphy et al. (2011) found the three following distinct swimming gaits for Antarctic krill based on swimming speed and body angle: hovering, fast forward swimming, and, more uncommonly, upside down swimming. During hovering, the krill's body angle relative to the surface is in the range of 25-50°. The water propelled posterior to the animal is thus pushed downward in a jet-like flow to provide weight support. As the krill's body rotates to a more horizontal position during forward swimming, the flow generated by the pleopods also becomes more horizontal and propels the animal forward (Kils, 1981; Murphy et al., 2011). Kils (1981) experimentally showed that hydrodynamic lift generated around the body itself provided enough upward vertical force to support the krill during fast forward swimming. During hovering, however, all weight support must be provided by the downward flow produced by the metachronally beating pleopods. Understanding the hydrodynamics of this unique behavior thus can provide insight into Antarctic krill energetics.

Furthermore, the hydrodynamics of propulsion via a traveling wave of appendages is interesting from a fluid physics standpoint. The forces and flows induced by a single paddling appendage (or appendage model) have been studied theoretically and experimentally in the low to intermediate Reynolds number (*Re*) regime characteristic of many drag-based swimmers (Walker and Westneat, 2000; Walker, 2000; Kim and Gharib, 2011; DeVoria and Ringuette, 2012). In particular, recent experimental work with rotating flat plates has shown that (depending on *Re*) vortices forming around the plate may also play a role in thrust generation (Kim and Gharib, 2011; DeVoria and Ringuette, 2012). The hydrodynamic effect of multiple appendages paddling in series, however, has not been experimentally studied in the same way (with physical models)

and is much less well understood. In the biological realm, several investigations have provided some insight into this type of flow, although most have focused on investigating the jet-like flow found in the animal's wake rather than on the flow around the appendages (Yen et al., 2003; Lim and DeMont, 2009; Catton et al., 2011). One exception is the study of lobster pleopod beating (in a mechanically actuated lobster exoskeleton) by Lim and DeMont (2009) in which they also examined flow generated by the pleopods. Lobsters, however, are a benthic species, and these flows were influenced by the bottom boundary. Other confounding factors in previous studies of metachronally produced flow have been animal tethering (which affects the flow by artificially reducing the animal's advance ratio to zero), insufficient spatial or temporal resolution, differences in animal swimming modes (hovering vs. forward swimming), and two dimensional flow measurements.

The purpose of the current chapter is to examine how hovering in Antarctic krill is facilitated by the flow produced by a metachronal stroke pattern. Using a volumetric flow measurement system, both the flow around the pleopods and in the wake will be examined with high spatial and temporal resolution around free-swimming animals. Furthermore, flow measurements and induced power theory will be used to estimate the energy required for hovering in Antarctic krill. It is hypothesized that hovering is an efficient swimming technique.

5.2. Materials and Methods

5.2.1. Experiment Description

Antarctic krill (*Euphausia superba*) were collected at coordinates of 64.9° W -64.4° S on a January 30, 2012 austral summer cruise conducted as part of the Palmer Antarctica Long-Term Ecological Research (PAL-LTER) program aboard the A.R.S.V *Laurence M. Gould.* Macrozooplankton were collected with a 2 × 2 m, square frame net with 700 µm mesh towed obliquely from the surface to a depth of 120 m. Once on board, the cod end contents were transferred to a large container of ambient surface seawater. Thirty krill were then moved to a 5 gallon bucket for transit back to Puntas Arenas, Chile from where they were shipped to Atlanta, GA for data collection. Water temperature during the week-long transit was recorded by a data logger and did not exceed 2.7° C. Because the shipment was detained for several days by U.S. Customs, only eight animals survived the trip. These krill appeared active and healthy on arrival and ranged in length from approximately 20 mm to 43 mm (eyeball tip to end of telson). Once in Atlanta, the surviving krill were kept in buckets of artificial seawater (salinity of 35 ppt) in an environmental chamber set at 0.1° C and fed from a culture of *Tetraselmis* phytoplankton.

Tomographic PIV flow measurements of free-swimming animals were conducted over a period of one week. To begin the experiment, six to eight animals were transferred from the environmental chamber to an aquarium of chilled seawater in a laboratory at room temperature. The hexagonal aquarium measured 15 cm to a side, with a height of 50 cm (approximately 29 l), and was covered with foam insulation to slow the temperature

increase of the water. Rectangular cutouts in the foam on two sides of the aquarium provided optical access for the four cameras, and cutouts on two additional sides allowed laser access. Water temperature and salinity were carefully monitored during the 2 to 3 hour long experiments and were controlled by the addition of seawater ice cubes (which increased the water salinity as they melted) and chilled freshwater (added to maintain the water salinity). The aquarium was occasionally gently stirred to maintain uniform conditions throughout. When necessitated by high ambient humidity, condensation on the aquarium surface was prevented by blowing air on the optical surface of the tank with hairdryers. The flow was seeded with 50 μm diameter glass sphere particles. Animals were returned to the environmental chamber upon completion of that day's experiments.

Free swimming krill were filmed at 400 fps with a tomographic PIV system (Murphy et al., 2012), shown in Figure 5.1, consisting of four high-speed Phantom v210 cameras (Vision Research, Wayne, NJ). Each camera was equipped with a 105 mm focal length Micro Nikkor lens (Nikon, Tokyo) and a Scheimpflug mount to correct for off-axis viewing distortion (which was lessened by having a fairly perpendicular view through the walls of the hexagonal aquarium). Cameras were mounted on optical rails and positioned by three-axis gear heads (Manfrotto, Cassola, Italy) to view a region (approximately 80 mm wide × 50 mm tall) in the center of the aquarium.

The volume of interest was illuminated by two continuous wave 7 W lasers (CrystaLaser, Reno, NV) operating with a near-infrared (IR) wavelength (808 nm). The krill did not appear to react to this wavelength of light. As shown in Figure 5.1, the two lasers were situated co-linearly on opposite sides of the aquarium in order to prevent shadowing of the particles by the presence of the animal. For each laser, the beam was expanded and

collimated using spherical plano-concave and biconvex lenses, and an adjustable aperture was used to create a beam with a rectangular cross-section of approximately 50 ×16 mm (height × width).The beam "width" defines the depth of the illuminated interrogation volume from the view of the four cameras. The positive *z*-axis was defined as pointing towards the four cameras, with the *x*- and *y*-axes defined as horizontal and vertical, respectively, in the imaged plane.

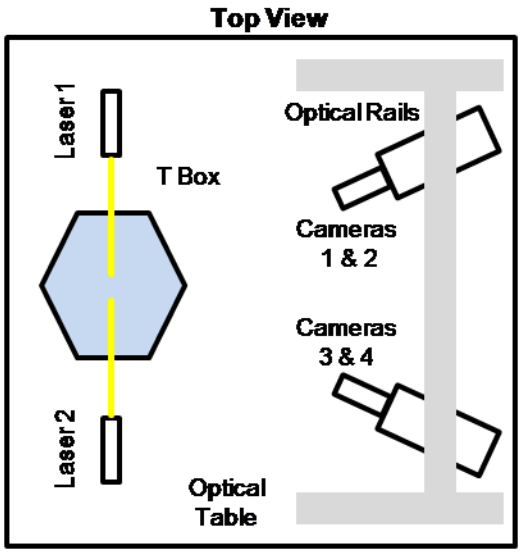

Figure 5.1 Diagram of the tomographic PIV system set up with a hexagonal tank to acquire flow field data surrounding Antarctic krill.

Data collection was manually triggered when an animal swam into the field of view of the cameras. Image acquisition was controlled through DaVis software (LaVision, Ypsilanti, MI) on a laptop PC and was synchronized by a high-speed controller that generates timing signals for the four cameras.

5.2.2. Data Analysis

One extended data sequence taken at 400 fps was chosen for analysis and was broken up into two sequences for separate processing and analysis. In this sequence, an Antarctic krill (length of 43 mm) enters the field of view from below (facing away from the four cameras) and swims upward through the field of view. Figure 5.2 shows simultaneous still images from all four cameras. The krill moves vertically and horizontally away from the cameras. It thus passes through the laser volume until only its posterior is still illuminated. The first data sequence (151 frames or 0.3775 s) comprised one complete stroke cycle (beginning with power stroke initiation by the fifth pleopod) and was extracted in order to investigate the flow around the pleopods. The second data sequence (360 frames or 0.9 s) began 200 ms later; it began during the middle of the fourth pleopod's power stroke and lasted slightly less than three stroke cycles. The krill had moved up since the first data sequence, and so the focus of this second sequence was the jet-like wake produced beneath the krill. Since the krill moved diagonally upward and away from the cameras during the second sequence, part of the jet exited the illuminated volume midway through this sequence.

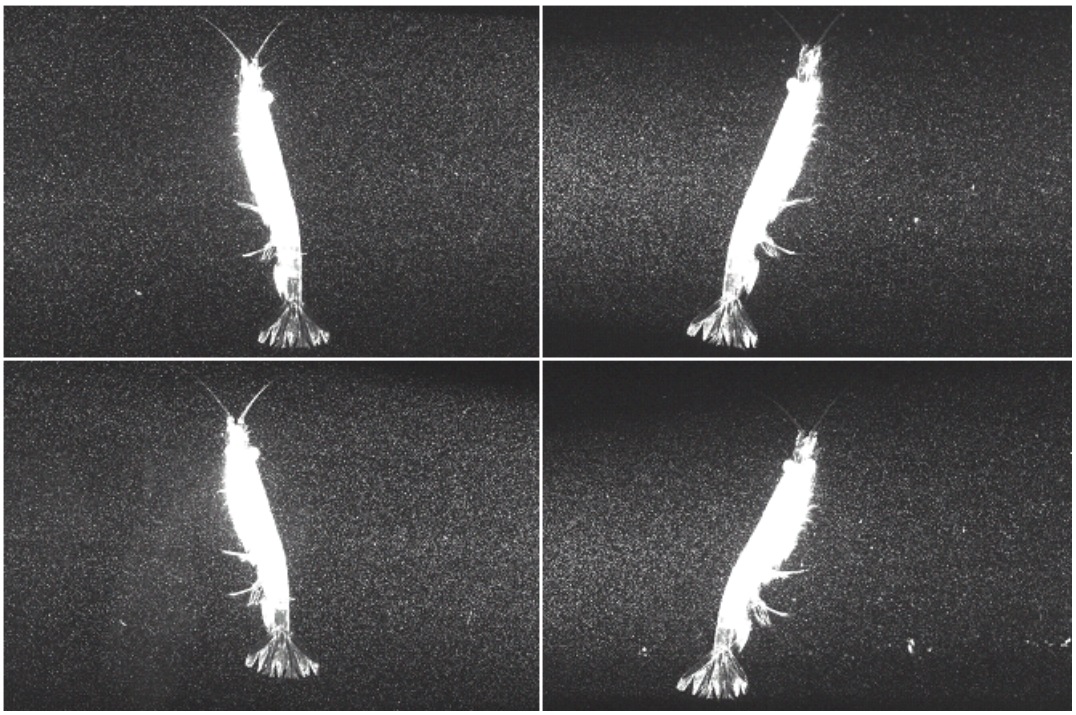

Figure 5.2 Example of four simultaneous still images of Antarctic krill analyzed in this study.

Because the two sequences were focused on different aspects of the flow, certain details of their processing were different. In both cases, images were pre-processed using a sliding minimum subtraction over 3 × 3 pixels, normalization with local average over 100 × 100 pixels, Gaussian smoothing, and subsequent sharpening of particles. For the first sequence, images were also processed via subtraction of a constant to eliminate noise, and multiplication by a factor of 10 to increase the dynamic range. Volume self-calibration was iteratively performed to correct for errors in the calibration (Wieneke 2008). Images were reconstructed into a light intensity volume by the MART algorithm in DaVis. In the first sequence a volume (measuring 46 × 54 × 19.5 mm) was

reconstructed. The animal body filled a portion of this volume. In order to reduce the effects of the reconstructed animal on the volume cross-correlations, the krill was masked before cross-correlation by manually tracing its outline in each of the four simultaneous images and creating a visual hull mask using the Multiplicative Lineof Sight (MLOS) scheme (Adhikari and Longmire 2012; Murphy et al. 2012). An attempt was made to automate this task using a median filter, but the very fine setae on the pleopods were unevenly illuminated and produced mediocre results. In order to understand the flow around the pleopods, the positions and extent of the appendages themselves had to be known with high certainty. Example visual hulls are shown in Figure 5.3. Because of the animal position, the volume frontal to the krill telson was in the “shadow” of the visual hull and therefore was unavailable for velocity measurements.

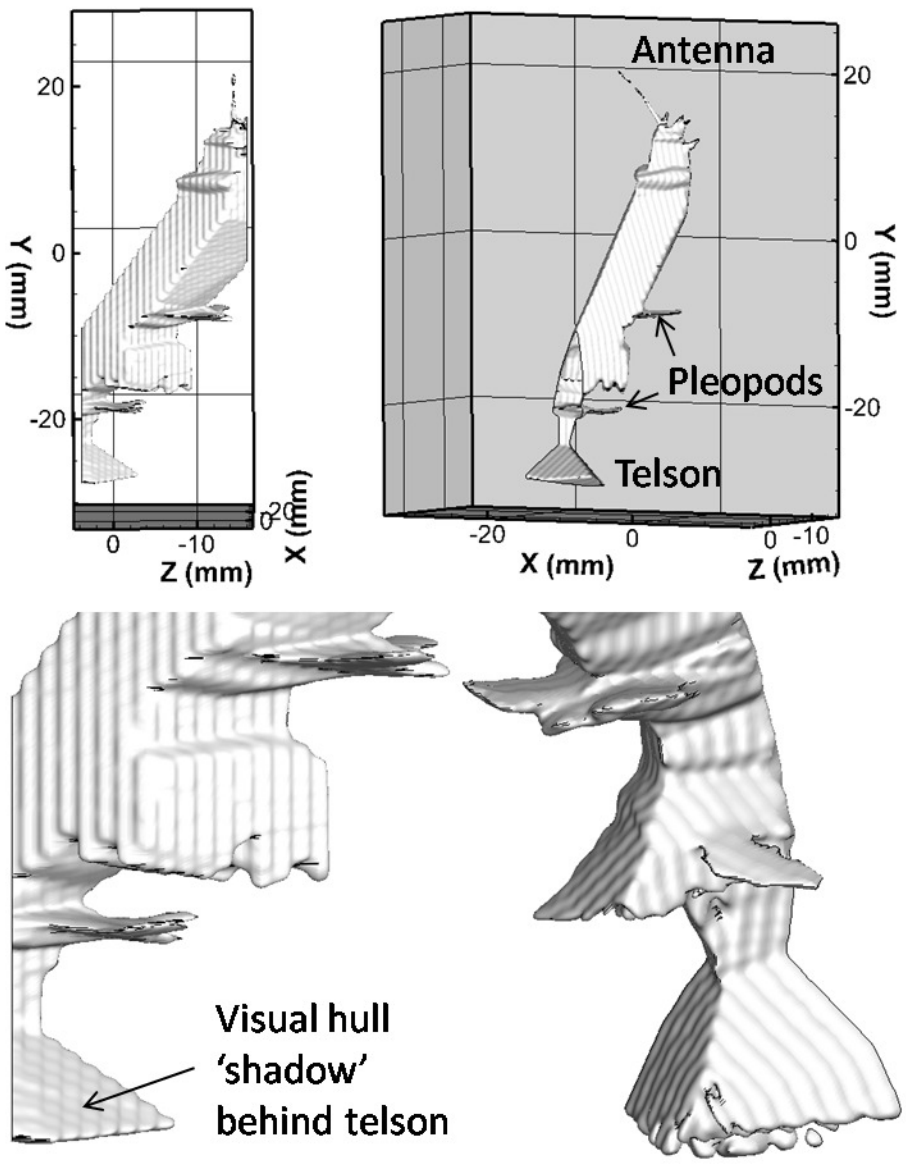

Figure 5.3 Examples of the visual hull created to represent the hovering Antarctic krill. The visual hull method captures the fine details such as the curvature of the pleopods and location of the antennae.

In the second sequence only the volume beneath the krill was reconstructed (which did not include the animal itself). The maximum vertical position of the reconstruction was increased at eight discrete steps throughout the time series (approximately every 50

frames) in order to capture flow directly beneath the upward-moving telson. The reconstructed volume began with a dimension in the *y*-direction of 8 mm and ended with a dimension of 16 mm. In order to place the flow in relation to the krill above it, a visual hull of the hovering animal was reconstructed as well. After performing image processing (normalize with local average over 200 × 200 pixels and Gaussian smoothing of 3 × 3 pixels) to increase the contrast around the animal's border, the background around the animal was algorithmically masked out with a threshold after using a 7 × 7 median filter to smooth out the PIV particles. The resulting silhouettes were reconstructed into visual hulls for each of the 491 time points using the MLOS algorithm in DaVis.

In both sequences, consecutive light intensity volumes (i.e. volumes containing particles) were cross-correlated with a window size decreasing down to 32 cubic pixels and an overlap of 75%. The resulting vector field had vector spacing of approximately 0.5 mm. In the first sequence, the universal outlier detection scheme (with a remove threshold of 2) was applied to remove and replace spurious vectors (Westerweel and Scarano 2005). The resulting velocity field was smoothed in space with a 3 × 3 × 3 Gaussian filter and smoothed over time with a 5 frame Gaussian filter. In the second sequence, the universal outlier detection technique was applied, and the vector volume was smoothed with a 3 × 3 × 3 spatial filter of the same strength (0.05) as in Murphy et al. (2012) before being smoothed again with a 3 × 3 × 3 Gaussian filter in space and a 5 frame Gaussian filter in time.

The second sequence was used to estimate the error associated with the tomographic PIV measurements, particularly the calculation of viscous dissipation rate described in the Discussion. As noted by Scarano and Poelma (2009), the precision can be estimated

based on physical criteria. Specifically, conservation of mass and incompressibility of flow can be used in the calculation of flow divergence to estimate errors on the spatial derivatives. For incompressible fluid, the divergence of the volumetric flow field ought to equal zero at every point and was denoted *D*:

$$D = \nabla \cdot \vec{V} = \frac{\partial u}{\partial x} + \frac{\partial v}{\partial y} + \frac{\partial w}{\partial z}$$

The standard deviation of *D* is then a statistical estimate of the measurement precision for spatial gradients. The divergence of the vector volume was calculated in DaVis via central differencing at each time point in a sub-volume of the domain. A time average was then produced and exported to Matlab where the standard deviation of *D* was calculated to be 0.44 s^{-1}. The value can be normalized by dividing by typical vorticity magnitude values found inside the jet (5 – 15 s^{-1}), giving a relative error of 2.9 - 8.8%, which is similar to the uncertainty values reported in Scarano and Poelma (2009).

5.3. Actuator Disk Theory

Hovering is a unique behavior since the underwater weight of the negatively buoyant animal is entirely balanced by the rate at which it transfers momentum downward through the beating of its pleopods. This equivalence allows the application of actuator disc theory in order to estimate the induced power necessary to support hovering (Blake, 1979; Alexander, 2003). This theory, originally applied to helicopters (Johnson, 1994), has previously been applied to hovering in flying insect and bird species (e.g.

Pennycuick, 1968; Ellington, 1978; Rayner, 1979) and to a benthic fish (e.g. Blake, 1979) but never before to a hovering pelagic animal such as a krill.

An actuator disc may be considered an idealized device that causes a sudden increase in pressure in a stream of fluid passing through it. For the purpose of krill hovering, the pleopods function as five pairs of actuator discs. Integrating this pressure rise over the total pleopod area A then gives the upward thrust force T necessary for the animal to support its underwater weight W_U. Far upstream of the pleopod actuator disc, the velocity is zero and the pressure is p_0. The water passes through the actuator disc at some increased velocity v_{ind}. On the upper side of the actuator disc, the pressure falls to p_1 because of increased velocity compared to the far upstream position (Bernoulli's principle). On the bottom side of the disc, pressure increases to p_2 because of the action of the actuator disc. In the wake far beneath the animal, the velocity becomes v_w while the pressure returns to p_0. Hydrostatic effects due to elevation changes are considered negligible.

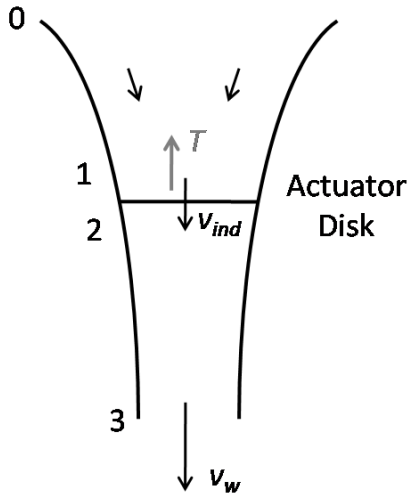

Figure 5.4 Diagram of relevant quantities in actuator disk theory

Bernoulli's equation can then be applied between a location far above the animal ($p = p_0$ and $v = 0$) and the top of the actuator disc ($p = p_1$ and $v = v_{ind}$), resulting in

$$p_0 - p_1 = \tfrac{1}{2}\rho v_{ind}^2. \qquad (1)$$

Applying Bernoulli's equation from just below the actuator disc ($p = p_2$ and $v = v_{ind}$) to a location in the wake far beneath the animal ($p = p_0$ and $v = v_w$) results in

$$p_2 - p_0 = \tfrac{1}{2}\rho(v_w^2 - v_{ind}^2). \qquad (2)$$

Adding equations (1) and (2) gives

$$p_2 - p_1 = \tfrac{1}{2}\rho v_w^2. \qquad (3)$$

The difference in pressure between p_1 and p_2 acts across the area of the pleopods A to support the underwater weight of the animal W_U, which is equal to the thrust T, as seen here:

$$T = W_U = \tfrac{1}{2}\rho A v_w^2. \qquad (4)$$

The rate of mass flow through the actuator disc is then $\rho A v_{ind}$. The rate at which vertical momentum is transferred to the water is the product of the mass flow rate and the vertical velocity component, which must equal the animal's underwater weight, is then

$$W_U = \rho A v_{ind} v_w. \qquad (5)$$

Equating (4) and (5) for underwater weight W_U shows that

$$v_w = 2v_{ind}. \qquad (6)$$

Furthermore, the induced power P_{ind}, the rate at which kinetic energy is added to the water, is

$$P_{ind} = \tfrac{1}{2}\rho A v_{ind} v_w^2. \qquad (7)$$

Substituting (6) into (5) and solving for v_{ind} yields

$$v_{ind} = \sqrt{\frac{W_U}{2\rho A}}. \qquad (8)$$

Substituting (6) and (8) into (7) yields an expression for induced power in terms of the animal's underwater weight, pleopod area, and water density

$$P_{ind} = 2\rho A v_{ind}^3 = \sqrt{\frac{W_U^3}{2\rho A}}. \qquad (9)$$

The pleopod area of the hovering krill considered here could not be measured directly from any of the four images from the tomographic PIV system. Instead, the pleopod area was based on morphological measurements of the five endopodites for the same-sized animal (43 mm in length) from Murphy et al. (2011) and on kinematics measurements of the current data set. As shown in Figure 5.5, the area of each pleopod was modeled as a circular sector where the radius is the measured endopodite length. The arc angle is the maximum angle between the endopodite and exopodite during the power stroke (γ = 53°) as measured on the krill visual hull reconstruction. This model does not include the protopodite area because its effect on the flow dragged down during the stroke is likely minimal. Endopodite lengths and modeled pleopod areas for pleopods one through five are shown in Table 5.1. The total pleopod area (i.e., the sum of the areas of the five individual pleopods) was approximately 130 mm^2.

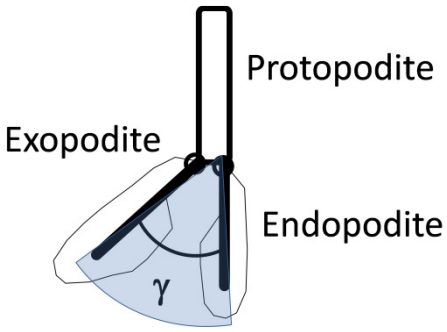

Figure 5.5 Diagram of pleopod and modeled pleopod area.

Table 5.1 Endopodite lengths (Murphy et al. 2011) and modeled areas (for both pleopods in a pair) for a 43 mm krill.

	P5	**P4**	**P3**	**P2**	**P1**
Endopodite Length (mm)	3.5	4.0	3.8	4.0	3.5
Pleopod Area (mm^2)	23	30	27	30	23

Based on a regression analysis, Kils (1981) provided the following expression for the underwater "weight" W_U (actually the mass including buoyancy effects) of

$$W_U = 1.73 \times 10^{-8} L^{3.67}$$

where W_U is in grams and L is in millimeters. For the 43 mm krill considered here, the true underwater weight is then 1.67×10^{-4} N. The induced power, assuming a seawater density of 1026.4 kg m^{-3}, is then 4.16×10^{-6} W. Dividing by the underwater weight of the krill gives a specific induced power of 0.025 W N^{-1}.

5.4. Results

5.4.1 Krill Kinematics

One of the difficulties of analyzing the flow produced by the krill is that its body is moving three dimensionally over time. In order to provide some reference point, the central tip of the reconstructed telson (tail) was tracked in the second data sequence at 0.05 s intervals. The time points at which pleopod power strokes began and ended were also noted. Figure 5.6 shows the krill speed as function of time in relation to the power stroke periods of the individual pleopods. Only the first two periods are shown because the pleopods exited the light volume with increasing time. Pleopod one could not be seen in all of the PIV images and hence was not included in the figure.

The krill translates upwards and away from the cameras (in the negative z-direction) at a mean speed of 13 mm s^{-1}. With a body length of 43 mm, the krill is moving at a normalized speed of approximately 0.25 body lengths per second. This value, along with the inclined body angle (50°), places the displayed swimming behavior within the hovering swimming gait identified by Murphy et al. (2011). Periodic increases in krill speed (notable at times of 0.2 and 0.6 s in Figure 5.6)seem to correspond to the onset of the third pleopod stroke. The middle pleopods usually are longer and thus more powerful than the outer pleopods such as P1 and P5. This trend has also been observed in metachronally stroking remipedes (Kohlhage and Yager, 1994).

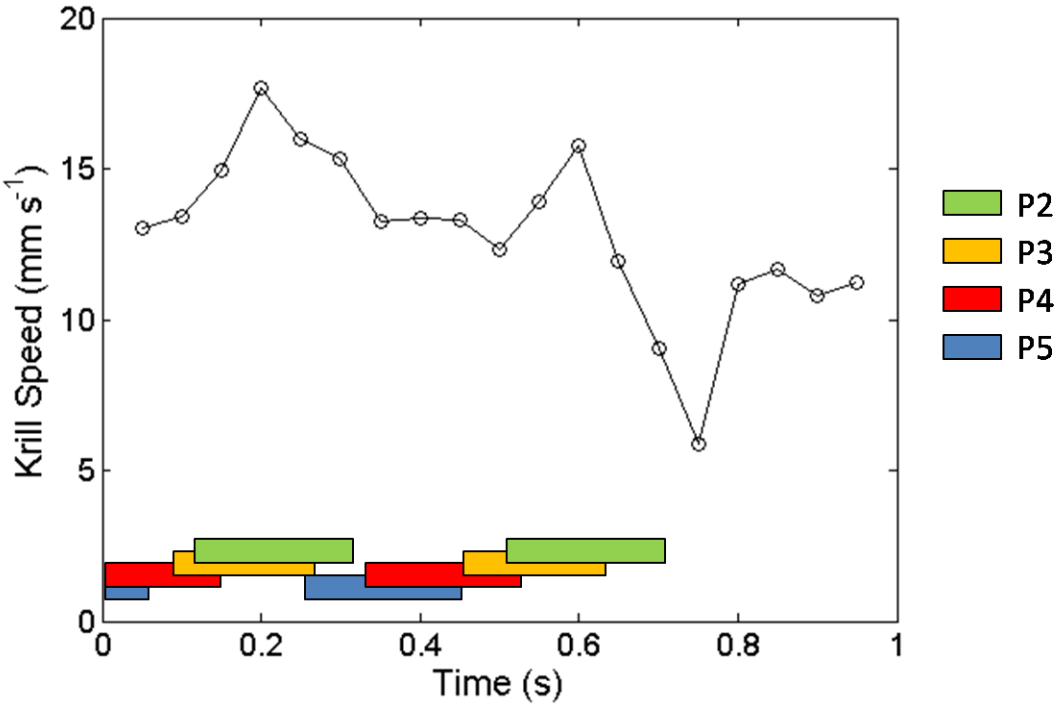

Figure 5.6 Krill speed as a function of time. The time period of the first two power strokes of pleopods two through five are shown as colored bars.

5.4.2 Flow Fields Surrounding Moving Pleopod

The flow field around a single, stroking pleopod will first be presented and examined based on the first data sequence. Figure 5.7shows a series of flow fields in the medial plane of the krill throughout the power stroke of pleopod four in 30 ms intervals. In the first panel (t = 0.1 s), the fifth pleopod has just completed its power stroke, and the flow created by its motion is directed downward, following the path of pleopod five, at speeds up to 30 mm s^{-1}. Pleopod four therefore is beginning its power stroke into fluid that is already being convected downward. In the second panel (t = 0.13 s), flow with speeds up to 24 mm $s^{-1}$is present in the wake of pleopod four, the tip speed of which is

approximately 50 mm s^{-1}. Also evident in this frame is upward curvature of the exopodite in response to resistive fluid forces. The endopodite apparently is more rigid and does not exhibit as much bending. The flow dragged behind the fifth pleopod continues to strengthen as that pleopod is pulled towards the body in the beginning of its recovery stroke. The flow generated by pleopod four continues to strengthen in the third panel (t = 0.16 s), with peak speeds of 35 mm s^{-1}. By the fourth panel (t = 0.19 s), pleopod four nears the completion of its power stroke. The volume of moving fluid has greatly increased by this time point, and peak speeds of up to 40 mm s^{-1} are present.

For comparison, flow at the power stroke completion of the more powerful third pleopod (t = 0.305 s) is shown in Figure 5.8. The vertical position of the krill visual hull has noticeably increased by this time point (as evidenced by the space beneath the telson), and peak flow speeds of up to 46 mm s^{-1} are present. It is also particularly evident in Figure 5.8 how the visual hull shadow prevents flow measurement in front of the telson. It is in this region that the individual flow pulses created by each pleopod are expected to join together in the cyclical jet measured beneath the krill in the second data sequence. Vectors near the visual hull boundary may also be contaminated if the volume masking fails to remove all vestiges of the reconstructed animal body.

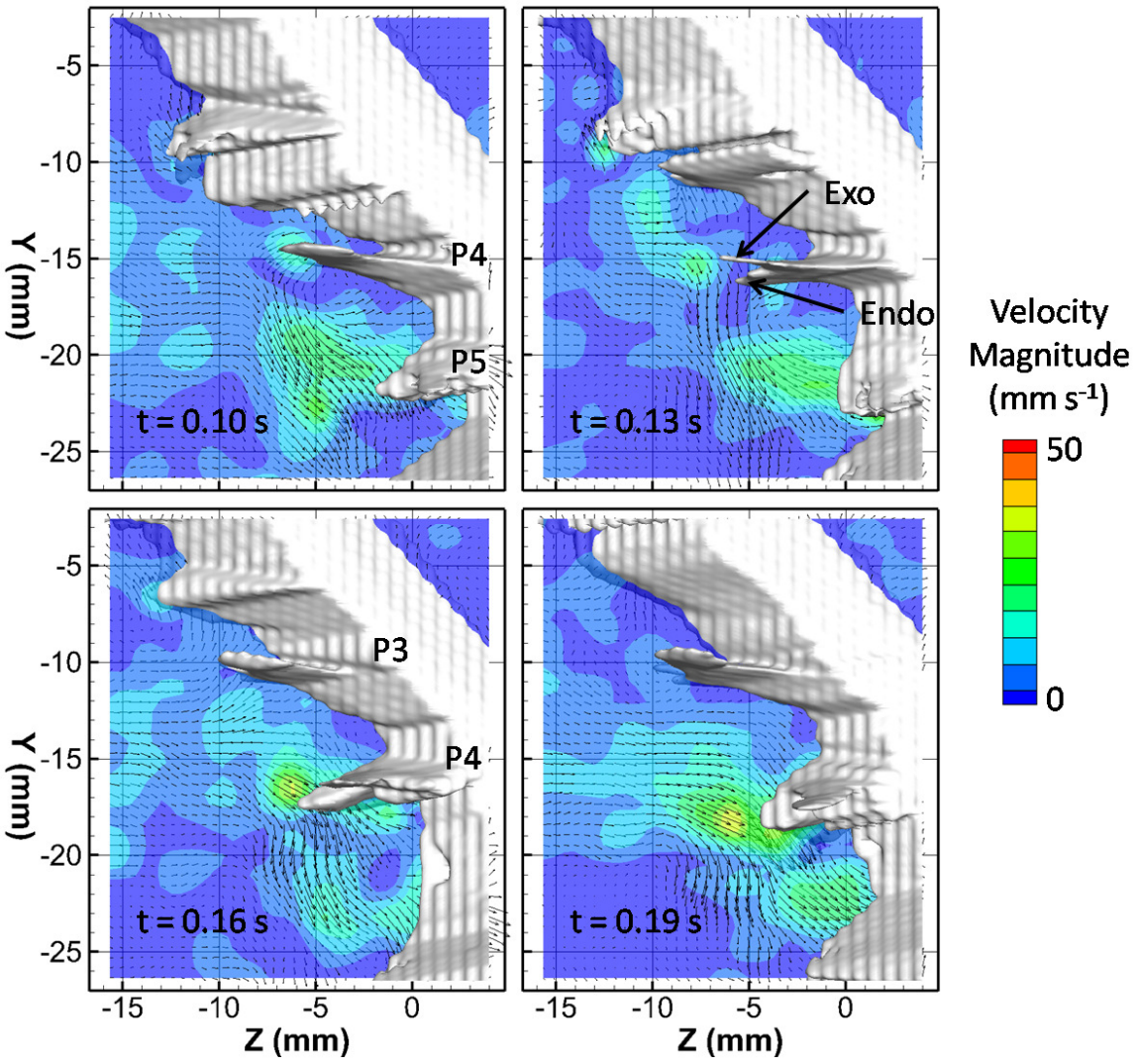

Figure 5.7 Flow fields in the krill medial plane at different times throughout the power stroke of pleopod four. Contour colors represent velocity magnitude while arrows additionally represent flow direction. Pleopods four and five (P4 and P5) and pleopods three and four (P3 and P4) are labeled in the first and third panels, respectively. The exopodite (Exo) and endopodite (Endo) are labeled in the second panel.

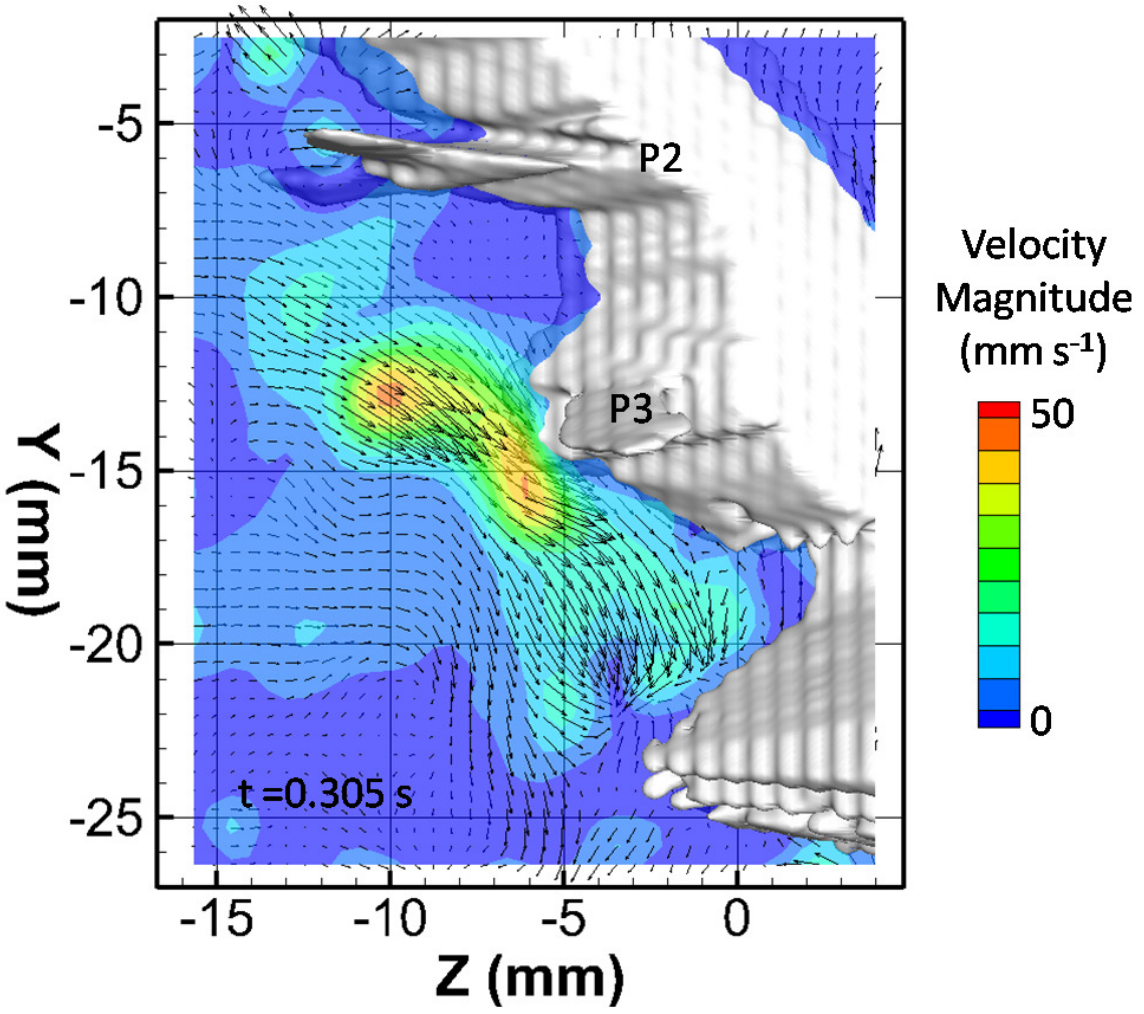

Figure 5.8 Flow field in the krill medial plane at one time near the completion of the power stroke of pleopod three. Contour colors represent velocity magnitude, while arrows additionally represent flow direction (in the plane). Pleopods two and three (P2 and P3) are labeled.

Figure 5.9 shows the flow field in a *z*-plane distal to the tip of the fourth pleopod at a time point of $t = 0.1925$ s and provides information on the lateral extent of the flow generated by the sweeping pleopods. The width of the high speed flow region approximately matches that of the extended pleopods. Furthermore, the edges of the flow have an inward (medial) component that likely is caused by pleopod cupping as the exopodites

are drawn medially during the latter part of the power stroke. This cupping is evident in the fifth pleopod pair in the volumetric reconstruction of the Antarctic krill in Figure 5.3 (lower right panel). Cupping is also seen in the pectoral and caudal fins of fishes, and cupping in a robotic caudal fin fish model was found to produce greater thrust than other profiles (Lauder and Madden, 2007; Esposito et al., 2012). Furthermore, as the exopodites are drawn together at the end of the power stroke, they may squeeze fluid downward in a jet. This volume was not accessible during the current experiments due to the shadow of the visual hull.

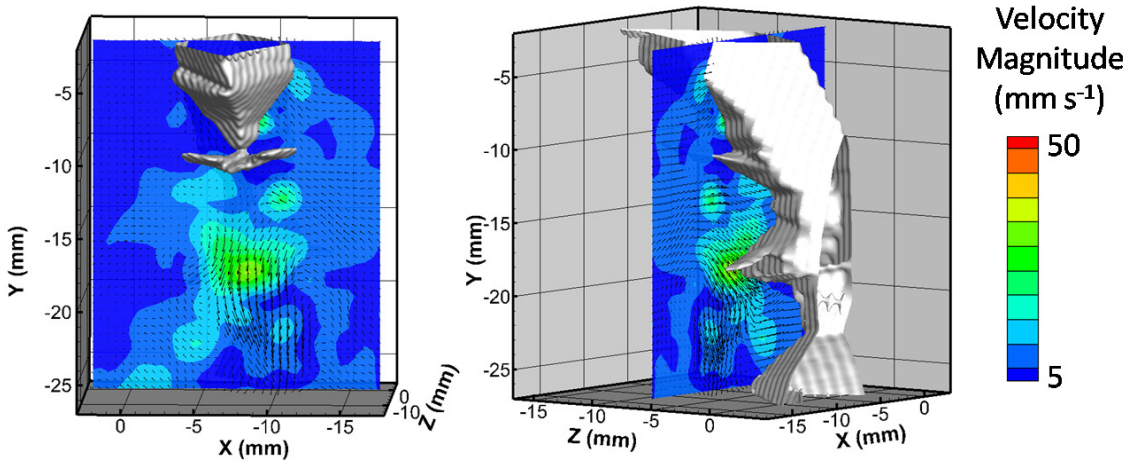

Figure 5.9 Flow field in a z-plane at t = 0.1925 s viewed from two different perspectives. Contour colors represent velocity magnitude while arrows additionally represent flow direction.

Figure 5.10 shows a plot of the vorticity during the middle of the power stroke of pleopod four (t = 0.1975 s) where color contours represent the z-component of vorticity. The downward sweep of both pleopod exopodites seems to have induced the formation of vortices (marked by heavy black arrows). Visible in the raw PIV images, the downward

motion of the pleopod pushes fluid in front of and to the side of the pleopod (i.e, away from krill body). The fluid pushed to the side is then entrained in the wake of the pleopod as it moves past.

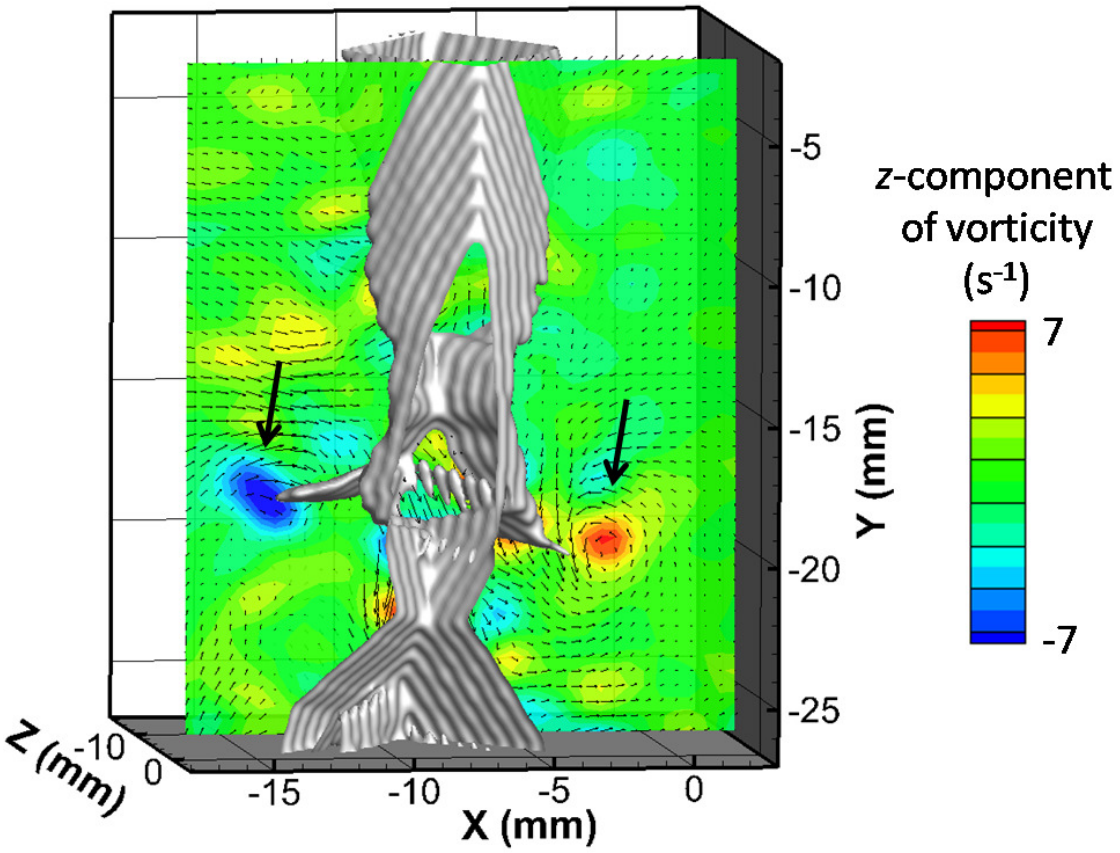

Figure 5.10 Flow field in the *z*-plane at $t = 0.1975$ s representing a pleopod-induced vortex. Contour colors represent the *z*-component of vorticity while arrows represent the velocity vector. The location of the vortex is marked by a heavy black arrow.

5.4.3 Jet Flow

The second data sequence was processed to examine the jet-like flow beneath the animal. Figure 5.11 reveals the volume the jet occupies beneath the krill using an iso-contour to connect points in the volume with the same velocity magnitude of 30 mm s^{-1}, and a heavy black arrow marks the posterior tip of the telson. Figure 5.12 shows flow in the krill's medial plane. The velocity vectors generally are angled down and backwards at about 15° from the vertical, which explains why the krill is drifting forward slightly over time. The influence of the telson in directing the flow can also been seen. The telson tip (which projects downward at z = 0 mm) provides a posterior edge to guide the jet and also is marked by a heavy black arrow.

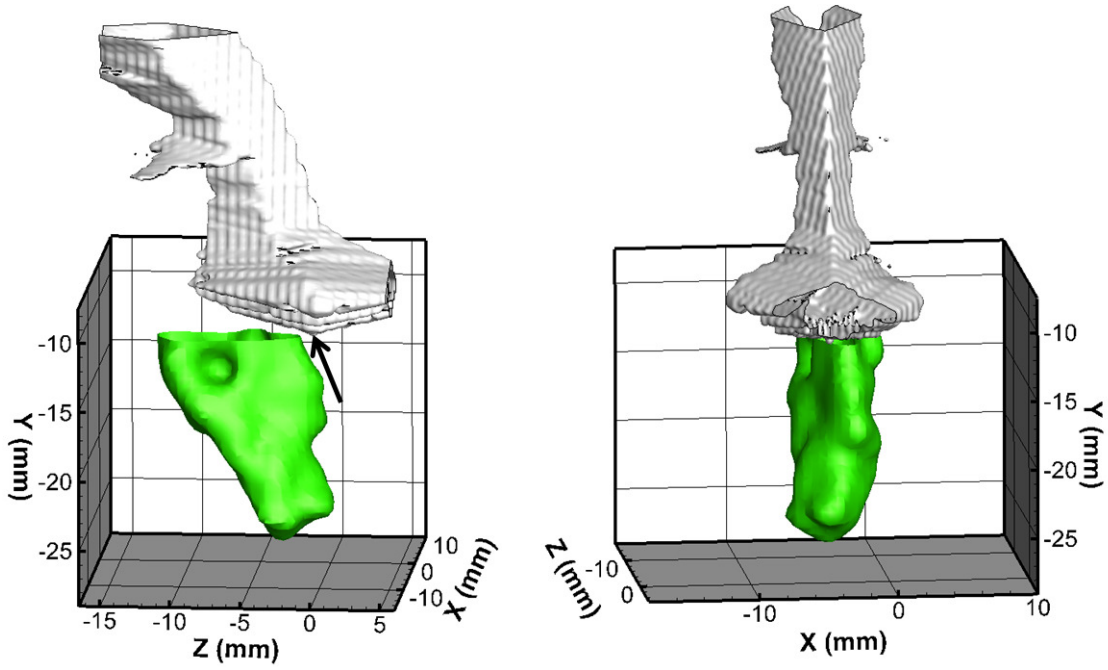

Figure 5.11 The three-dimensional iso-surface shown beneath the krill connects points in space that have a velocity magnitude of 30mm s^{-1}. The telson tip is marked by a heavy black arrow.

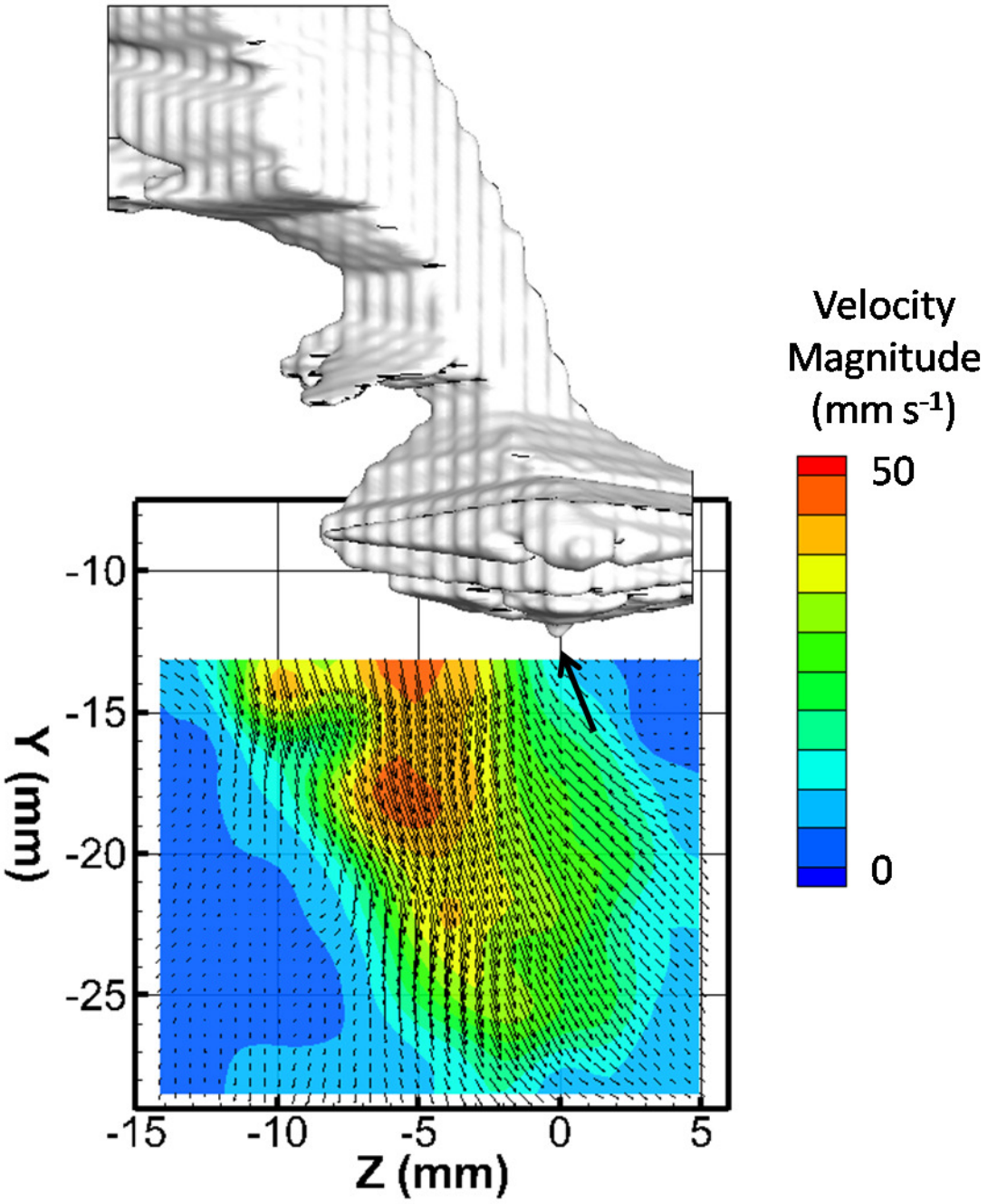

Figure 5.12 Flow field in wake of hovering Antarctic krill. Color contours indicate velocity magnitude while vectors additionally indicate flow direction (in the plane). The telson tip is marked by a heavy black arrow.

In order to analyze the development of the wake over time and space, two *y*-planes at different distances beneath the animal were examined in more detail. The proximal plane was positioned 2 mm below the tip of the telson while the distal plane was located 10 mm beneath the proximal plane. The positions of these planes relative to the krill reconstruction are shown in Figure 5.13 (at time $t = 0.4$ s; note that the time scale of the second data sequence does not correspond to that of the first). Because the krill moves vertically with time, the *y*-location of each plane was different at each time point and was based on tracking of the telson tip. Horizontal movement of the krill precluded selection of a single point from which to extract relevant velocity data. The maximum velocity magnitude in each extracted (horizontal) plane therefore was chosen as a representative velocity value.

Figure 5.14 shows the time record of the maximum velocity magnitude for the proximal and distal planes beneath the hovering krill. At 2 mm beneath the telson tip, proximal flows cyclically range from 35 mm s^{-1} up to 55 mm s^{-1}. The time separation between subsequent flow peaks at 0.3475 s and 0.7025 s reflects a frequency of 2.82 Hz, which matches the frequency of the pleopods found from observing the krill kinematics in the PIV images. At 12 mm beneath the telson tip, distal flows range from approximately 20 mm s^{-1} up to 50 mm s^{-1} and the periodicity is phase-shifted relative to the proximal flow (representing the 10mm separation between the two planes).

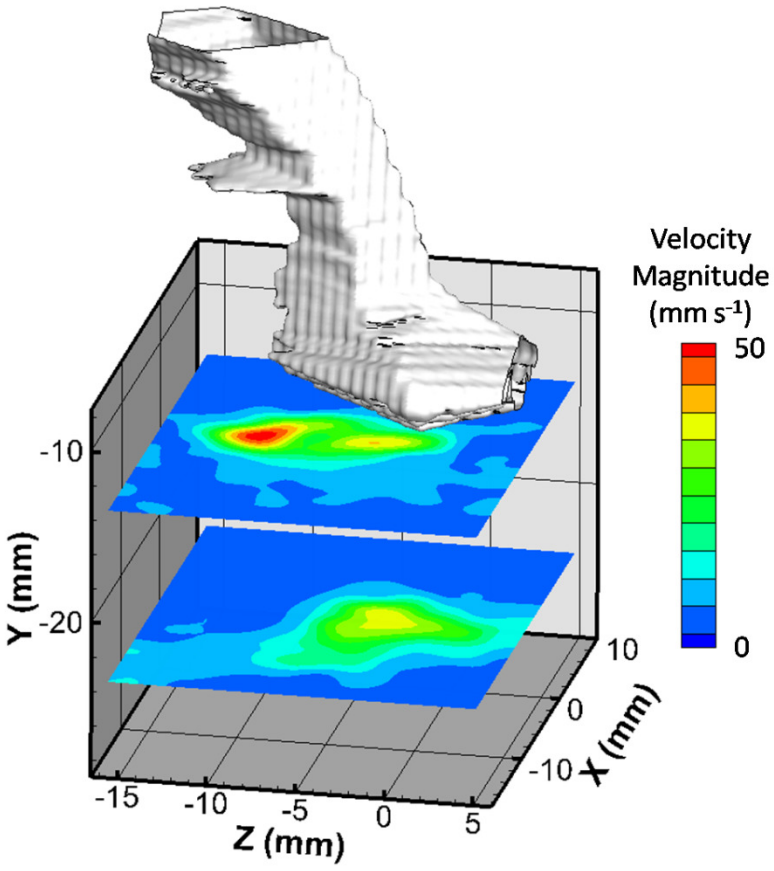

Figure 5.13 Two planes (proximal at 2 mm below telson; distal at 12 mm below telson) showing velocity magnitude in wake of hovering krill, thereby demonstrating the vertical positions of the extracted planes relative to the krill body.

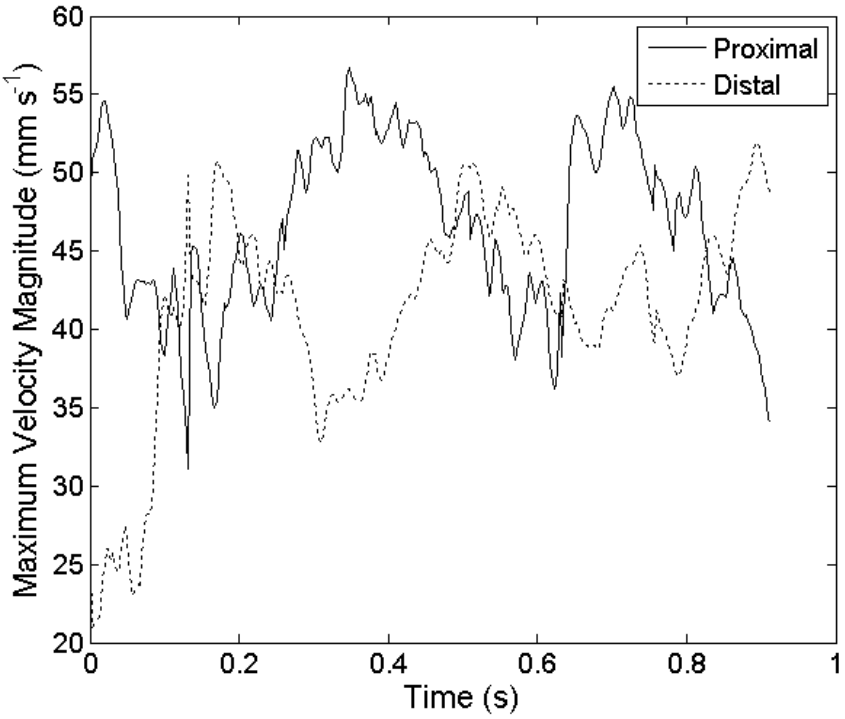

Figure 5.14 Maximum velocity magnitude as a function of time in proximal and distal planes 2 and 12 mm beneath the krill, respectively (as shown in Figure 5.13).

5.5. Discussion

5.5.1 Pleopod Flow

The flow generated by a stroking appendage in low Reynolds number drag-based propulsion has not previously been measured with the current level of temporal or spatial resolution. One of the most interesting flow features revealed by this resolution is the formation of tip vortices on the pleopods, a feature previously only seen in scaled appendage models (Kim and Gharib, 2011). Vortex formation is important in this context because the rate of change of vortex circulation and area enclosed by the vortex are

related to thrust generation (Kim and Gharib, 2011). Using a defocusing PIV system (similar to the tomographic PIV system used in this chapter) to acquire phase-averaged volumetric flow data, Kim and Gharib (2011) investigated the formation of vortices on rotating plates (meant to mimic a drag-based power stroke) at Reynolds numbers of 140 and 19,720 (calculated using the tip speed and paddle length). Based on a pleopod length of 6.5 mm and an exopodite tip speed of 95 mm s^{-1}, the Reynolds number of the flow under study here is approximately 340. Furthermore, the delta-shaped model used by Kim and Gharib (2011) closely resembles the euphausiid pleopod morphology when the exopodites are extended during the power stroke; their work with this paddle at the lower Reynolds number (140) therefore provides a nice point of comparison.

In the current work, vortices were associated with the lateral exopodites but not with the medial endopodites. Similarly, Kim and Gharib (2011) showed that the side vortices on their delta model were much larger than the tip vortex. The tip vortex was also shed from the paddle by flow down the paddle length. Another possible reason why the tip vortices were not present in the current work is that the medially-located endopodites were stroking into flow already set in motion by the previous pleopod. The difference in speed between the endopodite tip and the surrounding flow was therefore minimal. The exodpodites, in contrast, were stroking laterally into relatively still flow and therefore had a higher effective speed which was more conducive to vortex formation.

Several other similarities existed between the current work and that by Kim and Gharib (2011). They showed that the flow was dragged along perpendicular to the plate at low Reynolds numbers whereas it was forced along the length of the plate at high *Re*. In the current work, the flow behind the pleopods mostly remained perpendicular to the pleopod

surface, as seen in Figure 5.7. They also found that flexible plates produced greater thrust than rigid plates. As evidenced by the bending exopodites in Figure 5.7, the pleopods exhibit flexibility, too. One difference is that krill pleopods are covered with fine setae which effectively increase its surface area while the plates used by Kim and Gharib (2011) are not. Since many animals operating in this low *Re* regime have hairy appendages (Wootton, 1999), it would be interesting to investigate the effect of a setae-covered surface (versus that of a rigid, clean surface) on the formation of vortices.

One issue that the current data set does not address is how the packets of flow induced by each pleopod coalesce into the jet beneath the krill. This occurrence happens frontal to the telson where flow information is not available. Furthermore, the maximum velocities measured around the pleopods (45 mm s^{-1}) are slightly less than those measured below the telson (55 mm s^{-1}). This pattern was also seen in PIV of a hovering *Euphausia pacifica* by Catton et al. (2011) in which the maximum velocity was not reached until several millimeters below the telson. High temporal resolution PIV of a krill viewed from the side would answer this question.

5.5.2 Jet Flow

Although jet propulsion is common among aquatic organisms, the jet flow produced by the hovering Antarctic krill in this study is different. Salps, squids, and hydromedusae produce pulsed jets through the compression of internal cavities (Anderson and Grosenbaugh, 2005; Dabiri et al., 2006; Sutherland and Madin, 2010). Because the animal must relax in order to draw more fluid into its cavity, the jet production cycle is

necessarily rhythmic, and jet production has often been associated with low swimming efficiency (Alexander, 2003). Vortex rings, which often form as a result of a pulsed jet, may be tuned, however, to increase locomotion efficiency (Dabiri et al., 2006).

The jet produced by a hovering Antarctic krill, in contrast, is not pulsed. Instead, it has an oscillatory component superimposed on a steady component. At a location just below the telson, the steady component is approximately 45 mm s^{-1} while the oscillatory component has a peak-to-trough magnitude of approximately 20 mm s^{-1} (Figure 5.14). Farther downstream, the both the steady and oscillatory components are smaller and are phase shifted relative to the upstream (Figure 5.14). This pattern is similar to that seen by Lim and DeMont (2009) for a mechanically-actuated lobster exoskeleton in which the flow at a distal station had a smaller magnitude and was phase-shifted relative to a proximal station. Directly posterior to the last pleopod, Lim and Demont (2009) recorded speeds cycling between approximately 175 mm s^{-1} and 60 mm s^{-1} during steady state beating. Posterior to the tail fan (63 mm downstream of the proximal plane), jet speeds, while still showing variations of approximately 25 mm s^{-1}, had stabilized to a value of about 100 mm s^{-1}.

A direct comparison between the krill and lobster is difficult because of differences in size. The lobster body is much larger than the krill (236 mm vs. 43 mm), and the pleopods of the lobster are longer as well (41 mm vs. 6.5 mm). The beat frequency of the hovering krill is more than twice of that of the lobster (2.8 Hz vs. 1.3 Hz). Lobster and krill pleopod beating may be compared through the Strouhal number *St*, a dimensionless number describing oscillating flow systems, particularly those involving vortex shedding (Triantafyllou et al. 1993).The Strouhal number is defined as

$$St = \frac{fL}{V}$$

where f is the frequency, L is a characteristic length, and V is a characteristic velocity. The Strouhal number is remarkably consistent, within a range of $0.2 < St < 0.4$, for a wide variety of swimming fish and cetaceans and flying birds, bats, and insects when swimming or flying at their 'cruising' or self-selected speed (Triantafyllou et al., 1993; Taylor et al., 2003; Rohr and Fish, 2004). Strouhal numbers within this range have been linked to high locomotion efficiency (Triantafyllou et al., 1993; Anderson et al., 1998). All of these species employ lift-based locomotion mechanisms (often involving leading or trailing edge vortices) as opposed to the drag-based technique used by Antarctic krill, and the Strouhal number of paddling organisms has not been investigated. As seen in this study, however, vortex formation may also play a role in krill paddling, and it may therefore be appropriate to apply the Strouhal number to metachronally paddling organisms. Application in the current case of krill hovering is not straightforward, however, since animal speed is usually taken as the characteristic velocity. Triantafyllou et al (1993) state that there are cases "such as hovering foils, where the only relevant velocity is the maximum jet velocity, which must then be used in the definition of *St*." Since the lobster in Lim and Demont (2009) is stationary and the hovering krill is nearly stationary, the characteristic velocity$V$ is taken to be the peak flow velocity immediately posterior to the tail (55 mm s^{-1} for the krill and 160 mm s^{-1} for the lobster). The characteristic length L is taken to be the average pleopod length (6.5 mm for the krill and 41 mm for the lobster), and the frequency f is the animal's beat frequency (2.8 Hz for the krill and 1.3 Hz for the lobster). The Strouhal numbers of both species then match at *St*=

0.33, thereby implying dynamic similarity. The fact that St is within the $0.2 < St < 0.4$ range also indicates that hovering in Antarctic krill may be quite efficient.

It is interesting to consider how the wake signature would change when the advance ratio was increased. The advance ratio, which is the ratio of the animal speed to the appendage tip speed, may be normalized for multi-appendage animals by dividing by the number of leg pairs (Ellington, 1978; Murphy et al., 2011). In the current experiment, the normalized advance ratio J_m for the hovering krill was small at 0.06. The flow beneath the krill has an oscillatory component imposed on a steady component. The flow generated by each pleopod seems to merge into a single, rhythmic stream. Antarctic krill, however, can swim at up to eight body lengths per second, giving a J_m of approximately 0.34. Considering each pleopod separately gives a (non-normalized) advance ratio of 1.7, meaning that, on average, the krill is moving forward at almost twice the speed that its propulsive appendages are sweeping backwards. As krill swim faster, they transition from hovering into a more horizontal posture and therefore push flow backwards instead of down. The pulses of the hovering jet would become more pronounced as the animal transitioned into slow forward swimming. Eventually, at high speeds, it might be expected that each pleopod would propel discrete packets of flow backwards. The packets may be spaced far enough part to not interact significantly with each other. The spacing and timing of these packets could form a significant part of the hydrodynamic signal by which schooling Antarctic krill sense conspecifics. Although flow measurements of Antarctic krill swimming at very high speeds have not yet been captured, Catton et al. (2011) recorded planar PIV measurements of krill swimming at speeds up to approximately 2.5 body lengths per second. At these speeds, the wake flow

no longer resembles a coherent jet but is somewhat fragmented, with separated pulses of flow corresponding to each pleopod stroke. At elevated swimming speeds, the effect of the body on the wake flow must also be considered, with the possibility of induced drift behind the krill interacting with the pleopod-produced flows.

The Strouhal number of the Antarctic krill will also change with increased swimming speed. At some increased swimming speed, the swimming speed will become a more relevant characteristic velocity than the maximum jet speed in the animal's wake. The Strouhal number was investigated in relation to normalized swimming speed by plotting Strouhal number calculated from both wake speed (St_{ws}) and swimming speed (St_{ss}) over a range of krill swimming speeds and beat frequencies. Animal swimming speeds, wake flow speeds, and corresponding beat frequencies were taken or estimated (for a 43 mm krill) from the current work, Kils (1981), Catton et al. (2011), and Murphy et al. (2011). Figure 5.15 shows that St_{ss} and St_{ws} intersect at approximately the normalized swimming speed at which the pleopod swimming stroke becomes fully developed; greater speeds are then achieved solely through increased beat frequency (Kils, 1981; Murphy et al., 2011). It thus seems appropriate to use St_{ws} for normalized speeds of less than two body lengths per second and St_{ss} for speeds greater than that. The Strouhal number for Antarctic krill swimming then lies within or very near the highly efficient $0.2 < St < 0.4$ range for the entire span of its swimming capabilities. This is highly unusual for an animal that must provide weight support over its entire range of swimming speeds. Taylor et al. (2003) showed that zebra finches forced to fly at speeds ($4 – 14$ m s^{-1}) outside of their chosen range exhibited Strouhal number ranging from approximately 0.25 to 1.7. The limited Strouhal number range therefore provides evidence that Antarctic krill swimming is

highly efficient and that hovering is an energy efficient mechanism to enable its pelagic lifestyle.

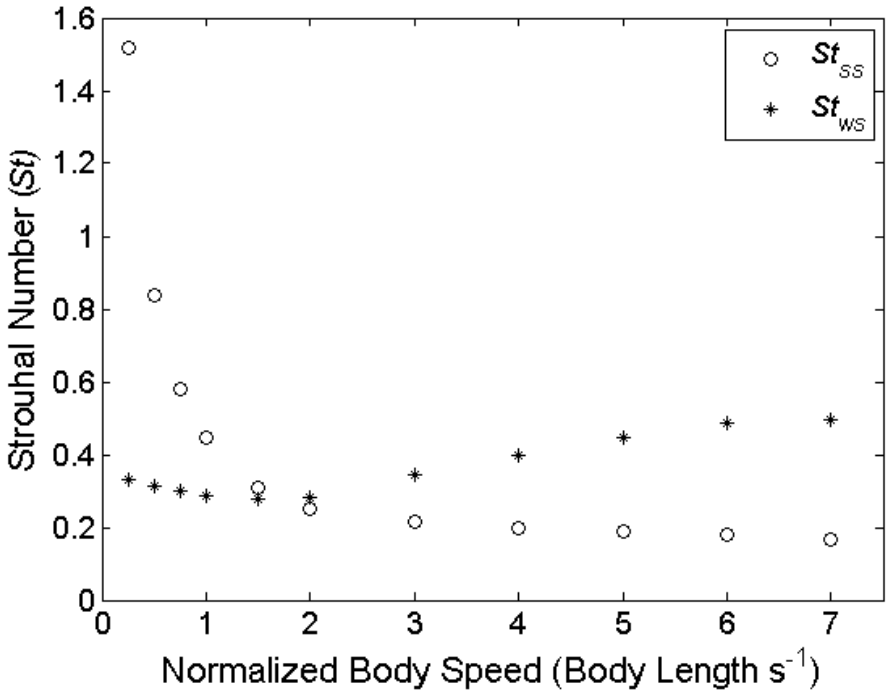

Figure 16.5 Strouhal number (calculated using two different characteristic velocities) as a function of normalized swimming speed.

5.5.3 Hovering Energetics

From the energetic perspective, hovering is likely inexpensive and thus provides an estimate of the minimum energy that krill must devote to locomotion, an important part of determining the energy budget of individual krill (Swadling et al., 2005). Furthermore, when in aquaria both Antarctic and Pacific krill spend the majority of their time hovering (Kils, 1981; Endo, 1993). The induced power analysis provides a quantitative estimate of the energy required for hovering and showed that a 43 mm krill must transfer 4.16×10^{-6}

Joules per second to the water in order to maintain its vertical position. Alternatively, Kils (1981) estimated the power necessary for hovering based on the energy necessary to lift an object the distance that it would fall in a given time period. Essentially, the required power was estimated as the animals' underwater weight multiplied by its sinking speed. For a 43 mm krill, the estimated power via this approach was 5.87×10^{-6} W.

The power required for hovering can also be calculated from the energy dissipated by viscous forces in the seawater. The viscous energy dissipation was calculated at each time point according to the formula:

$$\psi = \mu \left[2\left(\frac{\partial u_x}{\partial x}\right)^2 + 2\left(\frac{\partial u_y}{\partial y}\right)^2 + 2\left(\frac{\partial u_z}{\partial z}\right)^2 + \left(\frac{\partial u_x}{\partial y} + \frac{\partial u_y}{\partial x}\right)^2 + \left(\frac{\partial u_x}{\partial z} + \frac{\partial u_z}{\partial x}\right)^2 + \left(\frac{\partial u_y}{\partial z} + \frac{\partial u_z}{\partial y}\right)^2 \right]$$

The total energy dissipation rate (in units of W) then was found by integrating ψ over the flow volume. The viscous energy dissipation ψ was calculated at three time points in the first data sequence of the flow generated by the pleopods (after removing the vectors inside the visual hull) and at three time points in the second data sequence of the jet beneath the krill. The mean energy dissipation rate estimated for the flow surrounding the pleopods and that estimated for the jet region were added together to give an estimate of the total power required for hovering of 2.93×10^{-6} W, as shown in Figure 5.16. Also included is an estimate of power derived from PIV measurements by Catton et al. (2009). Catton (2009) estimated dissipative power for swimming Antarctic krill using planar PIV data and found a mean energy dissipation rate of 4.0×10^{-6} W based on an assumption of uniform flow disturbance across the width of the krill. Most of the animals studied by

Catton et al. (2011) were performing fast forward swimming or in the transition region between hovering and fast forward swimming and had a mean swimming speed of 77 mm s^{-1}.

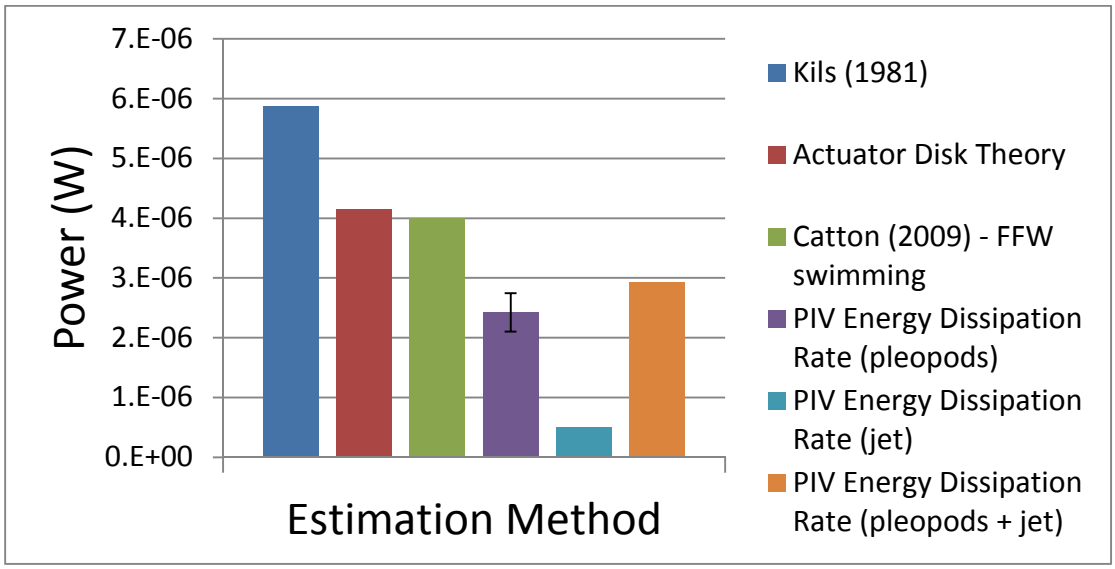

Figure 5.16 Estimates and measurements of power required for hovering for Antarctic krill.

The power values in Figure 5.16 range from 3×10^{-6} W to 6×10^{-6} W and, being of the same order of magnitude, are fairly consistent. Each method of estimating the power has strengths and weaknesses. The actuator disk theory is dependent on a simplified model of pleopod area, which in actuality varies significantly throughout the stroke. The power estimates from the PIV measurements suffers from not having visual access to the entire flow field. The flow behind the telson and beneath the field of view was not taken into account. Furthermore, the calculation of energy dissipation rate depends on velocity gradients, and the strength of those gradients depends on how much smoothing is done to

the flow field in post-processing. On the positive side, the three dimensional data facilitate direct calculation of the needed velocity gradients.

Swadling et al. (2005) measured the metabolic rates of Antarctic krill swimming at various speeds and found a rates ranging from 1.4 – 2.0 mg O_2 g_D^{-1} h^{-1} for krill swimming at 30 mm s^{-1}. Converting to Watts (assuming that 1 ml O_2 equals 0.698 mg O_2 and that 1 ml O_2 = 19.9 J) yields an energy consumption of 1.05 – 1.53 × 10^{-3} W, which, though several orders of magnitude greater than the values estimated theoretically and through viscous energy dissipation, does not account for muscle efficiency or hydromechanical energy losses. Furthermore, Kils (1981) estimated that hovering required only 60% of the krill's energy consumption. Applying this correction factor and assuming values of 0.25 for both types of efficiency losses yields a value of 4.0 – 5.8 × 10^{-5} W, which, although still much larger, is more in line with the estimates and measurements made here. Kils (1981) also found large discrepancies between theoretical estimates and respiration experiments. Finally, Swadling et al. (2005) also found that respiration greatly increased (approximately doubled) as krill increased swimming speed from 30 to 50 mm s^{-1}. This gradient in respiration as krill transitioned out of hovering was much steeper than that found as krill subsequently further increased swimming speed. This indicates that hovering is a low-energy state for Antarctic krill and also points towards hovering being an efficient mechanism of maintaining a pelagic lifestyle.

CHAPTER 6

CONCLUSIONS AND CLOSING REMARKS

While lift-based locomotion in large animals such as fish and turtles and jetting locomotion in jellyfish and squid have been extensively studied, drag-based swimming by crustaceans, particularly those employing multiple pairs of paddles in a metachronal rhythm, remains relatively unexplored. The ecological importance of animals using metachrony is large, with copepods and krill providing a vital link in the food web between phytoplankton and larger, commercially important metazoans. Far from being passive drifters, many of the animals using metachrony show strong swimming ability relative to their size and swim to find food and mates, escape from predators, and to migrate. Furthermore, the hydrodynamics and kinematics of their swimming systems produce communication cues among conspecifics and provide signals to predators. Understanding the design of metachronal locomotion systems, the kinematics with which they operate, and the hydrodynamic result of those kinematics thus has great bearing on planktonic ecology. This study has investigated the design of metachrony and the kinematics and hydrodynamics of metachronal propulsion in Antarctic krill and calanoid copepods.

6.1 Conclusions

Three distinct behavioral swimming gaits (hovering, fast forward swimming, and upside down swimming) each characterized by certain behavioral and hydrodynamic requirements, were identified in the investigation of Antarctic krill swimming kinematics.

Both pleopod stroke frequency and stroke amplitude varied significantly among these three gaits. The transition between hovering and fast forward swimming occurred at a normalized swimming speed of approximately two body lengths per second. As krill increase their speed (transitioning from hovering into swimming forward at up to seven body lengths per second), they first increase beat amplitude and secondarily increase beat frequency. The lag between consecutive beats also increased as the animal transitioned to fast forward swimming. In considering the design components that contribute to metachrony being a successful swimming technique, a comparison among many different species showed that the ratio between the appendage separation distance and appendage length remains relatively constant. This constant ratio possibly reflects an ideal interplay between reducing interference between adjacent appendages and maximizing the sweep that each appendage may travel through the surrounding fluid (and thus the momentum that it may impart).

The flow generated by metachronally stroking appendages was investigated in species on two different size scales (calanoid copepods and Antarctic krill). The escape jump by the calanoid copepod (*Calanus finmarchicus*) displayed high impulsivity, with a tremendous amount of energy delivered to the surrounding water on a time scale of approximately 10 ms. With accelerations of up to 7.4 g, metachronally powered escape jumps are an effective (yet expensive) mechanism for copepods to escape predation. The wake left by the escaping copepod consisted of a stronger posterior vortex ring generated by the metachronally stroking swimming legs and a weaker one generated anteriorly around the body by the impulsive start of the escape, both of which decayed over time. Because both wake and body vortices are present, the flow was modeled as an impulsive stresslet. The

experiments also revealed azimuthal asymmetry in the vortices caused by body yawing and the action of the swimming legs, flow features not considered in previous axisymmetric computational and theoretical models of copepod jumps. The volumetric flow measurements are thus useful in revealing where reality differs from proposed models. The differences in this case were attributed to periodic body yawing during the escape and to spatially distributed force application due to the metachronal kick of the swimming legs.

The extent of a hydrodynamic disturbance is an important consideration for plankton that sense food or predators or mates through hydrodynamic signals such as velocity magnitude or strain rate. In particular, predators are thought to use a velocity magnitude threshold to sense prey. The capability of the tomographic PIV system to measure hydrodynamic signal volume was demonstrated by showing that the volume of the wake generated by the escaping calanoid copepod was much larger than previously expected. In the context of performing a high speed escape, the volumetric extent of the flow disturbance may not be significant considering the prey's goal of immediately removing itself from the vicinity of a predator. Nevertheless, it has been shown that the tomographic PIV system can measure the volumetric extent of more ecologically-relevant flows such as the copepod feeding current or the flow generated by normal copepod hopping.

The flow associated with metachronal hovering in Antarctic krill was investigated in regards to the energy requirements of the pelagic lifestyle. Flows induced by the stroking pleopods, particularly the endopodites, formed a medial stream down the long axis of the krill. One of the most interesting flow features is the formation of tip vortices on the

pleopods, which have not been previously measured on a live animal in low Reynolds number drag-based propulsion. The growth of these vortices contributes to the lift generated by the stroking pleopod. The rhythmic jet-like wake beneath the animal resulting from the beating pleopods also was examined. The diagonally-downward pulsed jet produced by the hovering animal was shown to match the rhythm of the metachronally beating pleopods. The Strouhal number of the Antarctic krill during both hovering and forward swimming was found lie in a high-efficiency zone ($0.2 < St < 0.4$) found for other swimming and flying animals that use lift-based locomotion, thereby suggesting that the metachronal swimming system of Antarctic krill is uniquely adapted for efficiency. In addition, theoretical estimates of induced power and viscous energy dissipation estimates stemming from volumetric flow measurements matched fairly well with previous theoretical estimates of induced power.

6.2 Unique Contributions

Unique contributions of this work include the following:

- Quantification of the pleopod kinematics of freely swimming Antarctic krill via high-speed video; these kinematics are now available for computational fluid dynamics simulations that could provide a better understanding of the benefits of metachronal swimming.
- Identification of three significantly different swimming gaits based on these kinematics.

- Identification of the ratio of the distance between adjacent appendage bases and appendage length as a key parameter in the design and operation of metachronal swimming systems.
- Development of a tomographic PIV system capable of measuring volumetric flow fields around and in the wakes of zooplankton with high spatial and temporal resolution. Furthermore, the tomographic PIV system operates with illumination in the near-IR range (wavelength of 808 nm), a range to which most plankton are insensitive.
- Volumetric measurements of wake generated by escaping calanoid copepod, including the first three-dimensional measurement of wake volume and first three-dimensional measurement of viscous energy dissipation rate to estimate energy requirements.
- Assessment of proposed flow models for copepod jumps (e.g. impulsive Stokeslet, impulsive stresslet, and computational fluid dynamics model) in light of volumetric flow data and realization of significance of azimuthal asymmetry due to swimming leg action and body yawing.
- Volumetric flow measurements around a hovering Antarctic krill.
- Application of actuator disk theory to a hovering pelagic species.
- Quantification of the Strouhal number in the wake flow to demonstrate that Antarctic krill occupy a high efficiency zone ($0.2 < St < 0.4$).
- The first flow measurements of daphniid hopping.

- Proposal of a model for daphniid hopping consisting of two impulsive Stokeslets (applied in the same direction) separated by short distance representing the thickness of the daphniid's body.

6.3 Limitations and Challenges

The tomographic PIV system that was developed and used as part of this study of metachronal propulsion imparted both strengths and challenges. The major strength was, of course, that three-dimensional (volumetric) velocity vector data could be obtained surrounding (most of) the animal with high temporal resolution, thereby leading to new capabilities and orders of magnitude more information than would be obtained with a more conventional 2D PIV system. One challenge of the tomographic PIV system is that, especially with high temporal resolution, large quantities of data are generated. Each recorded event then requires a significant amount of time and effort in order to mask out the animal, reconstruct the particle intensity volumes, cross-correlate the reconstructed volumes, and produce vector fields. Faster processors and better tools for managing this type of data will no doubt speed tomographic PIV processing in future. In the meantime, foresight and good judgment are needed to select an appropriate time resolution and to choose for analysis those recorded events which best demonstrate the phenomenon of interest. Too high of a temporal resolution can limit the possibility of experimental replicates. For instance, Chapter 4 was based on one data sequence occupying only 655 ms but which took several months to process and analyze. Greater certainty in drawing conclusions concerning whether the impulsive Stokeslet or impulsive stresslet model

more faithfully represented the flow data could have been possible with further replicates. Similarly, the results concerning krill hovering in Chapter 5 are based on a single video sequence.

A second challenge of the tomographic PIV system is difficulty in obtaining a good volume reconstruction (and thus non-spurious vectors) in the areas near to the animal's body. These areas are often occluded from the view of at least two cameras by the organism itself, leading to poor particle reconstruction in the areas that are the most interesting. Similarly, the visual hull of the animal often blocks volumes in front of and behind the animal, thereby preventing flow measurement in those areas. Measuring the wakes of animals (as was done with the escaping copepod in Chapter 4) is therefore much more straightforward than measuring flow directly adjacent to the organism. Better tools for overcoming this challenge likely will be built into commercial tomographic PIV software in the near future.

A final challenge is that current tools for working with and visualizing volumetric flow data (such as volumetric light intensity fields or three-dimensional vector fields), especially in reference to a moving, arbitrarily shaped body, are lacking in capability. Specific lacking capabilities include the ability to automatically apply visual hull masks at multiple time steps in DaVis and the ability to mask vectors inside a visual hull in either DaVis or Tecplot. These capabilities will likely be included in future versions of these software packages. Visualization techniques for three-dimensional vectors fields will also improve with the development of anaglyph-based visualization software for use on computer monitors.

6.4 Future Directions

Metachronal propulsion is a theme that among zooplankton has many variations. Morphology, kinematics, body design, number of appendages (and appendage segments), appendage flexibility, and size (flow regime) are all variables that affect how a particular organism uses its multiple appendages and the flow that it produces. A parametric study using a dynamically scaled model would be useful in further exploring this design space. A dynamically scaled model with good optical access (e.g. transparent appendages) could particularly be used to make a detailed investigation of the flow interaction and possible synergy between adjacent appendages. A model on a rail with air bearings and force transducers would also be useful in investigating the 'synergy' possibility that two metachronally stroking appendages could travel more than twice as far as a single stroking appendages. The effect of the ratio of appendage length to appendage spacing could also be elucidated with this type of dynamically-scaled model. Another avenue of particular interest is the effect of appendage morphology. Many crustaceans using metachrony, such as copepods and krill, have appendages coated with bendable setae that effectively increase their surface area. Others such as stomatopods (which swim at much higher speeds than similarly sized Antarctic krill) do not bear these setae but instead rely on flat, plate-like appendages. A detailed fluid mechanics study of the effect of bristled appendage tips, especially with regard to the effect on vortices formed on the appendage edges, would be illuminating. Finally, a biomimetic 'krillbot' could be developed to better learn how the metachronal swimming system works. A paddlewheel may serve as a reasonable proxy to the mechanically and kinematically complex system used by the krill.

Furthermore, the fluid mechanic result of metachronal stroking in many plankters often seems to be a downward directed jet (as seen with the hovering Antarctic krill in Chapter 5). From data presented here and other preliminary tomographic PIV data, this seems to be the case for hovering euphausiids (krill), certain stages of crab larvae, and some species of copepods (such as *Hesperodiaptomus shoshone*). Jet-propelled plankton may in fact be quite common, and it is interesting that these organisms can create a continuous jet by rhythmic beating of multiple appendages. Characterizing these jets (in terms of unsteadiness and from an energetic standpoint) and comparing them to other organisms that create jets in a different way (such as a squid or a nautilus) may provide insight into this form of locomotion. Swimming by pushing water downward in a jet also presents an interesting challenge from the controls perspective.

A particularly interesting avenue of investigation is linking the Antarctic krill flow fields recorded in this investigation to their behavior in the field. Antarctic krill are known for their exceptional schooling behavior, and it is thought that the perception of hydrodynamic signals is one modality through which communication is accomplished during aggregation. The flow fields of fast forward swimming Antarctic krill measured here can lead to a better understanding of the signals that schooling krill will produce and experience.

Finally, the tomographic PIV system developed here for application to zooplankton opens a world of possibilities for further experiments in biofluid mechanics and sensory ecology. Further experiments already performed but not presented in this thesis include characterization of swimming by pteropods (sea butterflies), several species of copepods and daphniids, and several stages of crab larvae. In addition, a series of experiments to

characterize the sensory threshold of four species of copepods and two species of daphniids to predator mimics (steady and impulsive siphon flows mimicking the suction feeding of piscine predators) were performed.

In addition to using the new tool of tomographic PIV for studying plankton, the capabilities of the tool itself should be expanded through continual improvements in the acquisition and processing software. Possible improvements include single image self-calibration (to correct for camera vibration by calibrating each image separately) and a more streamlined approach to masking out arbitrarily shaped objects from reconstructed light intensity volumes. Better tools for visualizing arbitrarily shaped objects and incorporating them into three dimensional flow fields would also prove useful and will likely be developed in the not too distant future.

APPENDIX A

DAPHNIA SWIMMING HYDRODYNAMICS

A.1. Introduction

As reviewed in Chapter 2, the flow physics of daphniid swimming and the sensitivity of daphniids to hydrodynamic signals have not been well studied. In this Appendix, volumetric flow measurements of *Daphnia magna* hopping are presented for the sake of comparison to the measurements of the escape jump of a *Calanus finmarchicus* copepod presented in Chapter 4. The kinematics and flow physics of the hop are characterized, and the volume of flow disturbance and energy dissipated in the flow also are discussed.

A.2. Materials and Methods

A.2.1. Experiment description

Approximately twenty *Daphnia magna* (Carolina Biological Supply, Burlington, NC) of various sizes were placed in a small aquarium (approximately 5 cm on each side) filled with fresh water and seeded with light-reflecting particles with a mean diameter of 10 μm. The free-swimming animals were filmed at 100 fps using a tomographic PIV system (Murphy et al. 2012) composed of four synchronized high speed Phantom v210 cameras (Vision Research, Wayne, NJ). Each camera was equipped with a 30 mm extension ring, a 2× teleconverter, and a 200 mm focal length lens (Nikon, Tokyo, Japan) in order to obtain a field of view of approximately 1 to 2 cm^2.

The target volume was illuminated by a continuous wave 7 W lasers (CrystaLaser, Reno, NV) lasing with a near-infrared (IR) wavelength (808 nm). The animals did not appear to react to the illumination. The laser beam was expanded and collimated using spherical plano-concave and biconvex lenses, and an adjustable aperture was used to create a beam with rectangular cross-section of approximately 20 × 8 mm (height × width). Image acquisition was controlled through DaVis software (LaVision, Ypsilanti, MI) on a laptop PC and is synchronized by a high-speed controller that generates timing signals for the cameras.

A.2.2. Data Analysis

One 230 ms video sequence of a daphniid (body length of 2.3 mm) performing a hop was chosen for analysis. This video was chosen because the animal was well positioned within the laser sheet and was facing towards the four cameras, thereby providing a clean view of both of its swimming appendages. Kinematics of the animal jump were obtained by manually tracking the animal in 3D space in DLTdv5.

In order to represent the animal's position within the measurement volume, the visual hull technique (Adhikari and Longmire, 2012; Murphy et al, 2012) was used to create a volumetric outline of the animal at each time point. Briefly, the animal's outline was manually traced in each camera view. The four animal silhouettes were back-projected into a volume and multiplied together using the Multiplicative Line of Sight (MLOS) algorithm in DaVis. The volume in which the four back-projections intersect is the animal's visual hull and represents the maximum possible volume occupied by the animal. The front-to-back elongation of the animal is a function of the angle between the

cameras such that a smaller interior angle will lead to a more elongated visual hull depth. An example of the daphniid visual hull is shown in Figure A.1.

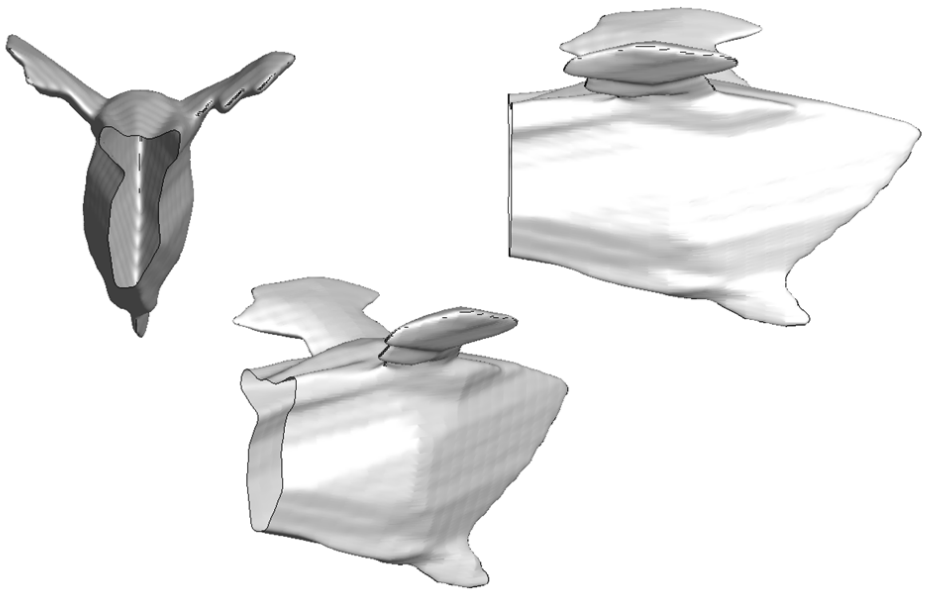

Figure A.1: Visual hull of *Daphnia magna* from three different perspectives.

The PIV images were pre-processed (sliding minimum subtraction over 3 × 3 pixels; normalization with local average over 100 × 100 pixels; Gaussian smoothing and subsequent sharpening of particles), and a volume self-calibration was iteratively performed to correct for errors in the calibration (Wieneke 2008). Images were reconstructed into a light intensity volume by the MART algorithm in DaVis. The previously created visual hull was used to mask the reconstructed animal from this light intensity volume. After masking, consecutive reconstructed volumes were cross-correlated in a multi-pass process to produce a volume field of three-component velocity

vectors. The reconstructed and cross-correlated volume was approximately 6 × 8 × 6 mm ($x \times y \times z$).

In order to investigate the extent of the signal volume generated by the daphniid hop, the volume of the flow field exceeding a threshold value of 5 mm $s^{-1}$was calculated at each point in time. Prior to this step, the vectors inside the animal volume (the visual hull) were removed so as not to influence the signal volume calculation. Furthermore, the viscous energy dissipation also was calculated at each time point according to the formula:

$$\psi = \mu\left[2\left(\frac{\partial u_x}{\partial x}\right)^2 + 2\left(\frac{\partial u_y}{\partial y}\right)^2 + 2\left(\frac{\partial u_z}{\partial z}\right)^2 + \left(\frac{\partial u_x}{\partial y} + \frac{\partial u_y}{\partial x}\right)^2 + \left(\frac{\partial u_x}{\partial z} + \frac{\partial u_z}{\partial x}\right)^2 + \left(\frac{\partial u_y}{\partial z} + \frac{\partial u_z}{\partial y}\right)^2\right]$$

The total energy dissipation rate (in units of W) was found by integrating ψ over the flow volume.

A.3. Results

A.3.1. Kinematics

Figure A.2 shows the daphniid speed over time. The daphniid initially is sinking after completing a hop approximately 80 ms prior to the time point $t = 0$ in Figure A.2. The daphniid begins its 70 ms long power stroke at this time point, and the animal's speed increases to almost 40 mm s^{-1}. The maximum acceleration of the animal during this time

period is approximately 1.8 m s^{-2}. The daphniid is also rotated nose-down during the power stroke because its antennal stroke plane is inclined.

The recovery stroke begins at approximately t = 70 ms and lasts until t = 130 ms. The daphniid appendages remain motionless while sinking very slightly and rotating back to a more vertical position until t = 220 ms, at which time it begins its next power stroke.

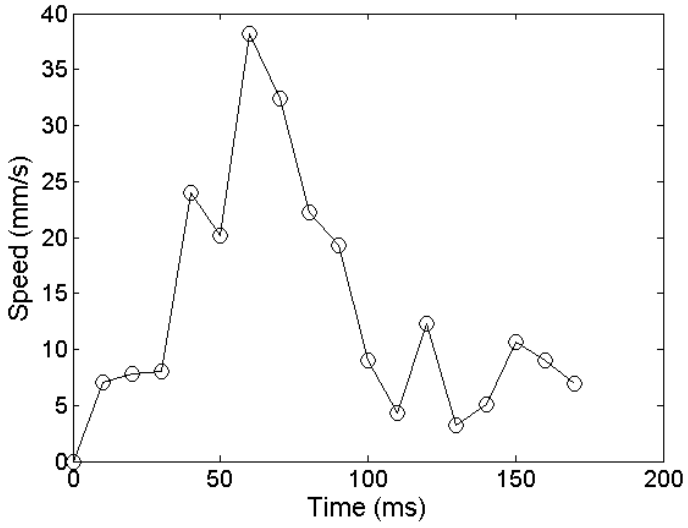

Figure A.2: *Daphnia magna* speed during one complete hopping cycle

A.3.2. Flow Fields

The flow generated by the daphniid in the 60 ms following initiation of its hop is shown in the six frames in Figure A.3. The single z-axis plane that is plotted roughly aligns with the daphniid's mid-section at the beginning of the jump (i.e. a frontal plane). The daphniid is facing out of the page. As time progresses, the daphniid moves upward and in

the positive z direction (out of the page). Each of these frames represents a time period of 10 ms over which two consecutive images were cross-correlated to measure the flow motion, and the daphniid position at the end of this time period is shown. For ease of viewing, only the components of the velocity vectors parallel to the plane are plotted.

At t = 10 ms after hop initiation (as seen in Figure A.3), downward flow from the daphniid's previous hop with speeds of up to 5 mm s^{-1} can be seen to the left of and below the animal. The reason that no flow is seen to the right of the animal is that the animal is slightly rotated (around a vertical axis) relative to the presented plane. At t = 20 ms, the second antennae have begun to move downward and drag flow behind them at approximately 5 mm s^{-1}, as seen especially on the antennae on the right, a trend that continues at t = 30 ms. At t = 40 ms, with the power stroke about halfway accomplished, the animal has begun to move up significantly, and it pushes flow ahead of it in a bow wake. Furthermore, the flow that is dragged down by the antennae seems to follow the contour of the body and curves around to vacate the volume left by the translating daphniid. Induced drift flow following behind the animal with speeds of up to 6 mm s^{-1} continues throughout the rest of the power stroke. The fluid dragged down by the antennae is shed as the antennae fold close to the body and continues downward at speeds of up to 8 mm s^{-1}. The daphniid continues to travel upwards during the remainder of the power stroke (through t = 80 ms) until viscous forces bring it to a halt during the recovery stroke (at approximately 110 ms after the stroke initiation).

Figure A.4 shows the flow field around the daphniid during its recovery stroke (in the same frontal plane as that shown in Figure A.3). As the daphniid moves upwards until about t = 110 ms, it continues to drag flow upwards behind it. The flow initiated by the

second antennae power stroke continues to develop and reaches speeds of over 10 mm s^{-1}. Left-right asymmetry is evident in the flow here and, again, is likely due to slight inclination or rotation of the animal relative to the presented plane. At t=110 ms the flow begins to decay. By t = 130 ms after hop initiation, the daphniid's antennae are unfolded and ready to stroke again. To further illustrate the flow decay, two further time points are shown in Figure A.5 (in the same frontal plane as Figures A.3 and A.4). At t=220 ms after the first hop, the daphniid begins its next hop. Again, downward flow from the previous stroke is still present. Due to its drag-inducing, setae-bearing antennae, the daphniid has not sunk appreciably by this point.

Finally, Figure A.6 shows the flow in an x-axis plane that intersects the tip of the animal's left antennae as it sweeps through its power stroke. Of particular interest is the flow in the negative z-direction at time points 80 and 100 ms after the hop, a phenomenon due to the inclined stroke plane of the antennae.

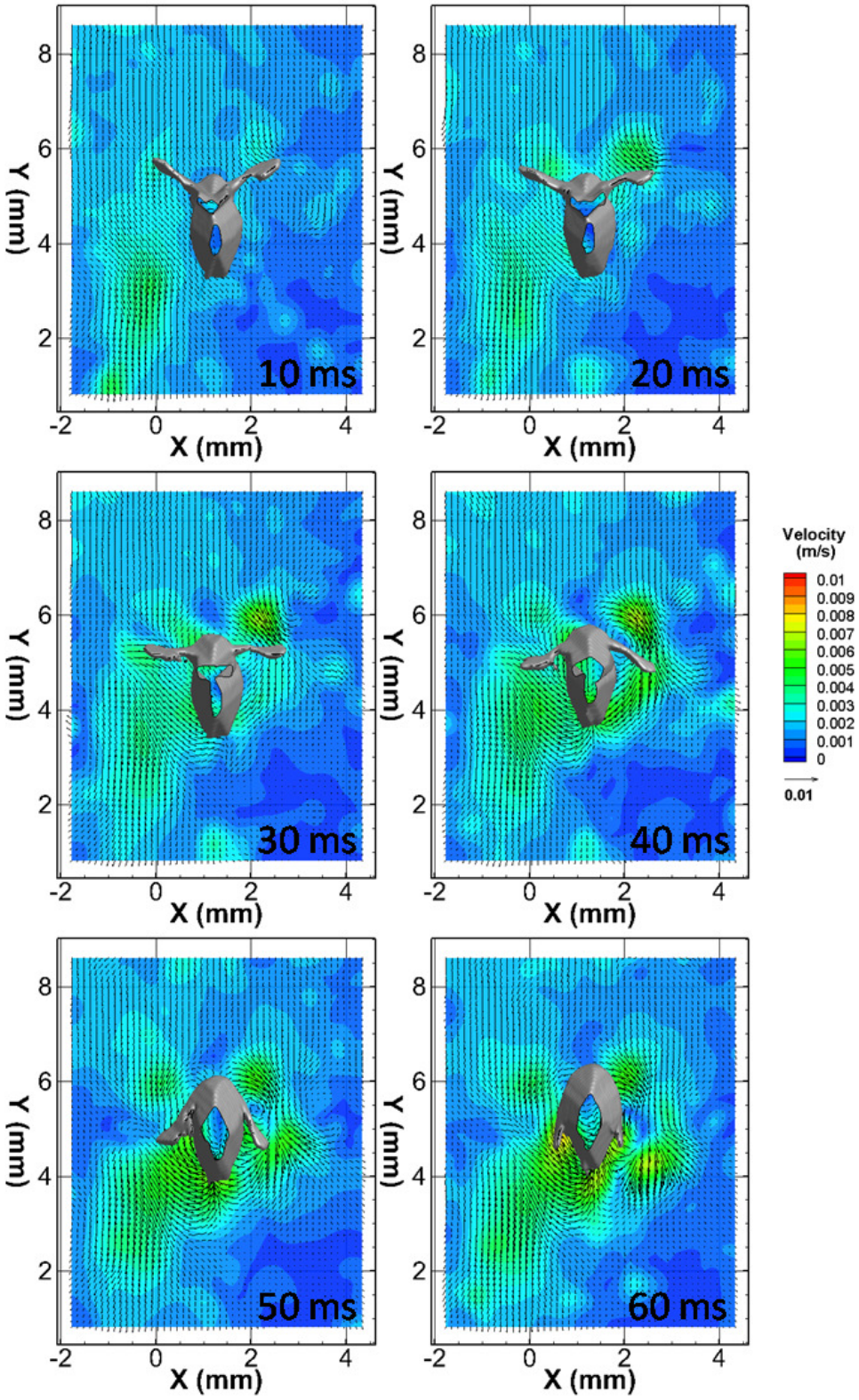

Figure A.3: Flow field in the daphniid frontal plane during its power stroke.

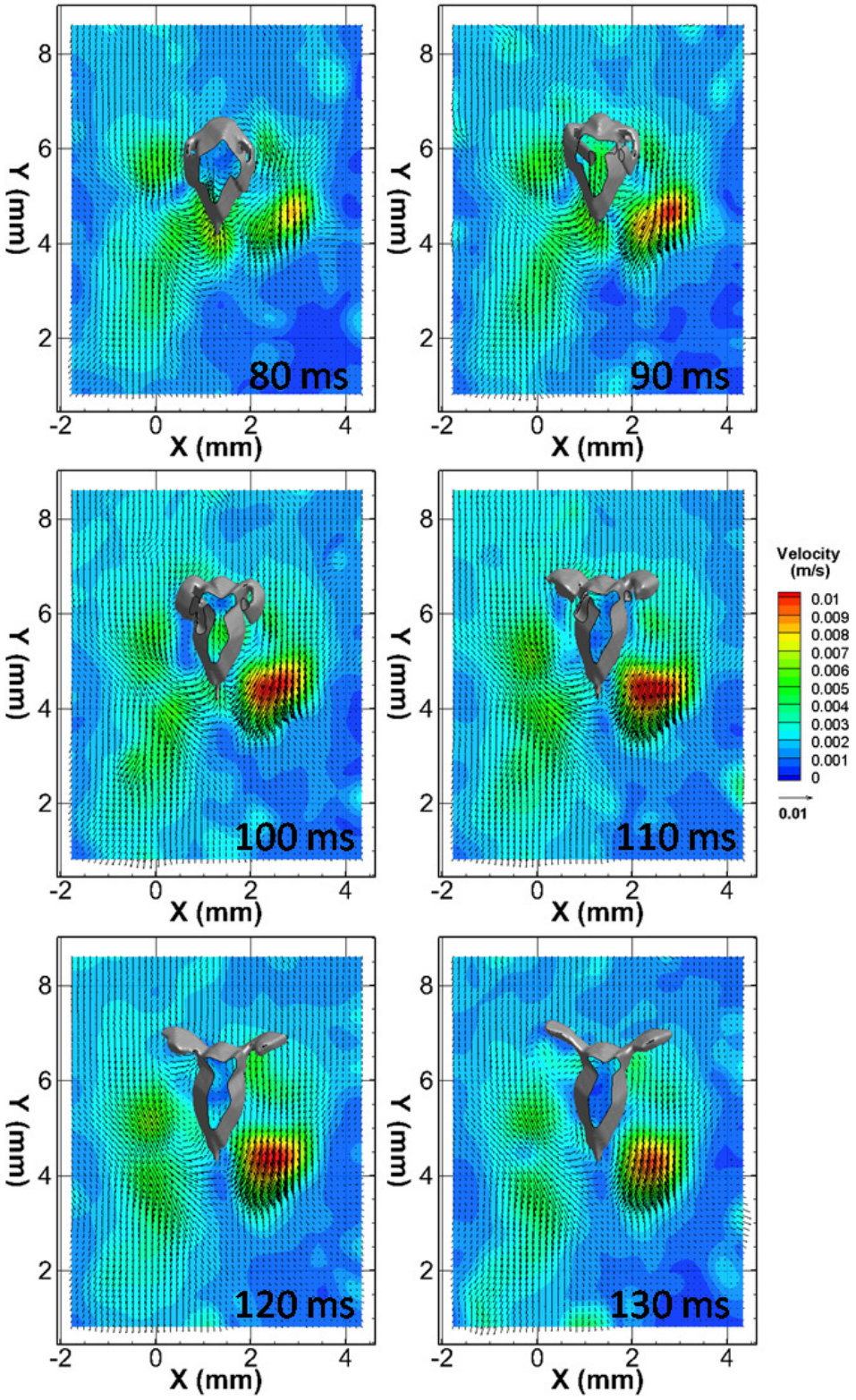

Figure A.4: Flow field in the daphniid frontal plane during its recovery stroke.

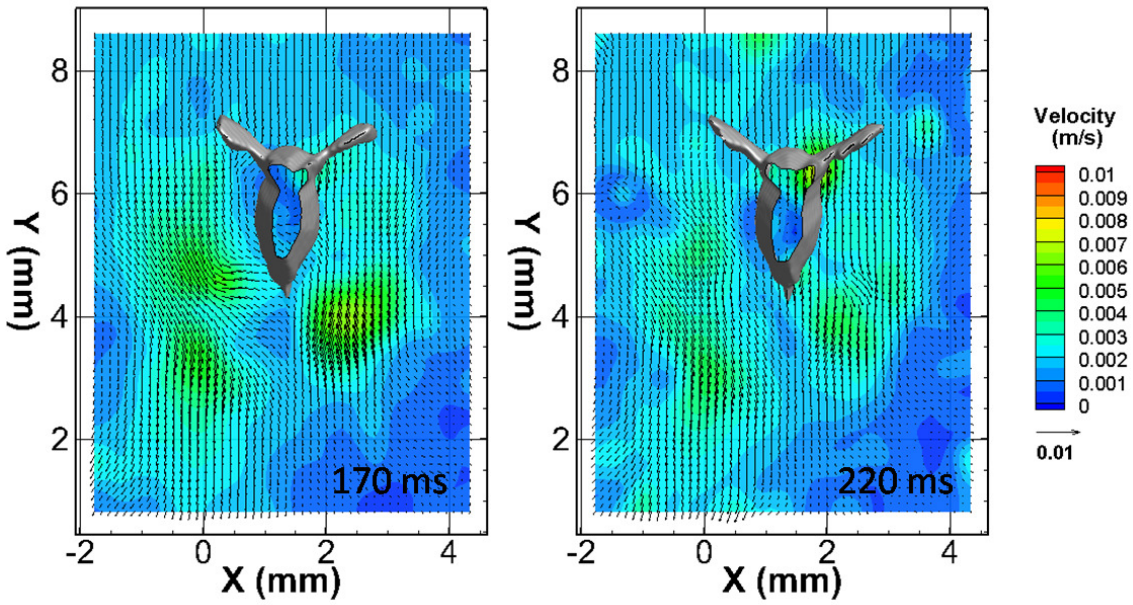

Figure A.5: Flow field in the daphniid frontal plane after its recovery stroke.

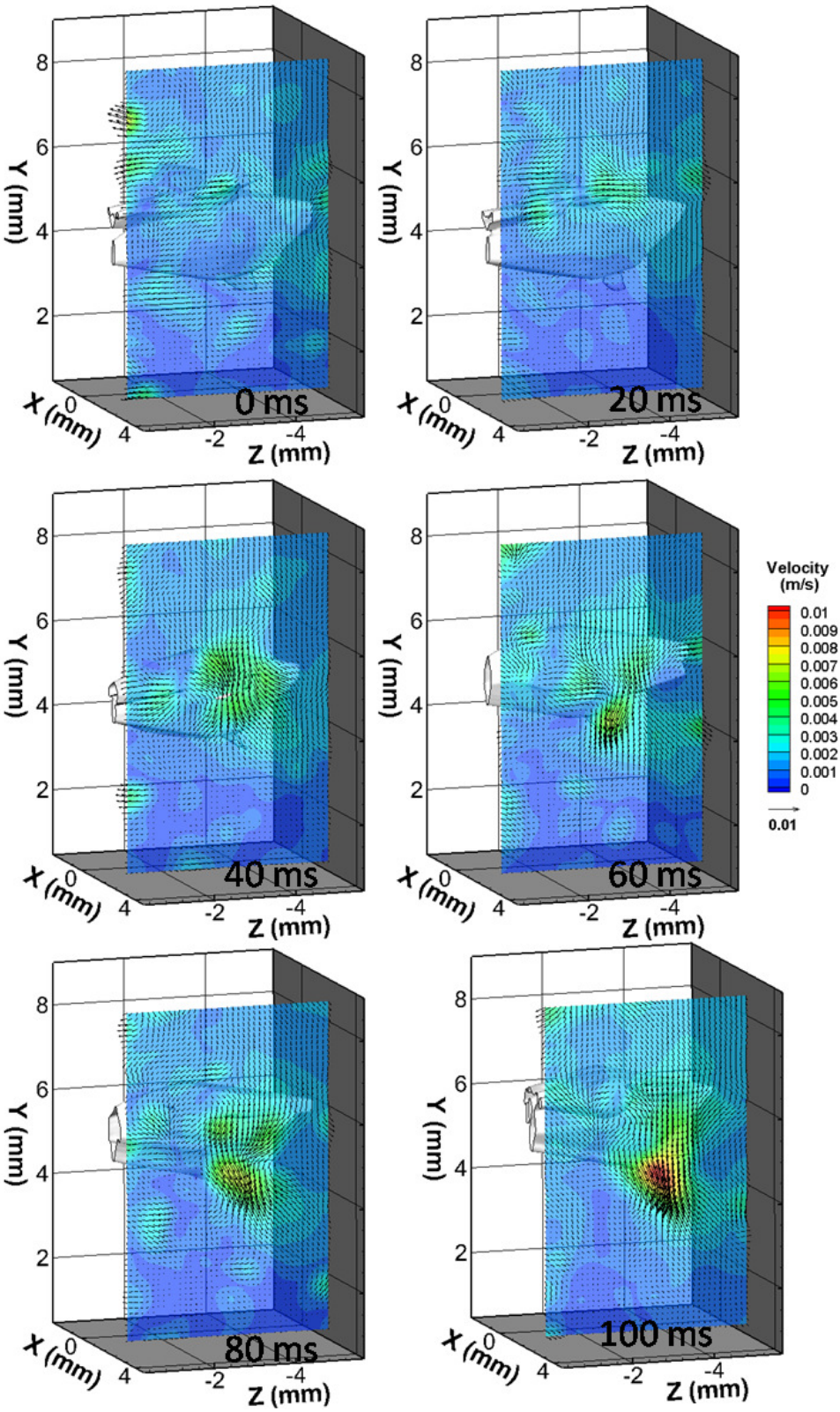

Figure A.6: Flow in an x-axis plane to the daphniid's side during its hop.

A.3.3. Signal Volume

Figure A.7 shows signal volume as a function of time. At the beginning of the stroke, flow from the previous stroke has not yet completely subsided, and approximately 5 mm^3 of flow exceeding the 5 mm s^{-1} threshold remain. As the animal performs its power stroke, that volume rapidly increases to about 20 mm^3 and subsides back down to the baseline level of 5 mm^3 over roughly 200 ms.

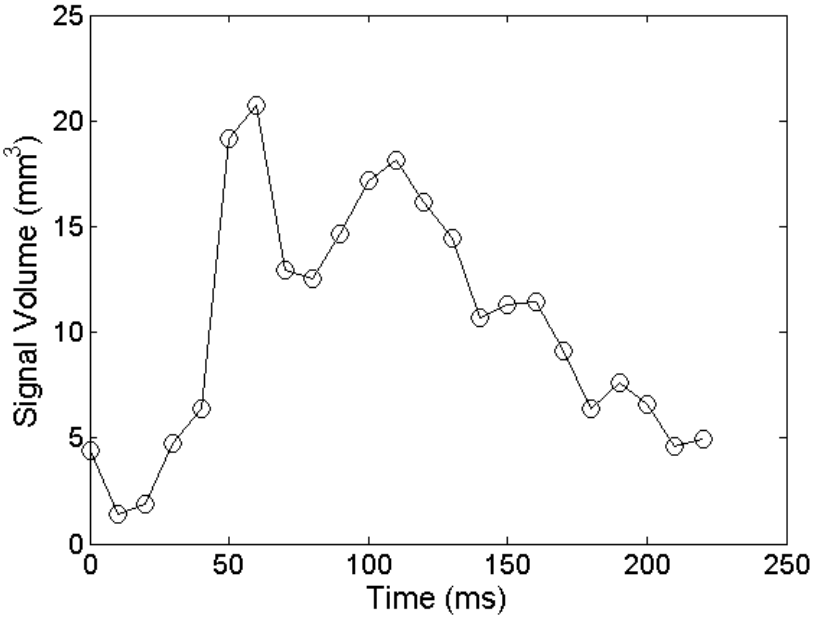

Figure A.7: Volume of flow exceeding a 5 mm s^{-1} threshold throughout the hop of a *Daphnia magna*.

A.3.3. Viscous Energy Dissipation

Figure A.8 shows viscous energy dissipation rate (in W or J s^{-1}) as a function of time. Energy dissipation spikes from a baseline of less than 3×10^{-9} W to almost 7×10^{-9} W as the daphniid performs its power stroke. Viscous effects in the flow gradually dissipate the kinetic energy down to its initial level over 200 ms.

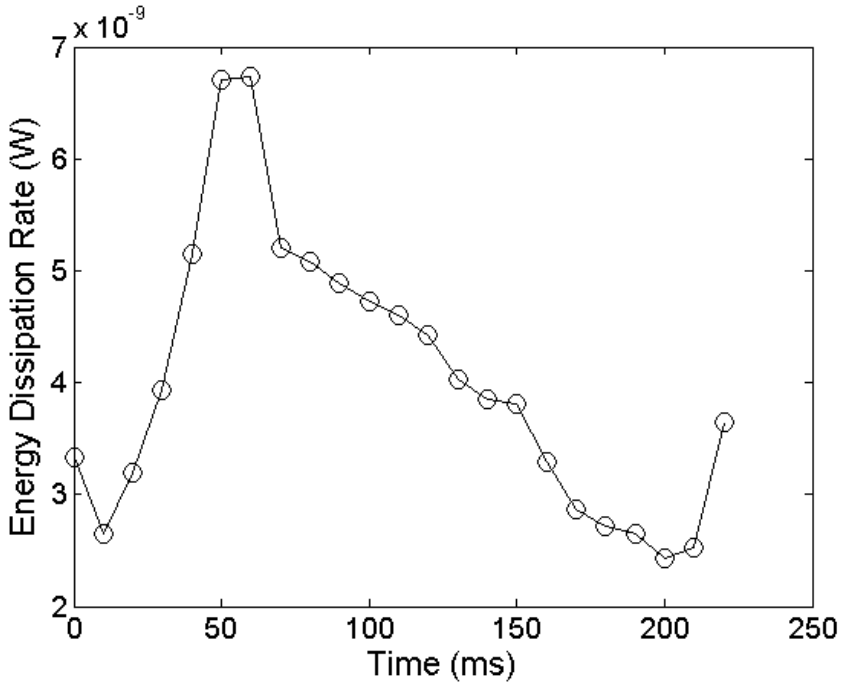

Figure A.8: Viscous energy dissipation rate as a function of time during ahop by *Daphnia magna*

A.4. Discussion

A.4.1. Comparison with Copepod Escape

Though daphniids do exhibit specific escape behavior characterized by increased beat frequency and stroke strength (Dodson et al, 1995), this behavior was not captured during the experiments. The swimming event analyzed here is one in which the daphniid is performing its normal swimming behavior (periodic hops), not one in which the animal is attempting to escape from a threat. It is therefore difficult (and perhaps not entirely fair to the daphniid) to compare a daphniid hop with a copepod escape jump. Comparing a daphniid hop to a copepod hop would be a better comparison. Nevertheless, doing so may be instructive since daphniid hops and copepod escapes do share the characteristic of impulsivity and therefore may be considered as 'bookends' spanning the entire spectrum of low Reynolds number impulsive locomotion.

In comparing kinematics, the *Calanus finmarchicus* considered in Chapter 4 reached maximum speeds of over 500 mm s^{-1} while accelerating at a rate of 73 m s^{-2} while the *Daphnia magna* considered here reaches a peak speed of almost 40 mm s^{-1} while accelerating at 1.8 m s^{-2}. The order of magnitude difference in peak speeds and accelerations between these two animals likely is most representative of the fact that copepod muscles can provide power at levels much higher than that of other organisms (Kiørboe et al. 2010b; Lenz et al.2004). Other contributing factors may include the fact that the copepod strikes metachronally with multiple swimming legs and that the daphniid is not performing an escape behavior characterized by a stronger stroke.

The copepod jump and daphniid hop may also be compared in terms of hydrodynamic signal extent. Though the animals have the same body length, the copepod jump affected a 40 mm^3 maximum volume while the daphniid hop affected a 20 mm^3 maximum volume (i.e. increased velocity magnitude beyond a 5 mm s^{-1} threshold in that volume). It is somewhat surprising that the volume affected by the daphniid is as large as it is. This may be because the flow disturbance is produced by appendages on opposite sides of its body. If the same force were applied on only one side of the body (either in metachronal fashion or by one power stroke), it is doubtful whether the flow disturbance would be as large. Because the daphniid's second antennules are on opposite sides of its body, the generated flow is more spatially distributed.

The copepod escape jump and daphniid hop showed dramatic differences in the amount of energy dissipated in the water by viscous forces. While the peak energy dissipation rate for the copepod escape was 4.4×10^{-7} W, that for the daphniid hop was two orders of magnitude less (almost 7×10^{-9} W). This difference underscores the highly effective escape system of the copepod and its ability to transfer large amounts of momentum to the surrounding flow medium in a short period of time.

The biggest difference in the resulting flow between the daphniid and copepod is the apparent absence of a vortex ring produced by the daphniid hop in Figures A.3 and A.4. This absence is unexpected since Gries et al. (1999) described the wake of similarly sized hopping *Daphnia* as a mushroom-shaped vortex. One possibility is that these vortices may have been caused by buoyant effects since their experiments were performed in a Schlieren apparatus to observe flow structures. Further examination of the present data, however, shows that separate viscous vortex rings may in fact be caused by each of the

antennae, but that most of the rotation in that ring may occur in the sagittal plane. Figure A.9 shows vorticity and velocity vector fields at 120 ms after hop initiation (at the end of the recovery stroke). Although vorticity is present, little flow curvature is evident in the frontal (*x*-*y*) plane. The upward motion of the daphniid body contributes to some flow rotation in the frontal plane, but a vortex ring (like that seen with the copepod flow) is not present. More flow rotation is seen in the sagittal plane. Where this flow curvature can be seen (i.e. the negative vorticity in the sagittal plane), the stagnation point (vortex center) is clearly separated from the point of maximum vorticity. This separation is characteristic of impulsively applied forces such as the impulsive stresslet and impulsive Stokeslet (Kiørboe et al. 2010a, Jiang and Kiørboe 2011b). Figure A.10, which shows an iso-surface of the vorticity magnitude (at a vorticity magnitude of 15.2 s^{-1}), further reveals the asymmetry in the vortex ring generated by the antennae stroke. Little vorticity is seen in the frontal plane far from the daphniid body while more is seen in the anterior and posterior directions. This asymmetry may be related to the biramous architecture of the daphniid second antennae, with separate branches protruding in different directions and influencing different areas of the flow. Because each antennae produces a separate vortex ring, it may be possible to model the flow associated with a daphniid hop as a pair of impulsive Stokeslets (applied in the same direction) separated laterally by some distance which represents the body thickness of the animal, as shown in Figure A.11.

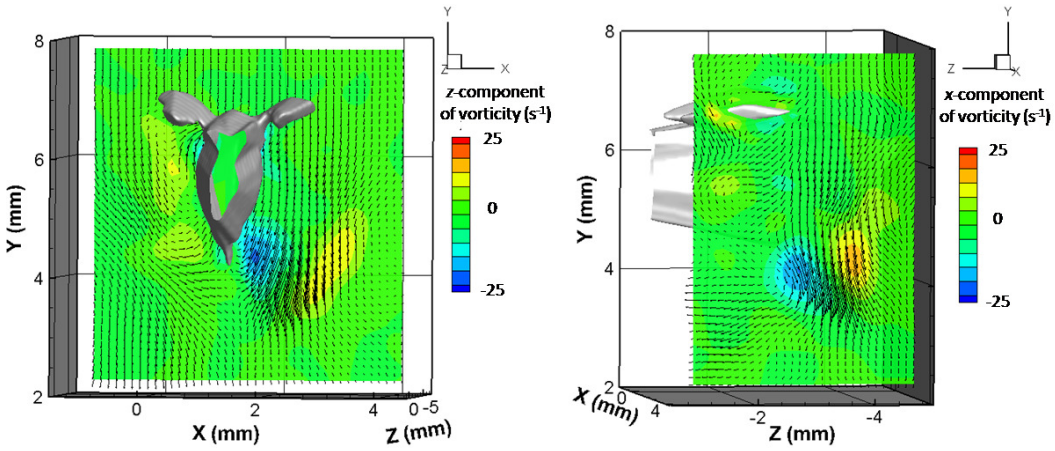

Figure A.9: Vorticity and velocity vector fields at t = 120 ms after hop initiation. The left panel shows contours of the z-component of vorticity (in a x-y plane), whereas the right panel shows contours of the x-component of vorticity (in a y-z plane). The cores of the viscous vortex ring, resulting from the power stroke of the daphniid's left antenna, can be seen in both views.

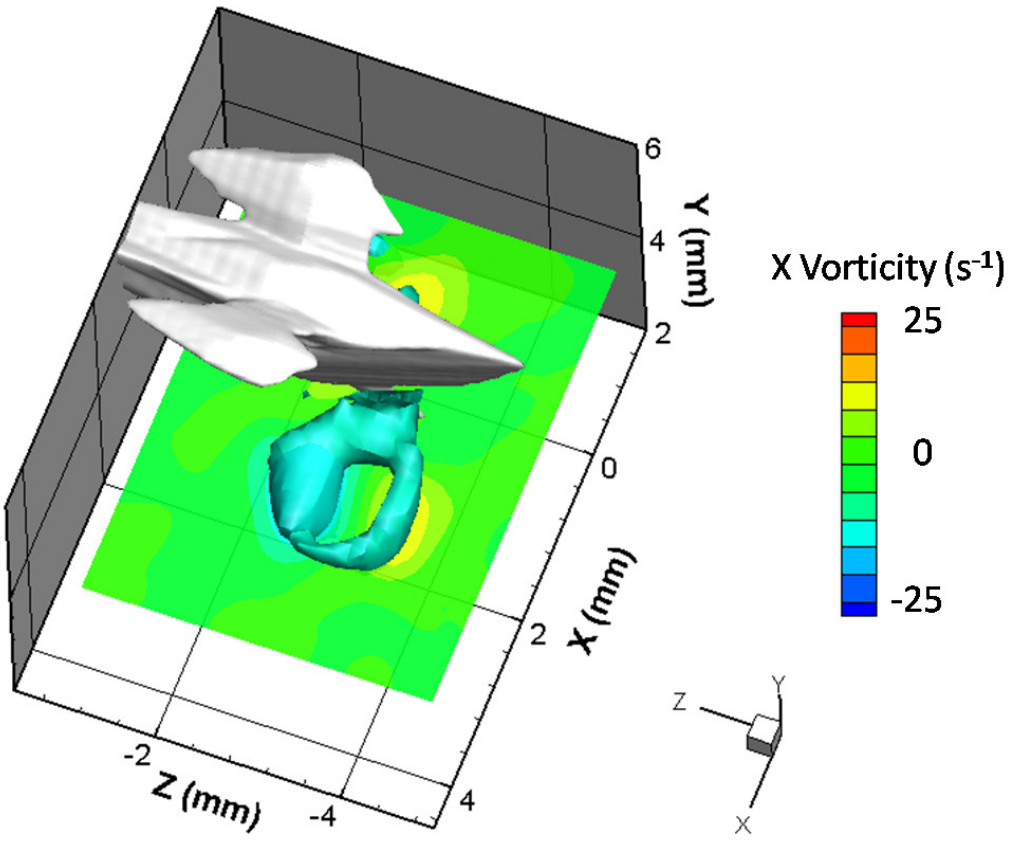

Figure A.10: Overhead view of daphniid at t = 120 ms after jump initiation. The three-dimensional iso-surface shown beneath the daphniid connects points in space that have a vorticity magnitude of 15.2 s^{-1}. Color contours in the plotted plane represent the x-component of vorticity. Asymmetry in the viscous vortex ring is apparent, with less flow rotation in the portion of the vortex ring distal from the body.

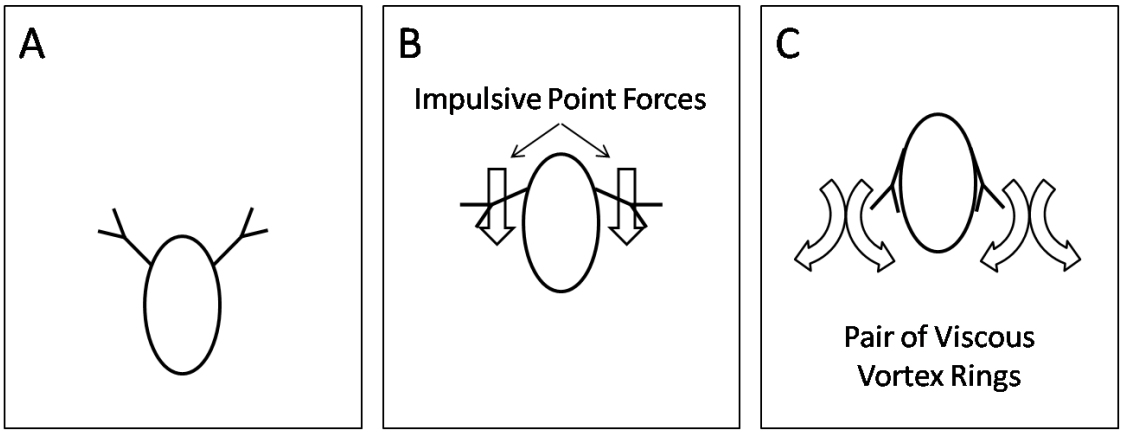

Figure A.11: Model of flow produced by daphniid hopping. Two impulsive point forces (impulsive Stokeslets) separated by some distance representing the lateral width of the daphniid may model the flow as a pair of interacting viscous vortex rings.

A.5. Conclusions

In sum, the daphniid hop, while in many aspects quite different from the escape jump of a calanoid copepod, also shares some similarities. While the copepod jump exhibits kinematic and energetic characteristics that are orders of magnitude larger than those produced by the hopping daphniid, the fluid mechanics of both can be represented by impulsively applied forces that result in viscous vortex rings that decay over time.

REFERENCES

Abrahamsen, M. B., Browman, H. I., Fields, D. M., and Skiftesvik, A. B. (2010)."The three-dimensional prey field of the northern krill, *Meganyctiphanes norvegica*, and the escape responses of their copepod prey," *Marine Biology*, 157, 1251-1258.

Adhikari, D., and E. K. Longmire. 2012. Visual hull method for tomographic PIV measurement of flow around moving objects. Exp. Fluids (in revision).

Alben S, Spears K, Garth S, Murphy D, Yen J (2010) Coordination of multiple appendages in drag-based swimming. J R Soc Interface 7: 1545-1557.

Alcaraz, M., and J. R. Strickler. 1988. Locomotion in copepods: pattern of movements and energetic of *Cyclops*. Hydrobiologia 167/168:409-414.

Alexander DE (1988) Kinematics of swimming in two species of *Idotea* (Isopoda: Valvifera). J Exp Biol 138: 37-49.

Alexander, R. M. 1990. Size, speed and buoyancy adaptations in aquatic animals. Amer. Zool. 30(1): 189-196.

Alexander RM (2003) Principles of Animal Locomotion. Princeton University Press, Princeton.

Aleyev, Y. U. 1977. Nekton.The Hague: Dr. W. Junk b.v. Publishers.

Anderson, J. M., Streitlien, K., Barrett, D. S., and Triantafyllou, M. S. 1998. Oscillating foils of high propulsive efficiency. J. Fluid Mech. 360, 41-72.

Anderson, E. J. and Grosenbaugh, M. A. 2005. Jet flow in steadily swimming adult squid. J. Exp. Biol. 208, 1125-1146.

Andrews, J. C. 1983. Deformation of the active space in the low Reynolds number feeding current of calanoid copepods. Can. J. Fish. Aquat. Sci. 40, 1293-1302.

Anker A (2010) The shrimp genus *Salmoneus* Holthuis, 1955 (Crustacea, Decapoda, Alpheidae) in the tropical western Atlantic, with description of five new species. Zootaxa 2372: 177-205.

Arroyo, M. P., and K. D. Hinsch. 2008. Recent developments of PIV towards 3D measurements. p. 127-154. *In* A. Schroeder and C. E. Willert [eds.], Particle image velocimetry: Topics appl. physics, Vol. 112. Springer-Verlag, Berlin.

Atkinson, A., Siegel, V., Pakhomov, E. A., Jessopp, M. J. and Loeb, V. (2009) A re-appraisal of the total biomass and annual production of Antarctic krill. Deep Sea Research Part I: Oceanographic Research Paper 56(5):727-740

Atkinson, C., and J. Soria. 2009. An efficient simultaneous reconstruction technique for tomographic particle image velocimetry. Exp. Fluids 47:553-568.

Baillieul, M. and Blust, R. (1999)."Analysis of the swimming velocity of cadmium-stressed *Daphnia magna*," *Aquatic Toxicology*, 44, 245-254.

Blake, R. W. (1979). The energetics of hovering in the mandarin fish (*Synchropus picturatus*). J. Exp. Biol. 82, 25-33.

Borazjani, I, Sotiropoulos, F., Malkiel, E., and Katz, J. (2010)."On the role of copepod antennae in the production of hydrodynamic force during hopping," *Journal of Experimental Biology*, 213, 3019-3035.

Boudrias, MA (2002) Are pleopods just "more legs"? The functional morphology of swimming limbs in *Eurythenes gryllus* (Amphipoda). J Crustacean Biol 22: 581-594.

Boxshall, G. A., Yen, J., and Strickler, R. (1997)."Functional significance of the sexual dimorphism in the cephalic appendages of *Euchaeta rimana* Bradford," *Bulletin of Marine Science*, 61(2), 387-398.

Boxshall, G. A., and Huys, R. (1998)."The ontogeny and phylogeny of copepod antennules," *Phil. Trans. R. Soc. Lond. B*, 353, 765-786.

Brewer, M. C. (1998). "Mating behaviours of *Daphnia pulicaria*, a cyclic parthenogen: comparisons with copepods," *Phil. Trans. R. Soc. Lond. B.*, 353, 805-815.

Brewer, M. C., Dawidowicz, P., and Dodson, S. I. (1999). "Interactive effects of fish kairomone and light on *Daphnia* escape behavior," *Journal of Plankton Research*, 21(7), 1317-1335.

Bronmark, C. and Hansson, L. (2005).The Biology of Lakes and Ponds. New York, Oxford University Press.

Browman, H. I., Kruse, S., and O'Brien, W. J. (1989). "Foraging behavior of the predaceous cladoceran, *Leptodora kindti*, and escape responses of their prey," *Journal of Plankton Research*, 11(5), 1075-1088.

Brücker, Ch. 1997. 3D scanning PIV applied to an air flow in a motored engine using digital high-speed video. Meas. Sci. Technol. 8:1480-1492.

Bundy, M. H. and Paffenhöfer, G. -A. (1996). "Analysis of flow fields associated with freely swimming calanoid copepods," *Marine Ecology Progress Series*, 133, 99-113.

Burdick, D. S., Hartline, D. K., and Lenz, P. H. (2007)."Escape strategies in co-occurring calanoid copepods," *Limnology and Oceanography*, 52(6), 2373-2385.

Buskey, E. J., Lenz, P. H., and Hartline, D. K. (2002)."Escape behavior of planktonic copepods in response to hydrodynamic disturbances: high speed video analysis," *Marine Ecology Progress Series*, 235, 135-146.

Campbell, R. W. and Dower, J. F. 2003.Role of lipids in the maintenance of neutral buoyancy by zooplankton.Mar. Ecol. Prog. Ser. 263:93-99.

Campos, EO (2009) Quick forward escape swimming in the stomatopod crustacean *Odontodactylus havanensis*. The Berkeley McNair Research Journal 16: 1-14.

Catton, K. B., Webster, D. R., Brown, J., and Yen, J. (2007)."Quantitative analysis of tethered and free-swimming copepodid flow fields," *Journal of Experimental Biology*, 210, 299-310.

Catton, K.B. 2009. Aspects of sensory cues and propulsion in marine zooplankton hydrodynamic distrubances. Ph.D. Thesis, Georgia Institute of Technology.

Catton KB, Webster DR, Kawaguchi S, Yen J (2011) The hydrodynamic wake of two species of krill: Implications for signaling among schooling krill. J Exp Biol 214: 1845-1856.

Catton, K. B., D. R. Webster, and J. Yen. 2012. The effect of fluid viscosity, habitat temperature, and body size on the flow disturbance of *Euchaeta*. Submitted.

Chang, K and Hanazoto, T. (2003)."Vulnerability of cladoceran species to predation by the copepod *Mesocyclops leuckarti*: laboratory observations on the behavioural interactions between predator and prey," *Freshwater Biology*, 48, 476-484.

Cheer AYL, Koehl MAR (1987) Paddles and rakes: Fluid flow through bristled appendages of small organisms. J Theor Biol 129: 17-39.

Cheng, Y., M. M. Torregrosa, A. Villegas, and F. J. Diez. 2011. Time resolved scanning PIV measurements at fine scales in a turbulent jet. Int. J. Heat Fluid Fl. 32:708-718.

Childress, S., M. A. R. Koehl, and M. Miksis. 1987. Scanning currents in Stokes flow and the efficient feeding of small organisms. J. Fluid Mech. 177, 407-436.

Cohen, R. E., and R. G. Lough. 1981. Length-weight relationships for several copepods dominant in the Georges Bank-Gulf of Maine area. J. Northw. Atl. Fish. Sci. 2:47-52.

Cowles DL (1994) Swimming dynamics of the mesopelagic vertically migrating penaeid shrimp *Sergestes similis*: Modes and speeds of swimming. J Crustacean Biol 14: 247-257.

Cuddington, K. M. and McCauley, E. (1994)."Food-dependent aggregation and mobility of the water fleas *Ceriodaphnia dubia* and *Daphnia pulex*," *Can. J. Zool.*, 72, 1217-1226.

Dabiri, J. O., Colin, S. P., and Costello, J. H. 2006. Fast-swimming hydromedusae exploit velar kinematics to form an optimal vortex wake. J. Exp. Biol. 209, 2025-2033.

Davidowicz, P. and Loose, C. J. (1992). "Cost of swimming by *Daphnia magna* during diel vertical migration," *Limnol.Oceanogr.*, 37(3), 665-669.

Davis, WJ (1968) Quantitative analysis of swimmeret beating in the lobster. J Exp Biol 48: 643-662.

DeVoria, A. C. and Ringuette, M. J. 2012.Vortex formation and saturation for low-aspepct-ratio rotating flat-plate fins. Exp. Fluids 52, 441-462.

Doall, M. H., Colin, S. P., Strickler, R., and Yen, J. (1998)."Locating a mate in 3D: the case of Temora longicornis," *Phil. Tran. R. Soc. Lond. B*, 353, 681-689.

Doall, M. H., Strickler, J. R., Fields, D. M., and Yen, J. (2002). "Mapping the free-swimming attack volume of a planktonic copepod, *Euchaeta rimana*," *Marine Biology*, 140, 871-879.

Dodson, S. L. and Ramcharan, C. (1991)."Size-specific swimming behavior of *Daphnia pulex*," *Journal of Plankton Research*, 13(6), 1367-1379.

Dodson, S. I., Hanazoto, T., and Gorski, P. R. (1995). "Behavioral responses of *Daphnia pulex* exposed to carbaryl and *Chaoborus* kairomone," *Env. Toxic.Chem.*, 14(1).43-50.

Dodson, S. I., Ryan, S., Tollrian, R., and Lampert, W. (1997a). "Individual swimming behavior of *Daphnia*: effects of food, light, and container size in four clones," *Journal of Plankton Research*, 19(10), 1537-1552.

Dodson, S. I., Tollrian, R., and Lampert, W. (1997b)."*Daphnia* swimming behavior during vertical migration," *Journal of Plankton Research*, 19(8), 969-978.

Dodson, S. L., Caceres, C. E., and Rogers, D. C. (2010)."Cladocera and other branchiopoda," pp. 773-827. In Thorp, J. H. and Covich, A. P. (eds.), Ecology and classification of north american freshwater invertebrates. Elsevier.

Drescher, K., R. E. Goldstein, N. Michel, M. Polin, and I. Tuval. 2010. Direct measurements of the flow field around swimming microorganisms. Phys. Rev. Lett. 105, 168101.

Ellington, C. E. 1978. The aerodynamics of normal hovering flight: three approaches. pp 327-346. *In* K. Schmidt-Nielsen, L. Bolis, and S. H. P. Maddrell. [eds.], Comparative Phsyiology: Water, Ions, and Fluid Mechanics. Cambridge University Press.

Ellington CP (1984) The aerodynamics of hovering insect flight. III. Kinematics. Phil Trans R Soc Lond B 305: 41-78.

Elsinga, G. E., F. Scarano, B. Wieneke, and B. W. van Oudheusden. 2006. Tomographic particle image velocimetry. Exp. Fluids 41:933-947.

Elsinga, G. E., B. Wieneke, F. Scarano, and A. Schröder. 2008. Tomographic 3D-PIV and applications. p. 103-125. *In* A. Schroeder and C. E. Willert [eds.], Particle image velocimetry: Topics appl. physics, Vol. 112. Springer-Verlag, Berlin.

Elsinga, G. E., J. Westerweel, F. Scarano, and M. Novara. 2011. On the velocity of ghost particles and the bias errors in tomographic-PIV. Exp. Fluids 50:825-838.

Endo, Y. 1983. Orientation of Antarctic krill in an aquarium. Nippon Suisan Gakkaishi 59(3), 465-468.

Esposito, C. J., Tangorra, J. L., Flammang, B. E., and Lauder, G. V. 2012. A robotic fish caudal fin: effects of stiffness and motor program on locomotor performance. J. Exp. Biol. 215, 55-67.

Fields, D. and Yen, J. (1992)."Fluid mechanosensory stimulation of behavior from a planktonic marine copepod, *Euchaeta rimana* Bradford," *Journal of Plankton Research*, 24(8), 747-755.

Fields, D. and Yen, J. (1993). "Outer limits and inner structure: the 3-dimensional flow field of *Pleuromamma xiphias* (Calanoida: Metridinidae)," *Bulletin of Marine Science*, 53(1), 84-95.

Fields, D. M. and Yen, J. (1996)."The escape response of *Pleuromamma xiphias* in response to a quantifiable fluid mechanical disturbance," pp. 323-339. In Lenz, P. H., Hartline, D. K., Purcell, P. E., and MacMillan, D. L. (eds.), Zooplankton: sensory ecology and physiology, Vol. 1. Gordon and Breach.

Fields, D. M. and Yen, J. (1997)."The escape behavior of marine copepods in response to a quantifiable fluid mechanical disturbance," *Journal of Plankton Research*, 19(9), 1289-1304.

Fields, D. M., and J. Yen. 1997. Implications of the feeding current structure of *Euchaeta rimana*, a carnivorous pelagic copepod, on the spatial orientation of their prey. J. Plankt. Res. 19:79-95.

Fields, D. M., Shaeffer, D. S., and Weissburg, M. J. (2002)."Mechanical and neural responses from the mechanosensory hairs on the antennule of *Gaussia princeps*," *Marine Ecology Progress Series*, 227, 173-186.

Fox, H. M. and Mitchell, Y. (1952). "Relation of the rate of antennal movement in *Daphnia* to the number of eggs carried in the brood pouch," *J. Exp. Biol.,* 30, 238-242.

Gassie, D. V., Lenz, P. H., Yen, J., and Hartline, D. K. (1993). "Mechanoreception in zooplankton first antennae: electrophysiological techniques," *Bulletin of Marine Science*, 53(1), 96-105.

Gelinas, M., Pinel-Alloul, B., and Slusarczyk, M. (2007)."Formation of morphological defences in responses to YOY perch and invertebrate predation in two *Daphnia* species coexisting in a mesotrophic lake," *Hydrobiologia*, 594, 175-185.

Gerritsen, J., Porter, K. G., and Strickler, J. R. (1988). "Not by sieving alone: observations of suspension feeding in *Daphnia*," *Bulletin of Marine Science*, 43(3), 366-376.

Goldthwait S, Yen J, Brown J, Alldredge A (2004) Quantification of marine snow fragmentation by swimming euphausiids. Limnol. Oceanogr. 49(4): 940-952.

Gorski, P. R. and Dodson, S. I. (1996). "Free-swimming *Daphnia pulex* can avoid following Stokes' law," *Limnol. Oceanogr*., 41(8), 1815-1821.

Gries, R., Johnk, K., Fields, D., and Strickler, J. R. (1999). "Size and structure of 'footprints' produced by *Daphnia*: impact of animal size and density gradients," *Journal of Plankton Research*, 21(3), 509-523.

Hamner, W. H., P. P. Hamner, S. W. Strand, and R. W. Gilmer. 1983. Behavior of Antarctic krill, *Euphausia superba*: chemoreception, feeding, schooling, and molting. Science 22, 433-435.

Hamner, W. H. 1984. Aspects of schooling in *Euphausia superba*. J. Crust. Biol. 4(1), 67-74.

Hartline, D. K., Lenz, P. H., and Yen, J. (1996)."Physiological and behavioral studies of escape responses in calanoid copepods." pp 341-354. In Lenz, P. H., Hartline, D. K., Purcell, P. E., and MacMillan, D. L. (eds.), Zooplankton: sensory ecology and physiology, Vol. 1. Gordon and Breach.

Haury, L. R. (1980). "Experimental evaluation of the avoidance reaction of *Calanus finmarchicus*," *Journal of Plankton Research*, 2(3), 187-202.

Hebert, P. D. N. (1978). "The adaptive significance of cyclomorphosis in *Daphnia*: more possibilities," *Freshwater Biology*, 8, 313-320.

Hedrick, T.L. (2008). "Software techniques for two- and three-dimensional kinematic measurements of biological and biomimetic system," *Bioinspiration & Biomimetics*, 3(3), 034001 (6pp).

Hessler RR (1985) Swimming in crustacea. Trans R Soc Edinburgh 76: 115-122.

Hinsch, K. D. 2002. Holographic particle image velocimetry. Meas. Sci. Technol. 13:R61-R72.

Hoyer, K., M. Holzner, B. Luthi, M. Guala, A. Liberzon, and W. Kinzelbach. 2005. 3D scanning particle tracking velocimetry. Exp. Fluids 39:923-934.

Humes, A. G. (1994). "How many copepods?"*Hydrobiologia,* 292/293, 1-7.

Hwang, J. and Strickler, R. (1994). "Effects of periodic turbulent events upon escape responses of a calanoid copepod, *Centropages hamatus*," *Bulletin of Plankton Society of Japan*, 41(2), 117-130.

Ikeda, T., Y. Kanno, K. Ozaki, and A. Shinada. 2001. Metabolic rates of epipelagic marine copepods as a function of body mass and temperature. Mar. Biol. 139:587-596.

Ivanenko VN, Defaye D, Cuoc C (2007) A new calanoid copepod (Spinocalanidae) swarming at a cold seep site on the Gabon continental margin (Southeast Atlantic). Cah Biol Mar 48: 37-54.

Jacobs, J. (1964). "Hat der hohe sommerhelm zyklomorpher Daphnien einen anpassungswert?"*Verh.Internat.Verein.Limnol.* 15, 676-683.

Jacobs, J. (1967). "Untersuchungen zur funktion und evolution der zyklomorphose bei *Daphnia*, mit besonderer berucksichtigung der selektion durch fische."*Arch. Hydrobiol.* 62(4), 467-541.

Jiang, H., Osborn, T. R., and Meneveau, C. (2002a). "The flow field around a freely swimming copepod in steady motion. Part I: Theoretical analysis," *Journal of Plankton Research*, 24(3), 167-189.

Jiang, H., Meneveau, C, and Osborn, T. R. (2002b)."The flow field around a freely swimming copepod in steady motion. Part II: Numerical simulation," *Journal of Plankton Research*, 24(3), 191-213.

Jiang, H. and Paffenhöfer, G. -A. (2008). "Hydrodynamic signal perception by the copepod *Oithona plumifera*," *Marine Ecology Progress Series*, 373, 37-52.

Jiang, H. and Kiørboe, T. (2011a)."Propulsion efficiency and imposed flow fields of a copepod jump," *Journal of Experimental Biology*, 214, 476-486.

Jiang, H. and Kiørboe, T. (2011b)."The fluid dynamics of swimming by jumping in copepods," *Journal of the Royal Society Interface*, rsif.2010.0481.

Johnson ML, Tarling GA (2008) Influence of individual state on swimming capacity and behaviour of Antarctic krill *Euphausia superba*. Mar Ecol Prog Ser 366: 99-110.

Johnson, W. 1994. Helicopter Theory. Mineola, NY: Courier Dover Publications.

Jonsson, P. R. and Tiselius, P. (1990)."Feeding behaviour, prey detection and capture efficiency of the copepod Acartia tonsa feeding on planktonic ciliates," *Marine Ecology Progress Series*, 60, 35-44.

Kajitani, L., and D. Dabiri. 2005. A full three-dimensional characterization of defocusing digital particle velocimetry. Meas. Sci. Technol. 16:790-804.

Kanda K, Takagi K, Seki Y (1982) Movement of the larger swarms of Antarctic krill *Euphausia superba* population off Enderby Land during 1976-1977 season. J of Tokyo U of Fisheries 68: 25-42.

Katz, J., and J. Sheng. 2010. Applications of holography in fluid mechanics and particle dynamics. Ann. Rev. Fluid Mech. 42:531-555.

Kawaguchi S, King R, Meijers R, Osborn JE, Swadling KM, Ritz DA, Nicol S (2010) An experimental aquarium for observing the schooling behaviour of Antarctic krill (*Euphausia superba*). Deep-Sea Research II 57: 683-692.

Kerfoot, W. C. (1978). "Combat between predatory copepods and their prey: Cyclops, Epischura, and Bosmina." *Limnol.Oceanogr.*, 23(6), 1089-1102.

Kerfoot, W. C., Kellogg, D. L., and Strickler, J. R. (1980). "Visual observations of live zooplankters: evasion, escape, and chemical defenses." In Kerfoot, W. C. (ed.) Evolution and Ecology of Zooplankton Communities.University Press of New England.

Kils U (1981) Swimming behaviour, swimming performance, and energy balance of Antarctic krill, *Euphausia superba*. BIOMASS Sci Ser 3: 1-122.

Kim, D. and Gharib, M. 2011. Characteristics of vortex formation and thrust performance in drag-based paddling propulsion.J.Exp. Biol. 214, 2283-2291.

Kiørboe, T., Saiz, E., and Viitasalo, M. (1996). "Prey switching behaviour in the planktonic copepod *Acartia tonsa*," *Marine Ecology Progress Series*, 143, 65-75.

Kiørboe, T. and Visser, A. (1999)."Predator and prey perception in copepods due to hydromechanical signals," *Marine Ecology Progress Series*, 179, 81-95.

Kiørboe, T., Saiz, E., and Visser, A. (1999)."Hydrodynamic signal perception in the copepod *Acartia tonsa*," *Marine Ecology Progress Series*, 179, 97-111.

Kiørboe, T., Andersen, A., Langlois, V., Jakobsen, H. H., and Bohr, T. (2009), "Mechanisms and feasibility of prey capture in ambush-feeding zooplankton," *PNAS*, 106(30), 12394-12399.

Kiørboe, T. (2010). "How zooplankton feed: mechanisms, traits and trade-offs," Biological Reviews, doi:10,1111/j.1469-185X.2010.00148.x.

Kiørboe, T., Jiang, H., and Colin, S. P. (2010a). "Danger of zooplankton feeding: the fluid signal generated by ambush-feeding copepods," *Proceedings of the Royal Society B*, 277, 3229-3237.

Kiørboe, T., Andersen, A., Langlois, V., and Jakobsen, H. H. (2010b). "Unsteady motion: escape jumps in planktonic copepods, their kinematics and energetics," *Journal of the Royal Society Interface*, 7, 1591-1602.

Knox, G. A. 1994. The Biology of the Southern Ocean. Cambridge University Press.

Kirk, K. L. (1985). "Water flows produced by *Daphnia* and *Diaptomus*: implications for prey selection by mechanosensory predators." *Limnol.Oceanogr*. 30(3), 679-686.

Knight-Jones EW, Macfadyen A (1959) The metachronism of limb and body movements in annelids and arthropods. Proc XVth Int Cong Zool pp. 969-971.

Kohlhage K, Yager J (1994) An analysis of swimming in remipede crustaceans. Phil Trans R Soc Lond B 346: 213-221.

Koehl, M. A. R. and Strickler, R. (1981)."Copepod feeding currents: food capture at low Reynolds number," *Limnol.Oceanogr.*, 26(6), 1062-1073.

Kohlhage, K. (1994). "The economy of paddle-swimming: the role of added water and viscosity in the locomotion of *Daphnia magna*," *Zool. Beitr. N. F.* 35(1), 47-54.

LaForsch, C. and Tollrian, R. (2004a). "Inducible defenses in multipredator environments: cyclomorphosis in *Daphnia cucullata*," *Ecology*, 85(8), 2302-2311.

LaForsch, C. and Tollrian, R. (2004b). "Extreme helmet formation in *Daphnia cucullata* induced by small-scale turbulence," *Journal of Plankton Research*, 26(1), 81-87.

Landry, M. R. (1980). "Detection of prey by *Calanus pacificus*: implications of the first antennae," *Limnol.Oceanogr.*, 25(3), 545-549.

Lauder, G. V. and Madden, P. G. A. 2007. Fish locomotion: kinematics and hydrodynamics of flexible foil-like fins. Exp. Fluids 43:641-653.

Laverack MS, Neil DM, Robertson RM (1977) Metachronal exopodite beating in the mysid *Praunus flexuosus*: A quantitative analysis. Proc R Soc Lond B 198: 139-154.

Lenz, P. H. and Yen, J. (1993). "Distal setal mechanoreceptors of the first antennae of marine copepods," *Bulletin of Marine Science*, 53(1), 170-179.

Lenz, P. H., Weatherby, T. M., Weber, W., and Wong, K. K. (1996)."Sensory specialization along the first antenna of a calanoid copepod, *Pleuromamma xiphias* (Crustacea)," pp 355-363. In Lenz, P. H., Hartline, D. K., Purcell, P. E., and MacMillan, D. L. (eds.), Zooplankton: sensory ecology and physiology, Vol. 1. Gordon and Breach.

Lenz, P. H., Hower, A. E., and Hartline, D. K. (2004)."Force production during pereiopod power strokes in *Calanus finmarchicus*," *Journal of Marine Systems*, 49, 133-144.

Li, J. L. and Li, H. (1979)."Species-specific factors affecting predator-prey interactions of the copepod *Acanthocyclops vernalis* with its natural prey," *Limnol.Oceanogr*. 24(4), 613-626.

Liberzon, A., R. Gurka, and G. Hetsroni. 2004. XPIV-multi-plane stereoscopic particle image velocimetry. Exp. Fluids 36:355-362.

Lim JL, DeMont ME (2009) Kinematics, hydrodynamics and force production of pleopods suggest jet-assisted walking in the American lobster (*Homarus americanus*). J Exp Biol 212: 2731-2745.

Macmillan DL, Neil DM, Laverack MS (1976) A quantitative analysis of exopodite beating in the larvae of the lobster *Homarus gammarus* (L.). Phil Trans R Soc Lond B 274: 69-85.

Malkiel, E., Sheng, J., Katz, J., and Strickler, J. R. (2003). "The three-dimensional flow field generated by a feeding calanoid copepod measured using digital holography," *Journal of Experimental Biology*, 206(20), 3657-3666.

Mauchline, J. (1998). The Biology of Calanoid Copepods. San Diego, Ca. Academic Press.

Mazzocchi, M. G. and Paffenhöfer, G. -A. (1999). "Swimming and feeding behavior of the planktonic copepod *Clausocalanus furcatus*," *Journal of Plankton Research*, 21, 1501-1518.

Meng, H., G. Pan, Y. Pu, and S. H. Woodward. 2004. Holographic particle image velocimetry: From film to digital recording. Meas. Sci. Technol. 15:673-685.

Miller, C. B. (2004). Biological Oceanography. Malden, MA, Blackwell Publishing Company.

Miyashita K, Aoki I, Inagaki T (1996) Swimming behaviour and target strength of isada krill (*Euphausia pacifica*). ICES J Mar Sci 53: 303-308.

Morgan, E (1972) The swimming of *Nymphon gracile* (Pycnogonida): The swimming gait. J Exp Biol 56: 421-432.

Murphy, D. W., D. R. Webster, S. Kawaguchi, R. King, and J. Yen. 2011. Metachronal swimming in Antarctic krill: Gait kinematics and system design. Mar. Biol. 158:2541-2554.

Nicol, S, Endo Y (1997) Krill Fisheries of the World. FAO Fisheries Technical Paper. No. 367. Rome: FAO. pp. 1-100.

Novara, M., K. J. Batenburg, and F. Scarano. 2010. Motion tracking-enhanced MART for tomographic PIV. Meas. Sci. Technol. 21:035401.

O'Brien, W. J. and Vinyard, G. L. (1978)."Polymorphism and predation: The effect of invertebrate predation on the distribution of two varieties of *Daphnia carinata* in South India ponds," *Limnol.Oceanogr*. 23(3), 452-460.

O'Keefe, T. C., Brewer, M. C., and Dodson, S. I. (1998)."Swimming behavior of *Daphnia*: its role in determining predation risk," *Journal of Plankton Research*, 20(5), 973-984.

Orlov, S. S., S. I. Abarzhi, S. B. Oh, G. Barbastathis, and K. R. Sreenivasan. 2010. High-performance holographic technologies for fluid-dynamics experiments. Philosophical Transactions of the Royal Society A 368:1705-1737.

Patria MP, Wiese K (2004) Swimming in formation in krill (Euphausiacea), a hypothesis: dynamics of the flow field, properties of antennular sensor systems and a sensory-motor link. J Plankton Res 26: 1315-1325.

Pelster, B. 1998.Buoyancy. P. 25-42. *In* Evans, D. H. [ed.], The physiology of fishes. CRC Press, New York.

Penalva-Arana, D. C., Moore, P. A., Feinburg, B. A., DeWall, J., and Strickler, J. R. (2007). "Studying *Daphnia* feeding behavior as a black box: a novel electrochemical approach," *Hydrobiologia*, 594, 153-163.

Pennak, R. W. (1978). Fresh-water invertebrates of the United States. New York, NY. John Wiley and Sons.

Pereira, F., M. Gharib, D. Dabiri, and D. Modarress. 2000. Defocusing digital particle image velocimetry: A 3-component 3-dimensional DPIV measurement technique: Application to bubbly flows. Exp. Fluids 29 Suppl:S78-S84.

Pijanowska, J. and Kowalczewski, A. (1997). "Predators can induce swarming behavior and locomotory responses in *Daphnia*," *Freshwater Biology*, 37, 649-656.

Pijanowska, J., Dawidowicz, P., and Weider, L. J. (2006). "Predator-induced escape response in *Daphnia*," *Arch. Hydrobiol*., 167(1-4), 77-87.

Porter, K. G., Gerritsen, J., and Orcutt, J. D. (1982)."The effect of food concentration on swimming patterns, feeding behavior, ingestion, assimilation, and respiration by *Daphnia*," Limnol.Oceanogr. 27(5), 935-949.

Pu, Y., and H. Meng. 2005. Four-dimensional dynamic flow measurement by holographic particle image velocimetry. Applied Optics 44:7697-7708.

Riessen, H. (1982). "Predatory behavior and prey selectivity of the pelagic water mite *Piona constricta*." *Can. J. Fish.Aquat. Sci.*, 39, 1569-1579.

Riessen, H. P., O'Brien, W. J., and Loveless, B. (1984)."An analysis of the components of *Chaoborus* predation on zooplankton and the calculation of relative prey vulnerabilities."*Ecology*, 65(2), 514-522.

Rohr, J. J. and F. E. Fish. 2004. Strouhal numbers and optimization of swimming by odontocete cetaceans. J. Exp. Biol. 207, 1633-1642.

Saiz, E. and Alcaraz, M. (1992). "Free-swimming behaviour of *Acartia clausi* (Copepoda: Calanoida) under turbulent water movement," *Marine Ecology Progress Series*, 80, 229-236.

Scarano, F. and Poelma, C. 2009. “Three-dimensional vorticity patterns of cylinder wakes,” *Exp. Fluids*, 47:69-83.

Scavia, D., Fahnenstiel, G. L., Davis, J. A., and Kreis, R. G. (1984). "Small-scale nutrient patchiness: Some consequences and a new encounter mechanism." *Limnol.Oceanogr.*, 29(4), 785-793.

Schabes M, Hamner W (1992) Mysid locomotion and feeding: Kinematics and water-flow patterns of Antarctomysis sp., *Acanthomysis sculpta*, and *Neomysis rayii*. J Crustacean Biol 12: 1-10.

Scourfield, D. J. (1900)."The swimming peculiarities of Daphnia and its allies, with an account of a new method of examining living Entomostraca and similar organisms."*Journ. Quekett Microscopical Club, Ser. 2*, 7(47), 395-404.

Sensenig AT, Kiger KT, Shultz JW (2009) The rowing-to-flapping transition: ontogenetic changes in gill-plate kinematics in the nymphal mayfly *Centroptilum triangulifer* (Ephemeroptera, Baetidae). Biol J Linn Soc 98: 540-555.

Seuront, L., Yamazaki, H. and Souissi, S. (2004). "Hydrodynamic disturbance and zooplankton swimming behavior," *Zoological Studies*, 43(2), 376-387.

Seuront, L., Schmitt, F. G., Brewer, M. C., Strickler, J. R., and Souissi, S. (2004). "From random walk to multifractal random walk in zooplankton swimming behavior."*Zoological Studies*, 43(2), 498-510.

Singarajah, K. V. (1975). "Escape reactions of zooplankton: effects of light and turbulence," *J. Mar. Biol. Ass. U.K.*, 55, 627-639.

Sleigh MA, Barlow DI (1980) Metachronism and control of locomotion in animals with many propulsive structures. In: Elder HY, Trueman ER (ed) Aspects of Animal Movement, Cambridge University Press, Cambridge, pp 49-70.

Stamhuis EJ, Videler JJ (1998a) Burrow ventilation in the tube-dwelling shrimp (*Callianassa subterranea* (Decapoda: Thalassinidea). I. Morphology and motion of the pleopods, uropods and telson. J Exp Biol 201: 2151-2158.

Stamhuis EJ, Videler JJ (1998b) Burrow ventilation in the tube-dwelling shrimp (*Callianassa subterranea* (Decapoda: Thalassinidea). II. The flow in the vicinity of the shrimp and the energetic advantages of a laminar non-pulsating ventilation current. J Exp Biol 201: 2159-2170.

Stamhuis, E. J., J. J. Videler, L. A. van Duren, and U. K. Muller. 2002. Applying digital particle image velocimetry to animal-generated flows: Traps, hurdles and cures in mapping steady and unsteady flows in Re regimes between 10^{-2} and 10^{5}, Exp. Fluids 33:801-813.

Stretch JJ, Hamner PP, Hamner WH, Michel WC, Cook J, Sullivan CW (1988) Foraging behavior of Antarctic krill *Euphausia superba* on sea ice microalgae. Mar Ecol Prog Ser 44: 131-139.

Strickler, R. and Bal, A. (1973). "Setae of the first antennae of the copepod Cyclops scutifer (Sars): their structure and importance." *Proc. Nat. Acad. Sci. USA*, 70(9), 2656-2659.

Strickler, R. (1975)."Swimming of planktonic *Cyclops* species (Copepoda, Crustacea): pattern, movements and their control." In Wu, T., Brokaw, C., and Brennen, C. (eds.) Swimming and Flying in Nature, Volume 2. New York, Plenum Press.

Strickler, R. (1977)."Observation of swimming performances of planktonic copepods," *Limnology and Oceanography*, 22(1), 165-170.

Strickler, R. (1982)."Calanoid copepods, feeding currents, and the role of gravity," *Science*, 218, 158-160.

Suchman, C. L. (2000). "Escape behavior of Acartia hudsonica copepods during interactions with scyphomedusae." *Journal of Plankton Research*, 22(12), 2307-2323.

Sutherland, K. R. and L. P. Madin. 2010. Comparative jet wake structure and swimming performance of salps. J. Exp. Biol. 213, 2967-2975.

Svensen, C. and Kiørboe, T. (2000)."Remote prey detection in *Oithona similis*: hydromechanical versus chemical cues," *Journal of Plankton Research*, 22(6), 1155-1166.

Swadling KM, Ritz DA, Nicol S, Osborn JE (2005) Respiration rate and cost of swimming for Antaractic krill, *Euphausia superba*, in large groups in the laboratory. Mar Biol 146: 1169-1175.

Szlauer, L. (1964). "Reaction of *Daphnia pulex* de Geer to the approach of different objects."*Polskie Archiwum Hydrobiologii*, 12(25), 5-16.

Tarling, GA, Johnson, ML (2006) Satiation gives krill that sinking feeling. Curr Biol 16, 3: 83-84.

Taylor, G. K., R. L. Nudds, and A. L. R. Thomas. 2003.Flying and swimming animals cruise at a Strouhal number tuned for high power efficiency. Nature 425, 707-711.

Tiselius, P. and Jonsson, P. R. (1990)."Foraging behaviour of six calanoid copepods: observations and hydrodynamic analysis," *Marine Ecology Progress Series*, 66, 23-33.

Todd, C. D., Laverack, M. S., and Boxshall, G. A. (1996).Coastal Marine Zooplankton, Cambridge, UK.Cambridge University Press.

Triantafyllou, G. S., M. S. Triantafyllou, and M. A. Grosenbaugh. 1993. Optimal thrust development in oscillating foils with application to fish propulsion. Journal of Fluids and Structures 7, 205-224.

Viitasalo, M., and Rautio, M. (1998). "Zooplanktivory by *Praunus flexuosus* (Crustacea:Mysidacea): functional responses and prey selection in relation to prey escape responses," *Marine Ecology Progress Series*, 174, 77-87.

Viitasalo, M., Flinkman, J., and Viherluoto, M. (2001). "Zooplanktivory in the Baltic Sea: a comparison of prey selectivity by *Clupea harengus* and *Mysis mixta*, with reference to prey escape reactions." *Marine Ecology Progress Series*, 216, 191-200.

van Duren, L. A. and Videler, J. J. (2003). "Escape from viscosity: the kinematics and hydrodynamics of copepod foraging and escape swimming," *Journal of Experimental Biology*, 206, 269-279.

Vannier J, Boissy P, Racheboeuf PR (1997) Locomotion in *Nebalia bipes*: a possible model for Palaeozoic phyllocarid crustaceans. Lethaia 30: 89-104.

Visser, A. W. (2001). "Hydromechanical signals in the plankton." *Marine Ecology Progress Series*, 222, 1-24.

Waggett, R. J. and Buskey, E. J. (2007a)."Calanoid copepod escape behavior in non-turbulent and turbulent hydrodynamic regimes," *Marine Ecology Progress Series*, 334, 193-198.

Waggett, R. J. and Buskey, E. J. (2007b)."Calanoid copepod escape behavior in response to a visual predator," *Marine Biology*, 150, 599-607.

Waggett, R. J. and Buskey, E. J. (2008)."Escape reaction performance of myelinated and non-myelinated calanoid copepods," *Journal of Experimental Marine Biology and Ecology*, 361, 111-118.

Walker JA (2002) Functional morphology and virtual models: Physical constraints on the design of oscillating wings, fins, and feet at intermediate Reynolds numbers. Integ and Comp Biol 42: 232-242.

Walker, J. A. and Westneat, M. W. 2000.Mechanical performance of aquatic rowing and flying. Proc. R. Soc. Lond. B. 267, 1875-1881.

Weber, A. and van Noordwijk, A. (2002). "Swimming behaviour of *Daphnia* clones: differentiation through predator infochemicals," *Journal of Plankton Research*, 24(12) 1335-1348.

Webster, D. R., and E. K. Longmire. 1998. Vortex rings from cylinders with inclined exits. Phys. Fluids 10:400-416.

Westerweel, J., and F. Scarano. 2005. Universal outlier detection for PIV data. Exp. Fluids 39: 1096-1100.

Wieneke, B. (2008). "Volume self-calibration for 3D particle image velocimetry," *Experiments in Fluids*, 45, 549-556.

Wiese, K. and H. P Marschall. 1990. Sensitivity to vibration and turbulence of water in context with schooling in Antarctic krill *Euphausia superba*. In eds. Wiese, K., Krenz, W. D., Tautz, J., Reichert, H., and Mulloney, B. Frontiers in Crustacean Neurobiology. Birkhauser Verlag Basel.

Wiese, K. and Ebina, Y. 1995. The propulsion jet of Euphausai superba (Antarctic krill) as a potential communication signal among conspecifics. J. Mar. Bio. Ass. U.K. 75, 43-54.

Wiese, K. 1996. Sensory capacities of euphausiids in the context of schooling. Mar. Fresh. Behav. Physiol. 28, 183-194.

Willert, C. E., and M. Gharib. 1992. Three-dimensional particle imaging with a single camera. Exp. Fluids 12:353-358.

Wootton RJ (1999) Invertebrate paraxial locomotory appendages: Design, deformation and control. J Exp Biol 202: 3333-3345.

Yen, J. (2000), "Life in transition: balancing inertial and viscous forces by planktonic copepods," *Biol. Bull.*, 198, 213-224.

Yen, J. and Nicoll, N. T. (1990)."Setal array on the first antennae of a carnivorous marine copepod, Euchaeta rimana."*Journal of Crustacean Biology*, 10(2), 218-224.

Yen, J., B. Sanderson, J. R. Strickler, and A. Okubo. 1991. Feeding currents and energy dissipation by *Euchaeta rimana*, a subtropical pelagic copepod. Limnol. Oceanogr. 36:362-369.

Yen, J., Lenz, P. H., Gassie, D. G., and Hartline, D. K. (1992)."Mechanoreception in marine copeopds: electrophysiological studies on the first antennae," *Journal of Plankton Research*, 14(4), 495-512.

Yen, J. and Strickler, R. (1996). "Advertisement and concealment in the plankton: what makes a copepod hydrodynamically conspicuous?" *Invertebrate Biology*, 115(3), 191-205.

Yen J, Brown J, Webster DR (2003) Analysis of the flow field of the krill, *Euphausia pacifica*. Mar Fresh Behav Physiol 36: 307-319.

Zaret, W. C. and Kerfoot, R. E. (1980)."The shape and swimming technique of *Bosmina longirostris*," *Limnol.Oceanogr.*, 25(1), 126-133.

Ziarek, J. J., Nihongi, A., Nagai, T., Uttieri, M., and Strickler, J. R. (2011). "Seasonal adaptations of *Daphnia* pulicaria swimming behaviour: the effect of water temperature." *Hydrobiologia*, 661, 317-317.